CRYSTALLIZATION OF TRISTEARIN FROM ITS SOLUTION IN DODECANE

by

Tianguang Jia

Submitted in partial fulfilment of the requirements
for the degree of Master of Science

at

Dalhousie University
Halifax, Nova Scotia
December 2017

© Copyright by Tianguang Jia, 2017

TABLE OF CONTENTS

LIST OF TABLES

LIST OF FIGURES

ix

ABSTRACT

A suspension of tristearin (SSS) crystals crystallized from 10% solution in dodecane (non-polar solvent), was studied using DSC (differential scanning calorimetry), Rheology, PLM (polarized light microscopy), and XRD (x-ray diffraction). Temperatures of -5, 0, 5, 12, 20, 28, and 35 °C, and shear rates of 0.9, 9, 90, and 900 s^{-1} were explored. DSC cooling rates of 1, 5, 10, and 15 C°/min showed two crystallization events (polymorphic changes). Onset temperatures (51.7 °C) suggests that the SSS molecules cluster in the liquid, and crystallize in the α form (54.1 °C). The viscosity from rheology (10^{-3} to 10^{-1} Pa·s) was shear thinning, with "*n*" of 0.4 to 0.6. The PLM flow micrographs showed segregation of the suspended crystals. The XRD showed that suspended *β* crystals increased their d-spacing 6 pm for 0.364 nm, and 2.5 pm for 0.383 nm (-5 °C to 35 °C). This is consistent with undiluted TAGs.

LIST OF ABBREVIATIONS AND SYMBOLS USED

CCD	Charge-Coupled Device
DODE	Differential scanning calorimetry
FOT	Fiber Optic Temperature Sensor
FWHM	Full Width at Half Maximum
GUI	Graphical user interface
LD	Lamellar Distance
PLM	Polarized Light Microscopy
SSS	Tristearin
T	Temperature of crystallization (K)
TAG	Triacylglycerols
TEC	Thermoelectric Cooler
u	Tangential velocity
WAXD	Wide Angle X-ray Diffraction
XRD	X-ray Diffraction
$\dot{\gamma}$	Shear rate
δ	Gap distance
η	Viscosity
η^*	Complex viscosity
q	Reciprocal lattice spacing (Å-1)
θ	Incident angle of x-rays
ΔG	Change in Gibbs energy (J)
λ	Wavelength of x-rays (Å)
d	The lamellar spacing of crystal planes
$\dot{\gamma}$	Shear rate, s^{-1}
ν	Fluid velocity, m/s
σ	Shear stress
τ	Torque at the shaft angular velocity
A_s	Effective contact area of the fluid on the

	shaft
u_θ	Local velocity
κ	Characteristic geometric ratio
$u_{\theta s}$	Velocity at the shaft
$\dot{\gamma}_{av}$	Volume-weighted average shear rate
2L	Double fatty acid chain length structure
3L	Triple fatty acid chain length structure

ACKNOWLEDGEMENTS

I would like to gratefully acknowledge my supervisor Dr. Gianfranco Mazzanti for his great patience, insight, patience, and generosity throughout my master study. Always available and helpful, he guided and encouraged me to a different field. This work would not be possible done without this great help.

I would also like to thank my thesis advisory team Dr. Suzanne Budge and Dr. Andrew MacIntosh, for providing valuable feedback and insight into this work.

I would like to thank all my lab colleagues, Omar Qatami, Yijin Su for their helpful discussion and friendship during my research. They have made my master study become a memorable and enjoyable journey.

I would like to say a special thank you to my family, especially my mom and dad, for their emotional and financial support during my study. Without their unconditional love, I cannot complete this research. My appreciation also goes to my friends for their kindness and generous support.

1 INTRODUCTION

Fats and oils are a necessary part of our daily diet, which are commonly found in plants and animals. Fats and oils are important substances for maintaining the human health physically and nutritionally. For example, ω-3 fatty acids are essential to keep the normal function of membrane fluidity, cellular signaling, gene expression, and eicosanoid metabolism (McClements & Decker, 2008). Many sensorial properties and the appearance of foods are also determined by fats and oils, *e.g.,* tenderness, texture, mouthfeel, structural integrity, lubrication, incorporation of air, heat transfer, and extended shelf-life (Rodríguez-García, Laguna, Puig, Salvador, & Hernando, 2013). In the pharmaceutical industry, fats and oils are ingredients used as delivery agents for drugs, imaging agents, and biomolecules. Drugs can be encapsulated within the hydrophobic core of a solid–lipid nanoparticle and slowly released as the solid–lipid nanoparticle is broken down. The fat solid–lipid nanoparticle provides a biodegradable route for the sustained and targeted release of therapeutics (Hughes and Walsh 2015). They are also used extensively in the cosmetic industry, since ancient times.

Thus, there is an ongoing research effort in the world to obtain a better understanding of fats and oils, from the perspectives of physics, chemistry, and biochemistry, and under industrial processing conditions (Sato et al., 1999). These molecules solidify into crystals, and these crystals have different polymorphic forms. This peculiarity determines the actual fat properties, such as melting point, sensory properties, and mechanical strength in a given product or environment. Furthermore, the crystals form hierarchical meso-structures and macrostructures: the fat crystalline networks. The networks serve as 'sponges' that keep the liquid parts of these materials from oozing out. The characteristics of the material are therefore influenced at all levels by processing conditions such as crystallization temperature, cooling rate, and shear rate.

The largest volume fraction of a triacylglycerol mixture is occupied by the non-polar alkyl chains of the molecules. The aim of this research was to study the behavior of the material formed as the triacylglycerol molecules crystallize out of a non-polar solvent. The behaviour was studied observing the crystallization of tristearin from a diluted 10% solution in dodecane. Essentially, a suspension of crystals was formed out of the solution

as it was cooled down. Tristearin was chosen as solute due to its relatively stable chemical and physical properties. The extensively used and documented alkane, dodecane, was selected as solvent. The 10% w/w tristearin value was arbitrarily chosen to provide a "dilute solution". The tests included different crystallization temperatures (-5, 0, 5, 12, 20, 28, and 35 °C) and shear rates (0.9, 9, 90, and 900 s^{-1}). The behaviour was observed via differential scanning calorimetry (DSC), rheology, polarized light microscopy (PLM), and x-ray diffraction (XRD).

The DSC data provided reference temperatures for melting/dissolution and maximum practical crystallization temperature possible. The thermal behavior data from DSC was additionally analyzed, and the Avrami model was fitted to the data to test its usefulness in describing the kinetics of crystallization.

The effect of the applied shear on the mechanical characteristics of the suspensions obtained from crystallizing the 10% SSS/dodecane solution was studied using a AR2000 rheometer. Small deformation oscillatory tests were conducted during the initial static crystallization. Then shear flow was applied, using different constant shear rates. Another oscillatory test was applied after stopping the shear.

The shear effect on early crystallization events and on the morphology of tristearin crystal clusters was also observed using PLM. Image analysis of PLM micrographs obtained from the material crystallized in a shear cell provided mostly qualitative information about the suspensions.

The nanostructure of the SSS crystals, formed out of the solution, was studied using X-ray diffraction (XRD). The internal geometry of the nanocrystals, which is the signature of their polymorphism, is characterized primarily by the values of the d-spacings between crystalline planes. Deng (2014, Mazzanti's research team) studied the effect of temperature on the d-spacings of pure TAGs and some of their binary mixtures. For pure SSS, she compared six main crystal planes of the small d-spacings spectrum. They were grouped by their general location into larger d-spacings, medium d-spacings, and small d-spacings. The data were plotted by taking the d-spacings at -20 °C as a reference. She found that when temperature increased, the small d-spacings also increased. This behaviour turned out to be

common to several pure triacylglycerols and their mixtures. For SSS, the d-spacings that were most sensitive to temperature were those located at 0.363 and 0.384 nm (at -5 °C).

In this research, the XRD experiments were designed to examine the relationship between small d-spacings and temperature in SSS crystals formed from SSS diluted in a nonpolar solvent, dodecane. The results from these crystals in suspension were compared with Deng's research with undiluted triacylglycerol samples. The possibility of using this relationship as intrinsic thermometers under static and shear condition had been indicated by Deng.

The planning of experiments also resulted in the design and set-up of many equipment improvements.

This thesis summarizes in chapter 2 the background that was prepared to attempt a systematic understanding of the observations from the experiments. It then describes in detail the experimental methods mentioned above to study our material: DSC, rheology, PLM and XRD. The results, in chapter 4, are also organized following this order. An overall summary and conclusion is given in the final chapter.

1.1 Objectives

The general goal in this research is to obtain a better understanding of the characteristics of the material "tristearin crystals in suspension", obtained by cooling a solution of 10% tristearin in dodecane to different temperatures and under different shear rates.

The specific objectives of this thesis are:

- To investigate the thermal properties of a 10% SSS/dodecane solution and of the suspension formed as the SSS crystallizes, under different cooling rates.
- To investigate the effect of applied shear rates on the apparent viscosity and complex viscosity of suspensions of SSS crystals. The suspensions will be formed by crystallizing SSS out of a 10% SSS/dodecane solution at different temperatures.
- To observe the morphology and the early crystal growth of the suspension of SSS crystals obtained from 10% SSS/dodecane solution, under different temperatures and shear rates
- To study how the small d-spacings (computed from WAXD peaks) of the SSS crystals in suspension (obtained from a diluted 10% SSS/dodecane solution) change their position as temperature changes.

2 LITERATURE REVIEW

2.1 Structures

2.1.1 Nanostructures

2.1.1.1 Polymorphism in Crystalline Triacylglycerols (TAGs)

As a subgroup of lipids, fats and oils are common organic compounds. "Fat" and "oil" are interchangeable terms, that depend on the physical state of the material at room temperature. Fats are made of hard crystalline solids, arranged in a three-dimensional network that contains liquid oil (10%–90%) (Bailey, 1979). As shown in Figure 2.1, a structural hierarchy exists in a three-dimensional fat crystal network (Marangoni & Wesdorp, 2013).
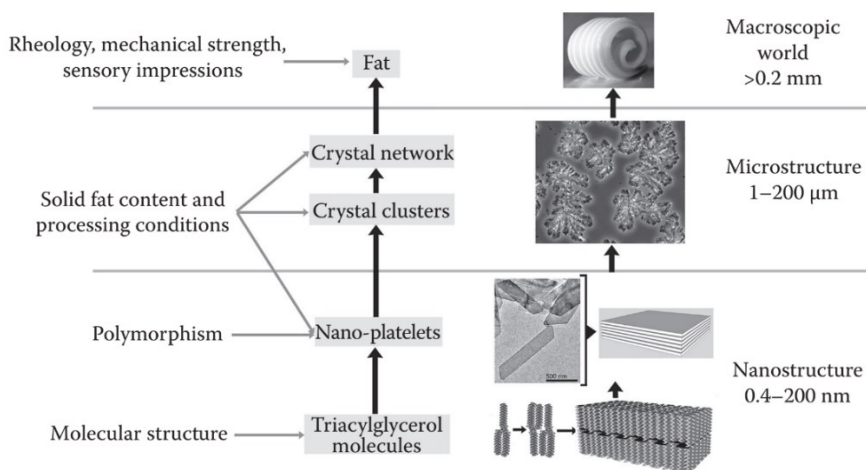
Figure 2.1 Structural hierarchy in a fat crystal network from molecules to the material from (Marangoni & Wesdorp, 2013).

The fundamental building blocks of fat crystal networks are triacylglycerol (TAG) molecules (Figure 2.2). A TAG is constituted by a glycerol backbone with three fatty acids esterified to the three alcohol groups at specific locations (*i.e.,* sn-1, sn-2, and sn-3) (Hartel, 2001a). The physical properties of fats depend on the molecular structure of TAGs, such as the length of the fatty acid chains, the existence and configuration of double bonds, and the stereospecific position of the fatty acid on the glycerol backbone (Marangoni & Wesdorp, 2013; Small, 1966).

$$
\begin{array}{c}
\text{O} \\
\parallel \\
\text{H}_2\text{C}-\text{O}-\text{C}-(\text{CH}_2)_n-\text{CH}_3 \\
\text{O} \qquad\qquad | \\
\parallel \qquad\qquad\; \\
\text{CH}_3-(\text{CH}_2)_n-\text{C}-\text{O}-\text{C}-\text{H} \\
| \\
\text{H}_2\text{C}-\text{O}-\text{C}-(\text{CH}_2)_n-\text{CH}_3 \\
\parallel \\
\text{O}
\end{array}
$$
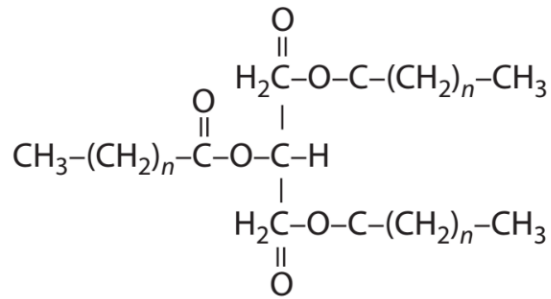
Figure 2.2 The structure of a typical saturated triacylglycerol molecule from literature (Marangoni, 2013).

As shown in Figure 2.3, TAG molecules can pack in one of two configurations when they nucleate (Acevedo & Marangoni, 2015; Mazzanti, Marangoni, & Idziak, 2005):

1. *tuning fork configuration*: the *sn-1* and the *sn-3* acyl chains pack alongside each other; *sn-2* is alone.
2. *chair configuration:* the fatty acid in the *sn-2* position packs alongside the chain on either the *1* or *3* positions.

Once crystallized, TAG molecules stack in pairs side by side, forming a double (2L) or triple (3L) fatty acid chain length structure (Figure 2.3 (b)) (Jensen & Mabis, 1963, 1966; Peschar et al., 2004). Then, one-molecule thick layers, called lamellae, can be formed by a continuous lateral self-assembly of TAG molecules. The stacking of these lamellae is what forms the crystals (Figure 2.3 (c)). A crystalline domain can be created when the lamellae stack following an epitaxial growth (Figure 2.3 (d)). These single domain crystals have the shape of a thin parallelepiped, and are known as nanoplatelets. The height of a crystalline domain corresponds to the thickness of a TAG nanoplatelet. The three-dimensional fat crystal network is formed via the aggregation of nanoplatelets into larger units (Acevedo & Marangoni, 2015; Mazzanti et al., 2005).
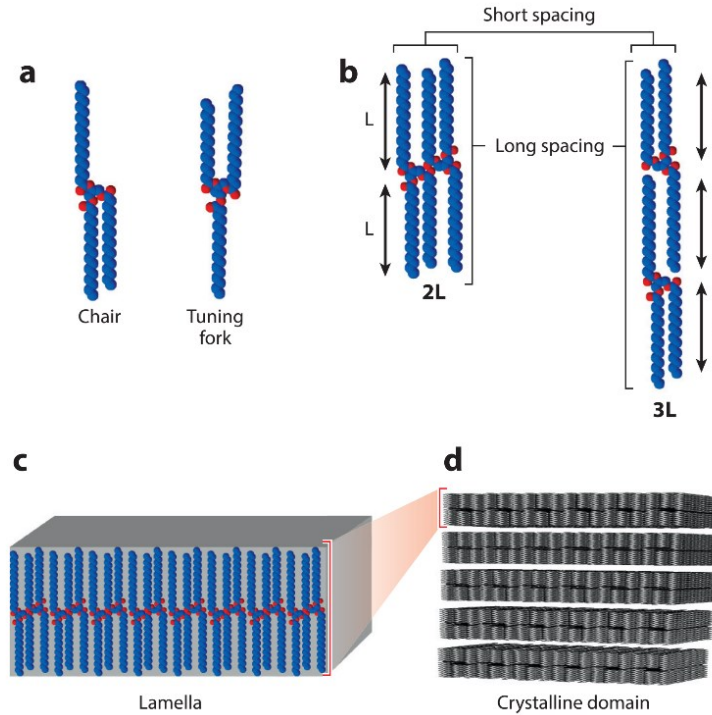
Figure 2.3 (a) Schematic representation of a chair and tuning fork configurations. (b) a double (2L) or triple (3L) fatty acid chain length structure. (c) a lamella formed by a continuous self-assemble of TAG molecules. (d) a crystalline domain created by stacking of several lamellae (Abbreviation: L, fatty acid chain length) from *(Acevedo & Marangoni, 2015)*.

Polymorphism

Duffy (1853) first observed the polymorphism of TAGs. Further studies in the early 1960s, using x-ray diffraction, provided an agreement on the number, structure, and nomenclature of different polymorphic forms of TAGs (Chapman, 1962; Larsson, 1964).

Polymorphism refers to the ability of molecules to form solids with different crystalline arrangements. The crystalline form depends on the arrangement of the molecules within the crystal lattice (Metin & Hartel, 2005). In TAGs, the differences in hydrocarbon chain packing and variations in the tilt angle of the packing lead to different polymorphs.

Apart from the molecular make-up, polymorphism is determined by external factors, chiefly temperature, the rate of crystallization, impurities, shear rate and pressure (Sato, 2001).
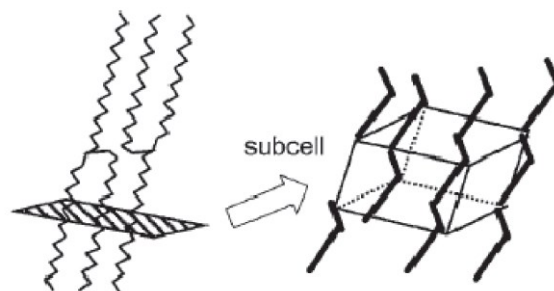
Figure 2.4 Schematic representation of the sub-cell structures of TAGs from *(Sato & Ueno, 2005)*.

As shown in Figure 2.4, the concept of subcell was developed to explain and identify different polymorphs(Vand & Bell, 1951). A subcell refers to an imaginary sub-structure within the fatty acid chains of the TAG. In other words, a subcell structure is defined as a lateral cross-sectional packing mode of the hydrocarbon chains of TAGs (Hagemann & Rothfus, 1983; Van Langevelde, Van Malssen, Hollander, Peschar, & Schenk, 1999; Vand & Bell, 1951).
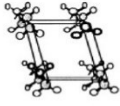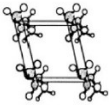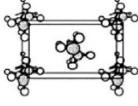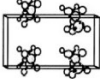
	H	$T_{//}$	$M_{//}$	$O_\perp$	$O'_{//}$
Capital letter Symbol	Hexagonal	Triclinic parallel (//)	Monoclinic parallel (//)	Orthorhombic perpendicular ($\perp$)	Orthorhombic perpendicular ($\perp$)
Arrangement (zigzag aliphatic chains)	rotationally disordered	parallel manner	parallel manner	nearly perpendicular to the neighbors	parallel manner
polymorph	α	β	β	β'	β'
Short-spacing	0.415 nm	0.379 nm 0.39 nm 0.46 nm	0.379 nm 0.39 nm 0.46 nm	0.38 nm 0.42 nm	0.38 nm 0.42 nm
Density	Least dense	Most dense	Most dense	Intermediate	Intermediate
Melting point	Lowest	Highest	Highest	Medium	Medium
Stability	Least stable	Most stable	Most stable	Intermediate	Intermediate

Table 2.1 Characteristics of three important polymorphs found in fats. Modified from (Sato & Ueno, 2005).

Ten types of subcell structures have been indentified in crystalline fats. The five predominant subcell structures are: H (hexagonal), $O_\perp$ (orthorhombic perpendicular), $O'_{//}$ (orthorhombic parallel), $T_{//}$ (triclinic parallel), and $M_{//}$ (Monoclinic parallel). The three most important polymorphs, shown in Table 2.1, are called α, β′ and β in order of thermodynamic stability. They are distinguished by the increasing angle of tilt , with a thinning and tighter packing of the molecular layers, from α to β′ and finally to β. The α polymorph has a hexagonal subcell that is least stable; β′ has a orthorhombic perpendicular sub-cell where hydrocarbon chains are inclined with respect to the basal plane by about 108 degrees (intermediate stability); β has a triclinic parallel sub-cell with the hydrocarbon chains inclined at about 128 degrees (highest stablility) (Takeuchi, Ueno, & Sato, 2003). The denser packing gives increased stability of the polymorphic form (*i.e.,* the hydrocarbon chain packing of the β form is denser than the α form). Stable forms have a higher melting point and higher heat of fusion than the less stable forms (Hagemann & Rothfus, 1983; Li, 2011; Lutton, 1948; Takeuchi et al., 2003).

This type of polymorphism is called monotropic, because the transformations are irreversible. Transformation of one polymorphic form into another always occurs from a less stable form to a more stable one. This process is also known as the Ostwald step rule (Rousset, 2002; Takeuchi et al., 2003). The transformation could take place with or without melting of the solid (*i.e.,* melt-mediated or solid state) as schematically illustrated in Figure 2.5. α, β′ and β forms can form directly from the melt. According to Mutaftschiev (1993), the crystallization normally starts from the presence of thermodynamically unstable phases followed by reorganization to more stable phases, which is from α to β′ and then to β, via polymorphic transition (Mutaftschiev, 1993). The α form has the lowest energy formation barrier (*i.e.,* the least constraints regarding incorporation of TAG molecules from the melt). With time, molecules in the α form can rearrange into more stable forms (*e.g.,* β′ and β) that possess lower Gibbs energy. Polymorphic transformation takes place until molecules adopt an ideal conformation and arrangement with an efficient close packing, and is therefore always an exothermic process in TAGs (Marangoni & Wesdorp, 2013). Fats can also directly transit from α to β in a crystallization process, instead of from α to β′ and then to β. This happens under external forces or due to kinetic factors. However, the

transformation from α to β′ to β is irreversible.

A less stable polymorph can also change towards a more stable one in solid state, though this is a slower process.
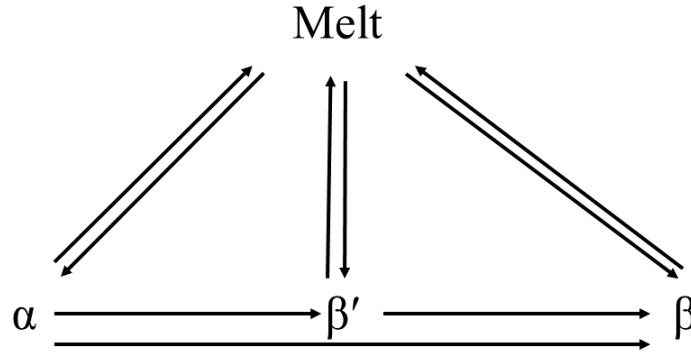
Figure 2.5 Dynamics of polymorphic transformations in TAGs and fats. Adapted from (Marangoni & Wesdorp, 2013).

This thesis is concerned with tristearin or glyceryl tristearate. It is a triglyceride with three units of stearic acid esterified on the glycerol backbone. Like other triglycerides, tristearin can crystallize in three polymorphs, α, β'and β. The thermal properties of tristearin are shown in Table 2.2. (Matovic, van Miltenburg, Los, Gandolfo, & Floter, 2005; Teja, Lee, Rosenthal, & Anselme, 1990).

β		β_2'		α	
T_{fus}	Δh_{fus}	T_{fus}	Δh_{fus}	T_{fus}	Δh_{fus}
K	J·g^{-1}	K	J·g^{-1}	K	J·g^{-1}
345.9	221.6			327.3	144.8
346.0	219.6	336.7	154.2	327.3	128.0
346.6	214.7	336.4		328.1	
344.6				327.6	
346.1		337.1		327.3	
345.6		337.6		327.6	
346.7		336.1		327.8	
		336.4	162.7		
346.3	220.7	337.1	178.4	327.1	162.9
343.1					
	70.4				
345.7	228.0			327.1	162.8
345.5	213.0			326.0	153.6
346.3	211.4	336.7	168.9	328.3	122.6
345.7	216.7	337.5	175.2^a	327.9	126.9

Table 2.2 Table of melting temperatures and enthalpies of fusion of the three important polymorphs (α, β'and β) of tristearin (Matovic, Miltenburg, Los, Gandolfo, & Floter, 2005).

The values used for tristearin in this Thesis are: $\Delta_{fus}H_\alpha$ = 107500 kJ/kmol at 327.2 K, $\Delta_{fus}H_{\beta'}$

= 188160 kJ/kmol at 336.7 K, and $\Delta_{fus}H_\beta$ = 203260 kJ/kmol at 345.75 K. For liquid and solid (α, β'and β) tristearin, its density follows the equation, ρ_{ms} = -0.62911·T + 1084.6 (ρ_{ms} in mol/m³, T in °C). For tristearin, values of specific heat are dependent on the properties and phase: C_p *(liquid)* =1975 J/(mol·K), C_p *(α)* = 1823 J/(mol·K), C_p *(β')* = 1738 J/(mol·K), C_p *(β)* = 1609 J/(mol·K) (Morad, Idrees, & Hasan, 1995).

The relationship between viscosity and temperature of many fluids can be conveniently described by Andrade's logarithmic viscosity equation (Andrade, 1951; Coupland & McClements, 1997; Formo, 1979; Moore, Burkardt, & McEwan, 1956):

$$\ln(\mu) = A + \frac{B}{C + T} \qquad (1)$$

For tristearin, the coefficients are A_s = -0.35895, B_s = 207.48, C_s = 8.1980, are my Andrade fit to the data) (Valeri & Meirelles, 1997). The other important substance in this thesis is the hydrocarbon n-dodecane, used as solvent. Dodecane is a flexible molecule, with a structure homologous to the alkyl chain of the stearic acid substituents in tristearin. In the thesis it is considered to remain only in its liquid state. The crystallization temperature of dodecane is 263.58 K (-9.57 °C) ant its enthalpy of fusion ΔfusH is 36836 kJ/kmol. Dodecane has a specific heat cp = 376.00 J/(mol·K), density ρ = 749.5 kg/m3 at 20 °C, and viscosity η = 1.34 mPa·s at 25 °C (Haynes, 1995). These properties are functions of temperature. The molar density of dodecane can be calculated from ρm = -4.3625·T + 4487.4 (ρm in mol/m3, T in °C). As shown in Figure 2.6, from -5 to 95 °C, the Andrade viscosity equation fits well with viscosity data from NIST (National Institute of Standards and Technology). The coefficients are Ad = -3.2963, Bd = 725.37, Cd = 176.22. This is consistent with other literature reports (Ambrose & Tsonopoulos, 1995; Caudwell, Trusler, Vesovic, & Wakeham, 2004; Rosenthal & Teja, 1989).

11
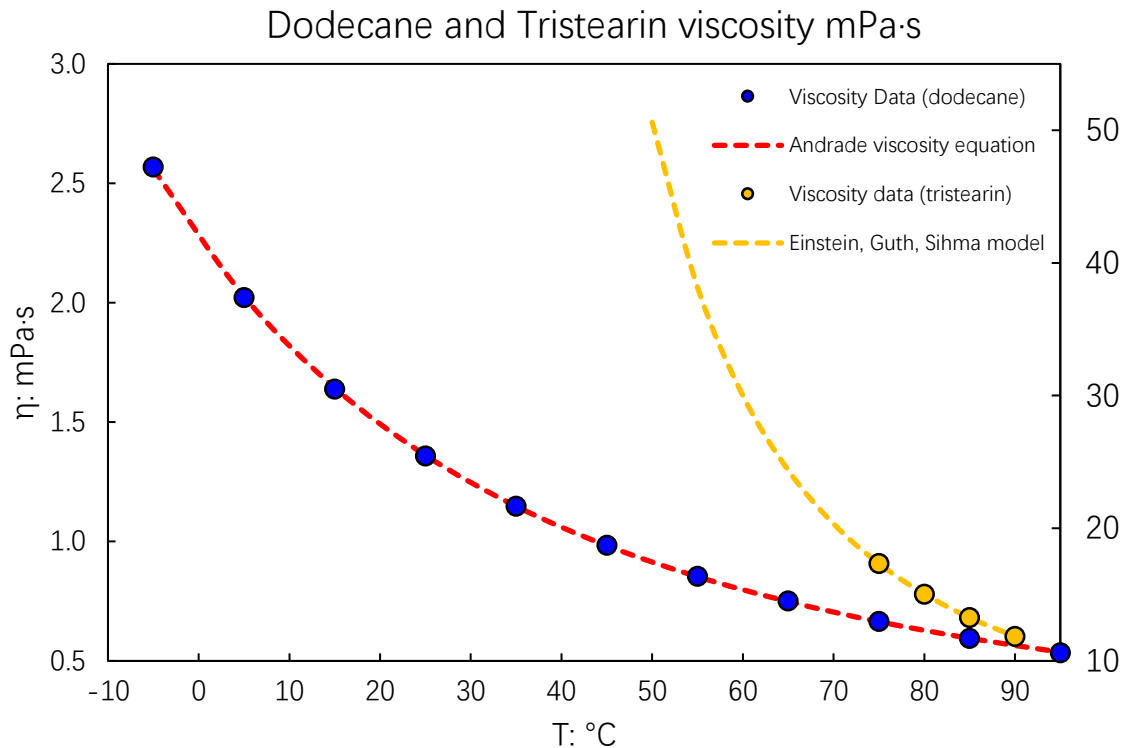
Figure 2.6 Viscosity of dodecane and liquid tristearin as a function of temperature. The blue dots represent the viscosity data for dodecane from references, on the left axis. The red dash line represents the calculated value based on the Andrade viscosity equation (Ambrose & Tsonopoulos, 1995; Caudwell et al., 2004; Rosenthal & Teja, 1989). The yellow dots are values for tristearin from on the right axis (Valeri & Meirelles, 1997), and the dotted line values extrapolated using its corresponding Andrade equation.

Intermolecular forces and movements

In anhydrous fats and oils, there are mainly three physical sources of forces between molecules: London-van der Waals type interactions (charge-fluctuation-induced), electrostatic interactions, and hydrogen bonding (David A, 2013). Van der Waals forces are the interactions between materials that are brought about by interactions between fluctuating atomic electric dipoles induced by fluctuations in the electromagnetic field (Hamaker, 1937; I, 1961; Landau & Lifshitz, 1968; Leckband & Israelachvili, 2001; Lifshitz, 1956). This is the predominant attractive force between alkyl chains.

Electrostatic interactions are the forces between moieties carrying electric charges on sufficiently large spatial scales (or long time scale) (Cevc, 1987, 1990; McLaughlin, 1989). Here, electric multipole (e.g., dipole–dipole) interactions are also considered as electrostatic interactions. Although there is no significant differences in the distance

12

dependence between electric dipole–dipole interactions and van der Waals interactions, the origins and mechanisms of these two interactions are not the same (David A, 2013). The TAGs do not carry net charge, since there is no ionization. However, the glycerol core has six oxygen atoms, three of them carboxylic. The charge density distribution in this part of the molecule makes this region a polar one. The alkyl chains, by contrast, are none-polar. This difference in polarity influences much of the behaviour of the TAG molecules in the liquid and solid phases.

Hydrogen bonding is a weaker Coulombic effect, which is short-range (<0.3 nm) and directional. In anhydrous fats and oils, hydrogen bonding is confined to certain proton-containing moieties (Israelachvili, 2011). Hydrogen bonding is regarded as a combination of van der Waals forces along with attractive electrostatic interactions in nonquantum molecular dynamics. They are virtually absent in the anhydrous mixture tristearin-dodecane studied in this thesis (David A, 2013; Himawan, Starov, & Stapley, 2006; Li, 2011; Mazzanti et al., 2005; Sato, 2001).

2.1.1.2 Effect of Temperature on Crystalline Interplanar Spaces

Crystalline interplanar space

As mentioned before, the stacking of TAG molecules can be in either a double (2L) or triple (3L) fatty acid chain length structure. In 2L and 3L, the height of TAG structure and the distance between TAG molecules are different. The term d-spacing is used to describe interplanar spacings among these structures (Acevedo & Marangoni, 2015; Jensen & Mabis, 1963, 1966; Peschar et al., 2004).

As the smallest building block for a crystal lattice, the unit cell of TAGs has two kinds of d-spacings, long spacings and short spacings (Figure 2.7 (a)). Long spacings refer to the length of a unit cell in c-axis direction, which is corresponding to the distance between ab planes (*i.e.,* thickness of the lamellae) (Acevedo & Marangoni, 2015). According to Chapman (1962), the long spacing is a function of the length of TAG molecules and the angle of tilt of the chains relative to the normal plane (Chapman, 1962). Measurement of long spacings provides insight on how the TAG molecules stack together to form lamellar structures (deMan, 1992; Larsson, 1994; Small, 1966).

Short spacing refers to the cross-sectional packing of the hydrocarbon chain. In the unit cell there are smaller repeating units, the subcells, along the acyl chain direction. In this subcell, the short spacing is often independent of the chain length (Figure 2.7 (b)) (Larsson, 1966). The Short spacings provide information about the lateral structure and the subcell structure. The identification of different polymorphic forms of fats can be achieved based on the specific set of XRD reflections of one chain-packing subcell (Acevedo & Marangoni, 2015). For example, the α form has a single and broad line at 4.15 Å; the β' form displays two strong lines at 4.2 Å and 3.8 Å (often accompanied by two weaker ones); and the β form is characterized by a strong line at 4.6 Å (S.E.Friberg & K.Larsson, 1997).
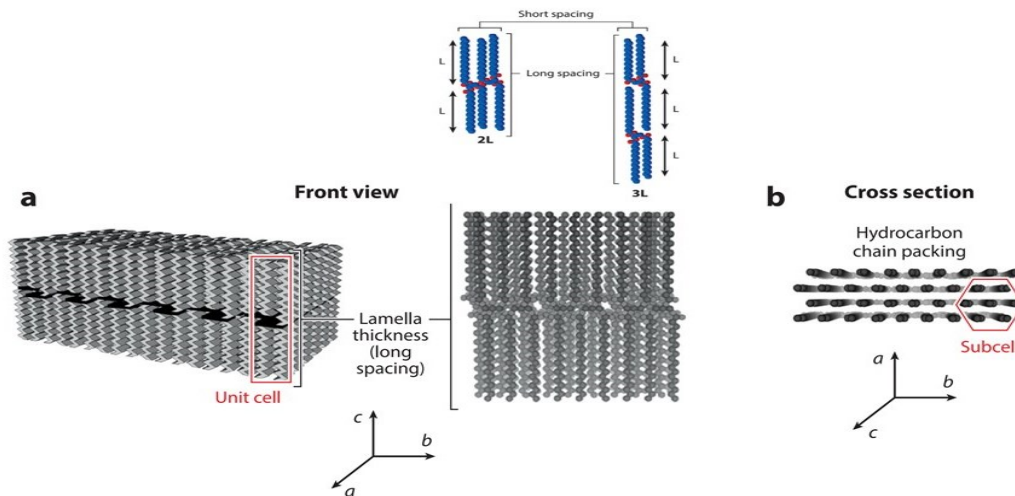
Figure 2.7 Schematic representation of interplanar among spacing of TAG molecules. Modified from *(Acevedo & Marangoni, 2015)*.

Bragg's law

Bragg et al., (1933) found that x-ray beams can be diffracted from the repeating atomic planes in a crystal lattice. In a diffracted x-ray beam, the constructive interference takes place when the distance traveled by different parallel diffracted x-rays differs by an integer number (n) of the incident wavelength (λ). If the crystal lattice is considered as a series of atomic planes, parallel to each other and separated a distance d apart, the path difference for x-ray reflected from adjacent planes at different reflection angles (θ) can be described by Bragg's law (Figure 2.8) (Bragg et al., 1933):

$$n\lambda = 2d \sin\theta \qquad\qquad (2)$$

- where λ is the wavelength of the x-ray, θ is the scattering angle and n is an integer representing the order of the diffraction peak.
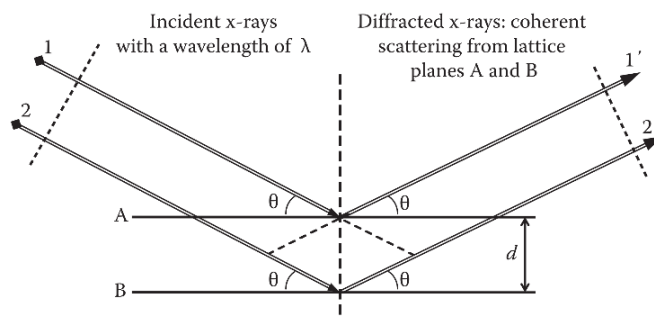
Figure 2.8 Geometry of the reflection of x-ray from crystal planes used in the derivation of Bragg's law from (Marangoni & Wesdorp, 2013).

The angle at which constructive interference occurs can be determined from the Bragg's equation. The Bragg law is valid when the atoms are replaced by molecules or collections of molecules, such as colloids, polymers, proteins and virus particles (Bragg et al., 1933; Li, 2011).

In fat lamellae, the difference in hydrocarbon chain packing results in different polymorphic forms. Thus, they scatter x-rays in different ways. As discussed earlier, an x-ray beam can be scattered into two major regions, the wide-angle region and the small-angle region. The wide angle region provides the short spacing data, with valuable information for the identification of polymorphic forms and phase transitions (Li, 2011). Vand & Bell (1951) succeeded in determining the x-ray diffraction patterns from the hydrocarbon chains of TAG molecules (Vand & Bell, 1951), and used this to establish the concept of 'subcell'.

Effect of temperature on crystalline interplanar spaces

Of particular interest for this thesis is the study by Lavigne, Bourgaux, & Ollivon (1993). They used XRD from a synchrotron high-intensity beam to dynamically observe phase

transitions of SSS. The short-spacings and long spacings for α, β', and β SSS are summarized in Table 2.3 (F. Lavigne, C. Bourgaux, M. Ollivon., 1993).

	Tmelting	short spacings	long spacings
	(°C)	(Å)	(Å)
α	54,5	4,1-4,2	50,6
β'	64,5	4,2 ; 3,8	46,2
β	72,5	4,6 ; 3,85 ; 3,70	45

Table 2.3 Thermal and structural features varieties of SSS. of SSS polymorphs from *(Lavigne, Bourgaux, & Ollivon, 1993)*.

In that investigation on pure tristearin (SSS), Lavigne, Bourgaux, & Ollivon. (1993) also combined Differential Scanning Calorimetry (DSC) with Small-Angle X-ray Diffraction. In Figure 2.9., short and long spacings are presented as 3D plots versus temperature (heating rate: 2 °C /min).
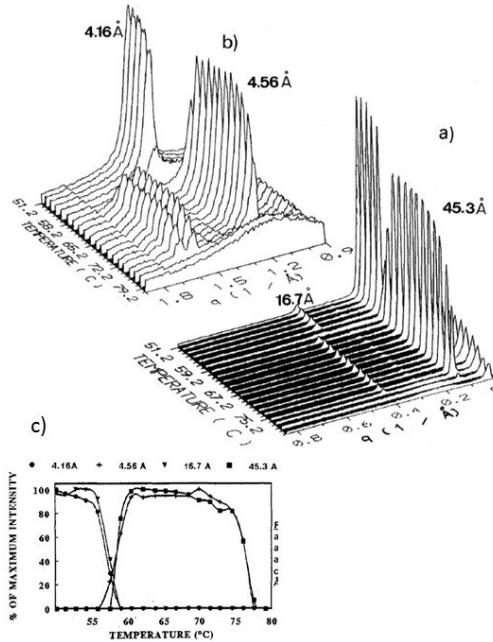
Figure 2.9 Short and long spacings are presented as 3D plots versus temperature. (a). Evolution of long spacings during the α to β liquid transitions of SSS (Heating rate= 2 C°/min). (b). Evolution of short spacings during the α to β liquid transitions of SSS (Heating rate= 2 C°/min). (c). Distribution of the different polymorphs as a function of temperature as obtained by the analysis of peak intensities corresponding to long and short spacings (4.16 and 16.7 Å correspond to α polymorph; 4.56 and 45.38 Å correspond to β polymorph. Adopted from (Lavigne et al., 1993).

This combined method allowed the dynamical observation of phase transitions of SSS. As shown in Figure 2.9 (a) and (b), below 55°C the short spacing patterns give a single sharp

peak at 4.16 Å, while the long spacings patterns give a main diffraction line at 50.1 Å with its second and third orders (25.7 and 16.7 Å respectively). These correspond to the α polymorph.

From 53.8 to 58.5°C, the first peak (50.1 Å) and third peak (16.7 Å) simultaneously vanish. Then a new set of long spacings (45.3 Å (n= I) and 15.1 Å (n=3)) and short spacings (4.6, 3.9, and 3.8 Å) appear, which are close to previously observed values for β SSS.

As shown in Figure 2.9 (c), the intensities of these new peaks increase as temperature increases from 60 °C and reach their maxima around 62 °C. The melting of the sample starts at around 70 °C. At 75 °C, the broad peaks typical of liquid samples can be seen (Lavigne et al., 1993). Eventually, above 79 °C only the liquid remains. Kellens, Meeussen, Riekel, & Reynaers (1990) reported similar results from the diffraction patterns of tripalmitin during its α-to-β transition (Kellens, Meeussen, Riekel, & Reynaers, 1990).

2.1.1.3   Thermodynamics of Crystal-Liquid Equilibria

A single component substance may co-exist in different phase in equilibria under certain sets of conditions. As shown in Figure 2.10, in the region AOB/AOC/COB, a single component substance is one phase, which is uniform not only in chemical composition but also in the physical state. Different phases are separated from one another by one or more abrupt interfaces (AO/CO/BO) (Bokshteĭn, B. S., 2005).
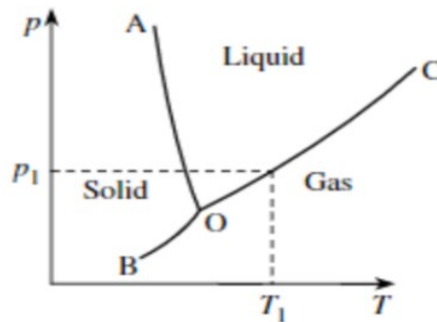
Figure 2.10 A typical p-T diagram for a one-component system. AO, OB, and OC lines represent conditions for which two phases are in equilibria. Three phases simultaneously co-exist at point O (triple point). Adapted from (Bokshteĭn, B. S.2005).

Therefore, for a condensed system (weakly dependent on the pressure, the pressure can be treated as fixed), the number of degrees of freedom can be calculated as (Bokshteĭn, B. S., 2005):

$$F = C + 1 - P \qquad (3)$$

- Where: C is the number of components; P is the number of the phase; F is the number of degrees of freedom;

For a pure component alone, that has no polymorphism, F=1+1-2=0, which means that equilibria only occur at melting temperature. The number of degrees of freedom associated with the equilibria in the solid-liquid mixture in this thesis applies for each polymorphic form separately.

The equilibrium condition, in fact, precludes the coexistence of two or more monotropic polymorphic phases. What happens is that one or more of them is not in equilibrium. For instance, if we are at x= 0.006 and T = 40 °C, the solution is in 'equilibrium' with a β' solid. It is not, however, in equilibrium with a β or α solid.

The kinetic coexistence of several polymorphs is an unstable state, not an equilibrium state. One single polymorph is in a metastable state, if the combination (x, T) is on its line. If the polymorph is the most stable one, then there is a condition of real equilibrium.

The condition of equilibrium in a mixture depends on the partial molar Gibbs energy of each component. This partial Gibbs energy is often called the chemical potential of that component, and is represented by the Greek letter μ. The phase equilibria condition requires that the chemical potential of each component in each phase be equal to that in any other phase:

$$\mu^{solid}(p,T) = \mu^{liquid}(p,T) \tag{4}$$

In the single-component system this can be simply expressed as (Bokshteĭn, B. S., 2005):

$$\mu^{solid} = \mu^{liquid} \tag{5}$$

A convenient zero reference for the chemical potential of the solute is its pure solid state, at its melting temperature, T_m. At a temperature $T < T_m$, the partial Gibbs energy in the solid state and the partial Gibbs energy in its liquid state must be equal, for phase equilibrium to exist. These chemical potentials (*i.e.* partial Gibbs energies) are:

$$\mu^s = \int_{T_m}^{T} c_p^S dT - T \cdot \int_{T_m}^{T} \frac{c_p^S}{T} dT \tag{6}$$

$$\mu^{liq} = \int_{T_m}^{T} c_p^{liq} dT - T \cdot \int_{T_m}^{T} \frac{c_p^{liq}}{T} dT + \Delta H_m - T \cdot (\Delta S_m + R \cdot \ln(x)) \tag{7}$$

Where: x is the mol fraction of solute in the solution, kmol (SSS)/ kmol solution; R is universal gas constant, kJ/(kmol·K); ΔH_m is melting enthalpy of the solute, kJ/kmol (SSS); T_m is the melting absolute temperature of the solute, SSS, in K. T is expressed in K. The term $R \cdot \ln(x)$ is the entropy of mixing of a binary solution.

At equilibrium the equality of chemical potentials is:

$$\int_{T_m}^{T} c_p^S dT - T \cdot \int_{T_m}^{T} \frac{c_p^S}{T} dT = \int_{T_m}^{T} c_p^{liq} dT - T \cdot \int_{T_m}^{T} \frac{c_p^{liq}}{T} dT + \Delta H_m - T \cdot (\Delta S_m + R \cdot \ln(x)) \tag{8}$$

In the special case when $c_p{}^s \approx c_p{}^{liq} \approx$ constant the integral terms cancel each other. If there is no mixing excess enthalpy, this equation simplifies to

$$0 = \Delta H_m - T \cdot (\Delta S_m + R \cdot \ln(x)) \tag{9}$$

Replacing $\Delta S_m = \Delta H_m / T_m$, and rearranging the terms, we obtain what is known as the Hildebrand equation (Benesi & Hildebrand, 1949):

$$\ln(x) = \left(\frac{-\Delta H_m}{R}\right)\left(\frac{1}{T_m} - \frac{1}{T}\right) \qquad (10)$$

It shows how the saturation concentration of the solution depends on the temperature, T. Due to the simplification of specific heats, only an approximate concentration can be estimated using Hildebrand's equilibrium equation for ideal solutions (*i.e.* regular and athermal).

Plots of the Hildebrand equation are shown in Figure 2.11, on a semilog scale. They were made using the thermodynamic properties for each polymorph of SSS. They plot the mol fraction of SSS in a non-interacting solvent, as a function of temperature, that is in equilibrium with the pure solid solute, in the polymorphic form indicated. The dotted line indicates the concentration of SSS solutions used in this study, to provide a sense of 'location' of these ideal curves within this Thesis.
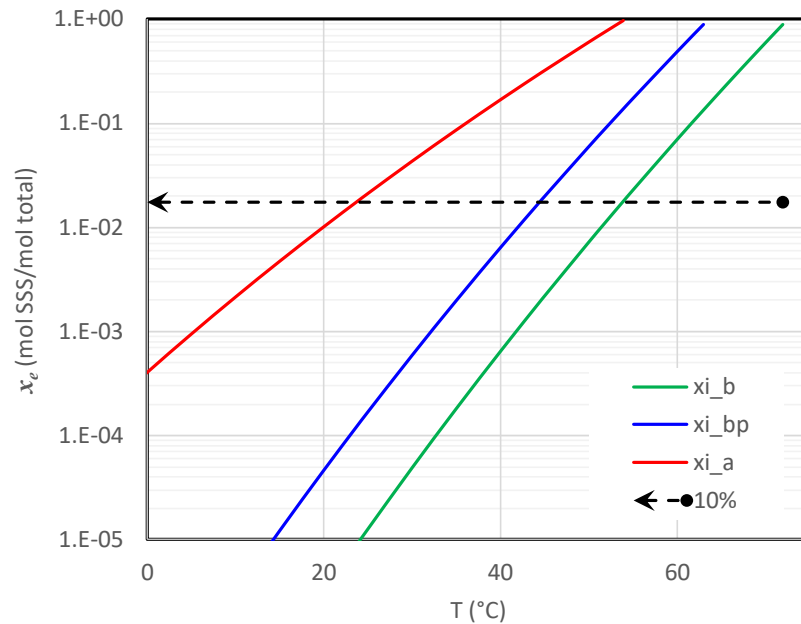
Figure 2.11 Ideal equilibrium mol fraction of tristearin, Xe, in a dodecane solution, as a function of temperature. Computed using Hildebrand's equation, each line corresponds to a polymorphic form of the pure solid tristearin, in equilibrium with the solution. Red is for α, blue for β', and green for β. The dotted line represents the mole fraction of the 10% tristearin in dodecane solution used in this Thesis.

At a given temperature and composition of the solution there is only one possible 'equilibrium', so long as that combination lies on one of the lines. The α and β' are in fact

metastable equilibria, because at that temperature and liquid composition, there will always be a possible phase arrangement with lower Gibbs energy, *i.e. β*. It will tend to reduce the liquid composition by crystallizing into the more stable form. The dotted line indicates the concentration of SSS solutions used in this study, to provide a sense of 'location' of these ideal curves within this Thesis.

2.1.2   Microstructures

2.1.2.1   Crystal Networks

At the nanostructure level (0.4-200 nm), TAG molecules can adopt ''tuning fork" or ''chair'' conformations, packing into lamella. Then a nanoplatelet can be formed by the epitaxial growth of these TAG lamellae (approximately 7 to 10 layers thick). The thickness of a nanoplatelet can be determined via Scherrer analysis of the small-angle X-ray diffraction data (Marangoni et al., 2011; West, 1984).

At the microstructural level (1 to 200 μm), a large polycrystalline particle can be created by the aggregation of primary nanoplatelets. At this level, there are various kinds of crystal habits, such as spherulites, needle-like crystals, micro platelets, disordered crystal aggregates, spherical crystal aggregates, fractal-like aggregates, and even some morphologies that defy proper description. The microstructural level structure of fat has a significant influence on the macroscopic properties of a fat network (Marangoni, 2013).

2.1.2.2   Mechanical Characteristics

The mechanical characteristics of fats depend on serval factors: the molecular structure, the interaction and organization of triacylglycerol molecules, and the concentration and the morphology of fat crystals (Marangoni & Narine, 2002; Walstra, 2003).

The rheological characteristics of fats are a result of the combined effects of solid fat content (SFC) and the microstructural organization of the fat network (*i.e.,* the shape, size, and spatial distribution pattern of the fat crystals) (Mazzanti, Li, Marangoni, &Idziak, 2011).

In the food industry, "solid fat" refers to a matrix of fat crystals holding a liquid oil mixture. Most liquid oils are considered as Newtonian liquids (*i.e.,* a fluid that exhibits a viscosity that remains constant regardless of any external stress placed upon it). These liquid oils

have intermediate viscosities (between 30 and 60 mPa·s at room temperature), which tends to decrease steeply with increasing temperature. The relationship between viscosity and temperature can be conveniently described by Andrade viscosity equation, as mentioned in 2.1(Andrade, 1951; Coupland & McClements, 1997; Formo, 1979).

Solid fats normally show a type of rheological behavior known as plasticity, which is ascribed to their ability in formation of a three-dimensional network of tiny fat crystals spread in a liquid oil matrix (Moran, 1994; Walstra, 2003). Fat crystal networks will behave like solid when below its critical yield stress (τ_0) (*i.e.,* fat crystal networks are not interrupted due to the unbroken weak bonds under small deformation condition). However, a plastic material will behave like a liquid when above τ_0 (i.e., fat crystals slide past one another and start to flow due to the breakage of weak bonds) (Walstra, 2003). Fat crystals can form new bonds with their neighbors and change the network to a "solid state" when the flow ceases (Damodaran, Parkin, Fennema, & Parkin, 2008).

However, in some fats, the yield stress tends to be a range of applied stresses rather than a well-defined value. It means that these fats show some flow characteristics (*e.g.,* viscoelasticity) below the yield stress, yet they don't flow. When they finally flow, they exhibit non-Newtonian behaviors (*e.g.,* shear thinning). This is because the disruption of the fat crystal network structure is not a instantaneous process when force is applied (Sherman, 1968).

2.2　Process Kinetics

2.2.1　Undercooling

2.2.1.1　Concept

When cooling a liquid below its melting temperature, nuclei would usually quickly form and grow out of the surrounding liquid. Liquid fats, however, can persist for a considerable time in their original liquid phase before any crystallization happens, even well below their melting point. The time required for the crystallization to begin depends on the temperature. This onset time decreases as the difference between the melting point and the temperature increases. The thermal process of lowering the temperature of a liquid fat below its melting temperature without solidification is called undercooling or supercooling.

We use the term "degree of undercooling (ΔT)" as the difference between the equilibrium melting temperature of the material (T_m) and its actual temperature (T) (*i.e.,* $\Delta T = T_m - T$). This is done to avoid confusion with the thermal process, also named "undercooling". The degree of undercooling (ΔT) is affected by many factors, such as the chemical structure of the lipid, the presence of any contaminating, the microstructure of the lipid phase (*e.g., bulk vs. emulsified oil*), and the application of external forces (*e.g., shear force, sonication, pressure*). If the single component fat is clean, the degree of undercooling (ΔT) could even be greater than 10 C° before any crystallization is observed (McClements & Decker, 2008).
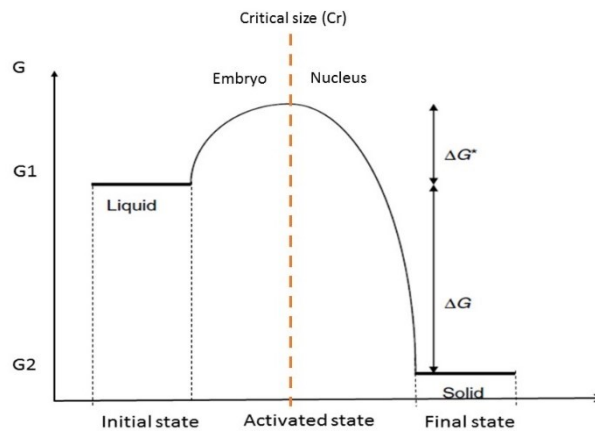
Figure 2.12 Schematic representation of the Gibbs energy change associated with the formation of nuclei. Modified from (McClements & Decker, 2008).

The undercooling is closely related to the Gibbs energy change between the liquid and solid phases (Figure2.12). A very useful way to use this relationship is to compare the Gibbs energy of the liquid with the Gibbs energy of the solid, at any given temperature. This comparison can be made by the thermodynamic equation:

$$\Delta G_{L \to S} = \Delta H_{L \to S} - T \Delta S_{L \to S}. \tag{11}$$

Where:

- $\Delta H_{L\text{-}S}$ (enthalpy term): this term comes from the difference in the overall strength of the molecular interactions between triacylglycerols in the liquid and the solid state. TAG molecules pack more densely in the solid state than in the liquid state. This corresponds to the greater strength of the bonds between TAG molecules in the solid state. Thus, $\Delta H_{L\text{-}s}$ is negative ($\Delta H_{L\text{-}s} < 0$).

- ΔS_{L-S} (entropy term): this term comes from the difference between the organization of the molecules in the liquid phase, and their organization in the solid phase. The entropy of the TAG molecules in the liquid state is greater than that in the solid state. Thus, ΔS_{L-S} is negative ($\Delta S_{L-S} < 0$).

When the temperature is below the melting point of TAG molecules, the enthalpy term 'dominates' the entropy term (absolute value: $\Delta H_{(L \to S)} > T \cdot \Delta S_{(L \to S)}$; $\Delta H_{L-s} < 0$, $\Delta S_{L-S} < 0$, and $T > 0$). (Atkins, 1994; Hartel, 2001; Walstra, 2003). Thus, $\Delta G_{(L \to S)}$ is negative ($\Delta H_{(L \to S)}$ - $T \Delta S_{(L \to S)} < 0$). This means a liquid-to-solid phase transition can happen spontaneously. However, when undercooled, crystals may not appear in a short time frame, even though the solid phase has a lower Gibbs free energy than the liquid phase (thermodynamically favored).

This is because the molecules must overcome an activation energy barrier (ΔG^*) to be able to actually form nuclei. This activation barrier (ΔG^*) reflects the difference between the average and the individual Gibbs energy. The Gibbs energy of individual molecules follows a probability distribution, which means that only a small number of molecules are in a high Gibbs energy level (*i.e.* in the activated state). This is shown in Figure2.13. Other molecules, with low energy, must go through a local thermal activation process, where the Gibbs energy can be changed. After local thermal activation, the Gibbs energy will be the sum of the thermal energy and the entropy term at a higher temperature and the original Gibbs energy. To transit into a solid, molecules must be more organized, which means they have a smaller entropy than they had in the liquid state. Thus, a positive Gibbs energy change ($\Delta G > 0$) occurs after this local thermal activation.

If the Gibbs energy after the local thermal activation is insufficient to overcome the activation barrier ΔG^*, the higher Gibbs energy molecules have formed an unstable embryo, which will melt and be incorporated back into the liquid. If the Gibbs energy after local thermal activation is enough to overcome this barrier ΔG^*, the higher energy molecules could form a stable nucleus, and will release the enthalpy associated with its formation, to reach the lower Gibbs energy level of the solid nucleus.

The stability of the crystal nuclei formed in the liquid oil determines the height of the activation energy barrier (ΔG^*) (McClements & Decker, 2008). The ΔG^* is the net result of two terms: the negative Gibbs energy change due to the crystallization of a volume of solid ΔG_v, and the positive Gibbs energy change ΔG_s, due to the formation of a new interface between the solid and the liquid:

- ΔG_v: Enthalpy and entropy changes occur in the interior of the nucleus owing to the phase transition. ΔG_v is proportional to the volume of the nucleus formed.
- ΔG_s: A solid-liquid interface appears when a nucleus is formed. This creation involves an increase in Gibbs energy, that is called interfacial energy. ΔG_s is proportional to the surface area of the nucleus formed.

The net Gibbs free energy change ΔG of the formation of a spherical nucleus (liquid to solid) is, therefore, a combination of a volume and a surface term (Hartel & Schwartzberg, 1992; Hartel, 2001):

$$\Delta G = \Delta G_V + \Delta G_s = -\frac{4}{3}\pi r^3 \frac{\Delta H_m \Delta T}{T_m} + 4\pi r^2 \gamma_i \qquad (12)$$

- Where: r is the radius of the nuclei, ΔH_m is the melting enthalpy change per unit volume (solid to liquid transition, which is positive), and γ_i is the solid–liquid interfacial energy, ΔT is the degree of undercooling, and T_m is the sbsolute temperature at the melting point.

When the size of the nuclei increase, the surface area to volume ratio will decrease. The surface contribution ends dominating small nuclei formation, while the volume contribution dominates for large nuclei. Therefore, there is a maximum overall net Gibbs free energy when nuclei form at a critical radius (r*) (McClements & Decker, 2008):

$$r^* = \frac{2\gamma_i T_m}{\Delta H_m \Delta T} \qquad (13)$$

When spontaneously formed, the stability of a spherical nucleus depends on its radius. A spherical nucleus with a radius below the critical size (radius) r* will tend to dissociate to reduce the Gibbs free energy of the system. On the other hand, above the critical size r*, a spherical nucleus will tend to grow into a crystal.

TAG molecules, however, do not crystallize in neat spherical nanoparticles. They, instead, form nanoplatelets. If the critical thickness of one of these nanoplatelets is ξ_c, then the aspect ratios of the nanoplatelet can be defined for width $a \cdot \xi_c$, and length $b \cdot \xi_c$. Thus, the geometrical factors, surface area A and volume V, can be defined as (Wang, 2016):

$$A = g_s \cdot \xi_c^2 \quad g_s = 2(a + b + b \cdot a) \tag{14}$$

$$V = g_v \cdot \xi_c^3 \quad g_v = b \cdot a \tag{15}$$

The net Gibbs energy written as a balance between two Gibbs energy terms is (Wang, 2016):

$$\Delta G_c = \frac{V}{V_m^s} \Delta G_m - A \cdot \gamma_T \tag{16}$$

- Where: Surface tension term: $A \cdot \gamma_T$, A is the surface area created; γ_T is the interfacial energy in J/m^2); Bulk energy term: $\Delta G_m \cdot n$, ΔG_m is the Gibbs energy difference of bulk crystallization per mole, in J/mol; 'n' is the number of moles of material crystallized, $n = V/V_m^s$. V is the volume of the nanoplatelet, and V_m^s is the molar volume of a solid molecule (Bondi, 1964). The critical size of a nucleus of thickness can be then determined by (Wang, 2016):

$$\Delta G_c = \frac{V}{V_m^s} \Delta G_m - A \cdot \gamma_T \implies \Delta G_c = \frac{g_v \cdot \xi^3}{V_m^s} \Delta G_m - g_s \cdot \xi^2 \cdot \gamma_T \tag{17}$$

$$\Delta G_m = \Delta H_m - T \cdot \Delta S_m = \Delta H_m - T \cdot \frac{\Delta H_m{}'}{T_m} = \Delta H_m \cdot \left(\frac{T - T_m}{T_m}\right) \tag{18}$$

$$\Delta G_c = \frac{g_v \cdot \xi^3}{V_m^s} \Delta H_m \cdot \left(\frac{T - T_m}{T_m}\right) - g_s \cdot \xi^2 \cdot \gamma_T \tag{19}$$

$$\frac{\partial(\Delta G_c)}{\partial \xi} = \frac{3g_v}{V_m^s} \Delta H_m \cdot \left(\frac{T - T_m}{T_m}\right) \cdot \xi^2 - 2g_s \cdot \xi_c \cdot \gamma_T = 0 \implies \tag{20}$$

$$\xi_c = \frac{2g_s \cdot V_m^s \cdot \gamma_T}{3g_v \cdot \Delta H_m} \left(\frac{T_m}{T - T_m}\right)$$

$$\xi_c = s_f \cdot \gamma_T \left[\frac{V_m^s}{\Delta H_m} \left(\frac{T_m}{T - T_m} \right) \right] \quad \therefore s_f = \frac{2g_s}{3g_v} \qquad (21)$$

$$\Delta G_c = s_g \cdot \gamma_T \left[\frac{V_m^s}{\Delta H_m} \left(\frac{T_m}{T - T_m} \right) \right]^2 \quad \therefore s_g = s_f^2 (g_s - g_v \cdot s_f) \qquad (22)$$

It is possible that the nucleus is a monolayer lamella, in which case its thickness is the 'd' spacing of the polymorph. In the bulk the d spacing values are 5.06 nm for α, 4.62 nm for β', and 4.50 nm for β. However, in nanoplatelets with one up to a few lamellar layers, the 'bulk' is not quite real 'bulk' since all the molecules are on the surface (Kiselev & Lombardo, 2016; Unruh, Bunjes, Westesen, & Koch, 1999). A small difference in interfacial energy can result in a large difference in nucleation events (Timms, 1995). Even so, for the same kind of fat, nucleation may not be the same because interfacial energy γ_i varies in different polymorphs (Boistelle, 1988).The influence of interfacial energy is greater than the temperature driving force (Metin & Hartel, 2005).

Consider a parallelepiped nucleus that has the same proportions as a final crystal in its width and length, *e.g.* 3:10. Assume it consisted of a single lamella of tristearin molecules pairs in the α form (ξc ≈5.1 nm, a / b = 3/10). The interfacial energy needed to generate new area is different for each pair of surfaces. The interfacial energy of the surface (a×b) is the lowest, followed by (a×1), and finally (1×b). Physically it means that it is easier to incorporate a molecule onto surface (1×b), which produces an effective increase in the other two areas, but not in (1×b). Then it is easier onto (a×1). Incorporating molecules onto (a×b), *i.e.* adding molecules perpendicular to the large surface to add one lamellar thickness, is the most difficult process. Thus, the crystal nucleates, and grows, anisotropically.

The value of interfacial energy γ_T in equation (16) is a surface-averaged value of the three individual interfacial energies. The values will be different when crystallizing from the melt instead of from a solvent like dodecane. However, the interfacial energies will still maintain the order from smaller to larger related to the surfaces.

$$\gamma_T = \frac{(a \cdot \gamma_b + b \cdot \gamma_a + b \cdot a \cdot \gamma_c)}{(a + b + b \cdot a)} \qquad (23)$$

The phase transition can occur throughout a whole range of metastable conditions until the system reaches its stable equilibrium. The crucial factor is the rate of phase transformations, which depends on the process conditions (*e.g.* the degree of undercooling, cooling rate, supersaturation, *etc.*). The thermodynamic-kinetic analysis allows us to understand the metastable states and resultant structures. For example, the degree of undercooling determines the packing time of the fat molecules during liquid-solid phase transition. Under a sufficiently high degree of undercooling, TAG molecules are hard to align due to relatively long hydrocarbon chains. The onset time is not sufficient for TAG molecules to pack in the most thermodynamically stable configuration (high melting point). Thus, liquid fat tends to crystallize first in a metastable form. Campos, Narine, & Marangoni (2002) studied anhydrous milk fat (AMF) under a rapid cooling rate (5˚C/min) and a slow cooling rate (0.1 ˚C/min). When cooling rapidly, AMF crystallized in metastable polymorphic forms (α, β' forms). However, when cooled slowly, AMF had a lower solid fat content (SFC) and was in a more stable polymorphic form (β) (R. Campos, Narine, & Marangoni, 2002).

This indicates that the activation energy barrier (*) of the metastable form is lower than that of its 'cousins'. Thus, the metastable nuclei can form more readily than those of the stable forms. Moreover, the metastable form has the smallest Gibbs free energy difference with respect to the liquid (ΔG_n). This indicates its poorer thermodynamic stability (lower melting point) when compared to the other forms, but also explains why it is possible to crystallize it faster. After its formation, it is common that the metastable form transforms into a more stable one. The metastable form can sometimes be kept without change for times long enough to be considered permanent, from a practical point of view. This is accomplished by lowering the temperature, and keeping the material solid.

2.2.1.2 Compositional undercooling

As we discussed above, undercooling is very important in single component crystallization. For a multi-component system, undercooling now not only depends on the temperature but also on the composition of the mixture. There are two main kinds of mixtures, solutions (solvents do not crystalize) and melts (solvents can partially crystallize). Undercooling in a mixture is termed "compositional undercooling". The concept of compositional

undercooling was first introduced by (Rutter & Chalmers, 1953). In their study of the instability of the interface in impure metals, they suggested that the cellular substructure at the interface was due to compositional undercooling. This phenomenon is closely related to the diffusion process ahead of the moving interface. We can study this compositional undercooling in a coordinate system moving with the interface (Figure 2.13):
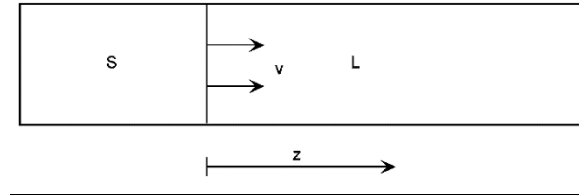
Figure 2.13 Moving coordinate system for analyzing steady-state growth. The coordinate z is measured away from the moving interface; v is the velocity of moving the interface; S is the solid phase and L is the liquid phase. Adapted from (Jackson, 2004a).

When moving away from the interface at velocity u, the equation for steady-state diffusion in the coordinate system can be written (Jackson, 2004):

$$D\frac{d^2C}{dz^2} + u\frac{dC}{dz} = 0 \qquad (24)$$

- where C is the composition in the liquid, D is the diffusion coefficient, and z is the distance from the interface.

The value of the molecular diffusivity "D_{sd}" of tristearin in dodecane, as a function of temperature and composition, could be roughly estimated from a correlation for alkanes developed by (Erkey, Rodden, & Akgerman, 1990),:

$$\frac{10^9 D_{sd}}{\sqrt{T}} = \frac{94.5}{M_s^{0.239} M_d^{0.781} (\sigma_s \sigma_d)^{1.134}} (V - bV_0) \qquad (25)$$

$$bV_0 = b \cdot \frac{N \cdot \sigma_d^3}{\sqrt{2}} \qquad (26)$$

$$b = 1.206 + 0.0632(\frac{\sigma_s}{\sigma_d}) \qquad (27)$$

- Where: D_{sd} is in m²/s; T is in Kelvin, molecular weights are in g/mol, and the molar volumes are in cm³/mol; V, is the close packed hard sphere volume of the solvent, 237.8 cm³/mol for dodecane; σ_s and σ_d are the effective hard sphere diameters of

the molecules of the solute, σ_s (tristearin) =12.53 Å, and solvent, σ_d (dodecane) = 7.44 Å; and N is the Avogadro number (6.0221×10^{23} molecules/mol)

Therefore, D_{sd} can be calculated as a function of temperature. Figure 2.14 shows its values, along with a linear approximation.

D_{sd} ($\times 10^{-10}$ m²/s)
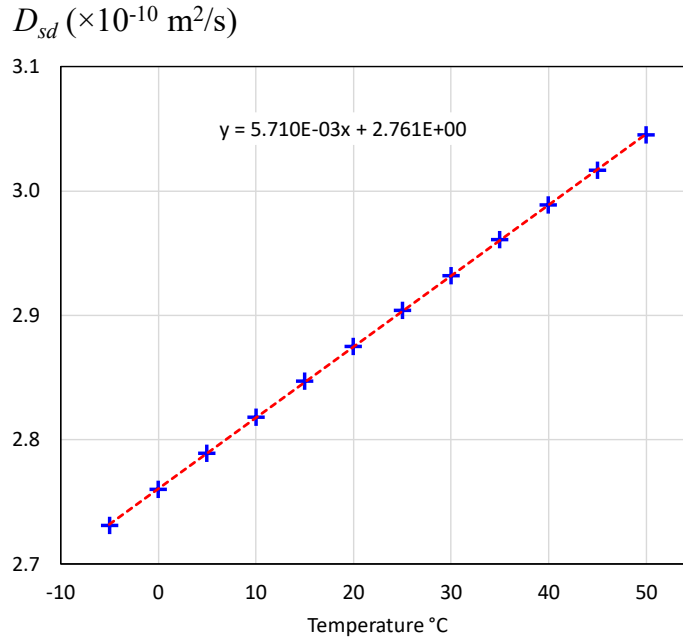
Figure 2.14 Estimated value of the molecular diffusivity "D_{sd}" as a function of temperature. The values in the "y" axis must be multiplied by 10^{-10}.

The concentration distribution can be written as (with regard to equation 24) (Jackson, 2004):

$$C = C_\infty + C_\infty \left(\frac{1}{k} - 1\right) \exp\left(-\frac{u \cdot z}{D}\right) \tag{28}$$

- where C_∞ is the initial and bulk concentration of the liquid in kmol/m³, and k is the equilibrium segregation coefficient, which is the ratio of the composition in the solid to the composition of the liquid, ($k = C_S/C_L$) at the interface. In a solution, as is the case for this thesis, for concentrations expressed as mole fractions, $k_x = 1/x$. This is because the solid is pure tristearin, and therefore its mole fraction is one in that phase.
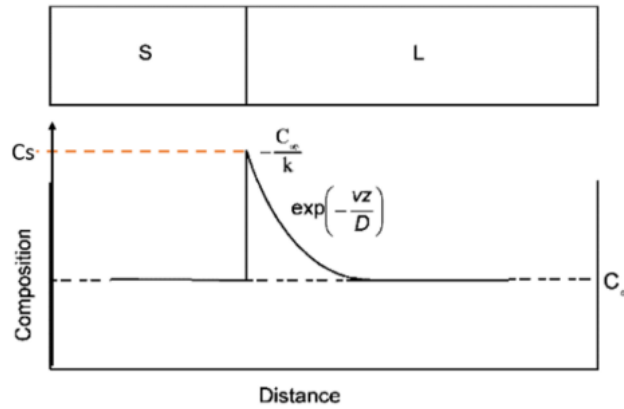
a.
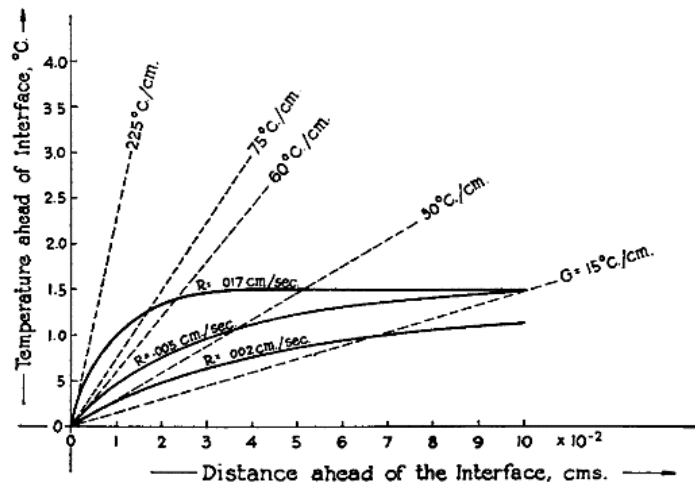
b.

Figure 2.15(a) The steady-state concentration distribution ahead of a moving interface. Adapted from (Jackson, 2004) (b) The original illustration of constitutional supercooling. Adapted from (Sekerka, 1965).

The mol fraction expression for diffusion becomes very cumbersome, since the relationship between molar concentration and mol fraction is given by

$$C = \frac{1}{\Delta V^l + \frac{V_d}{x}} \qquad (29)$$

- Here ΔV^l is the difference between the molar specific volumes of tristearin, V_s, and dodecane, V_d *(Figure2.16)*: $\Delta V^l = V_s - V_d$; "x" is the mole fraction of tristearin in solution. The equilibrium mole fraction x_s can be calculated from the Hildebrand equation, and it is, therefore, a function of the temperature.

31

Dodecane & Tristearin molar volume L/mol
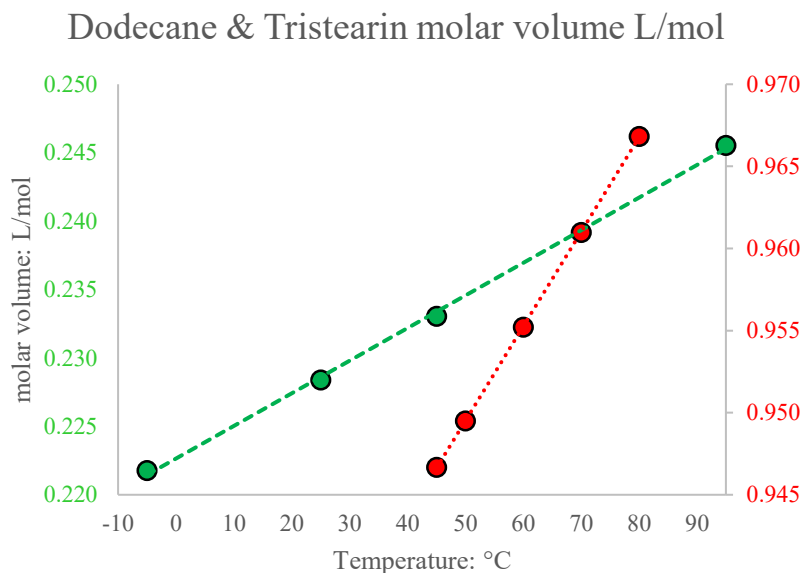
Figure 2.16 A plot of dodecane and tristearin molar volume as a function of temperature. The blue dot (dodecane) and red dot (tristearin) are experimental data; The green line and red line represents the calculated values.

The composition C_∞ of the uncrystallised solution surrounding the crystal, can be computed from its mole fraction x_∞. This concentration is not constant: it will decrease over time, and it is "bound" to a volume in the proximity of the growing crystal. Between each pair of growing crystals there would be a boundary in the liquid where diffusion goes to one crystal or the other as show in Figure 2.17. The composition C_∞ for those crystals in that direction is the composition of the solution at that boundary.
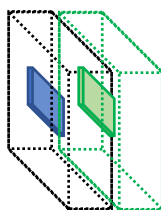
Figure 2.17 Graphic illustration of a pair of growing crystals.

For a dilute solution where the nucleation happens 'instantaneously' and completely evenly distributed, the average interparticle distance can be estimated from the number density of

32

nuclei.

The rate of growth in the direction "*z*" of the diffusion must satisfy the mass transfer expression

$$-D\frac{\partial C}{\partial z}\Big|_{interface} \cdot A_z = \frac{u_z \cdot A_z}{V_m^s} \tag{30}$$

The anisotropic shape of the crystals formed by TAGs is the consequence of different growth velocity for each plane. The area of each growing plane, roughly perpendicular to the velocity and growth direction "*z*", does not depend on the diffusion, which is isotropic in the liquid. The rate of incorporation is controlled by the surface energies of the crystal surfaces. In TAGs nanoplatelets with three main growth surfaces, the differences are enough to produce aspect ratios such as 10:3:1 with respect to the thickness ξ of the nanoplatelet (Acevedo & Marangoni, 2010).

The concentration distribution from Eq. (29) near the interface is shown in Figure 2.15 (a). Chalmers found a mathematical expression for constitutional supercooling (Jackson, 2004). Using the data from (Sekerka, 1965), a plot can be made to illustrate this idea (Figure 2.15 (b)). The solid curves in the figure represent the melting points of the solid (as a function of distance ahead of the interface); the dashed line in the figure represents the actual temperature ahead of the interface. The slope of the melting point curve at the interface can be obtained from Eq. (29). So, constitutional supercooling occurs when the slope of the melting point curve is greater than the slope of the actual temperature field. In other words, constitutional supercooling occurs under the condition where the temperature gradient G is less than the value given by Eq. (32) (Jackson, 2004):

$$G < mC_\infty \left(\frac{1}{k} - 1\right)\frac{v}{D} \tag{31}$$

- where: m is the slope of the concentration distribution at the interface (Figure 2.15 (a) (left figure).

This lag between the solid and dashed curves is the supercooling zone where the actual temperature of the liquid is below its corresponding melting point at the same distance from

the interface. In this region, liquid fats are constitutionally supercooled and crystallize at the interface, forming a cellular or feather-like structure instead of the planar interface (Figure 2.19).
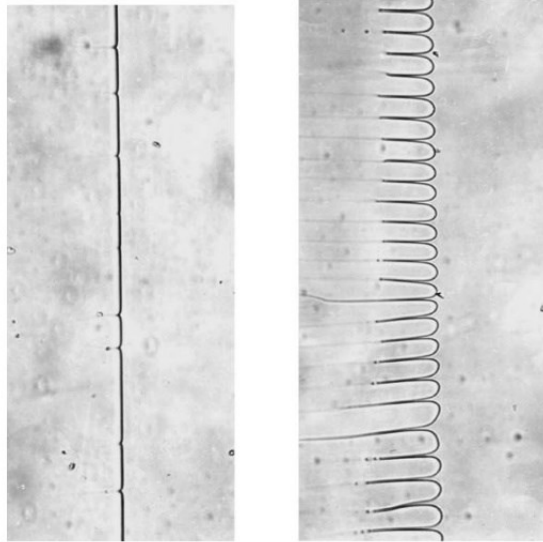
a.
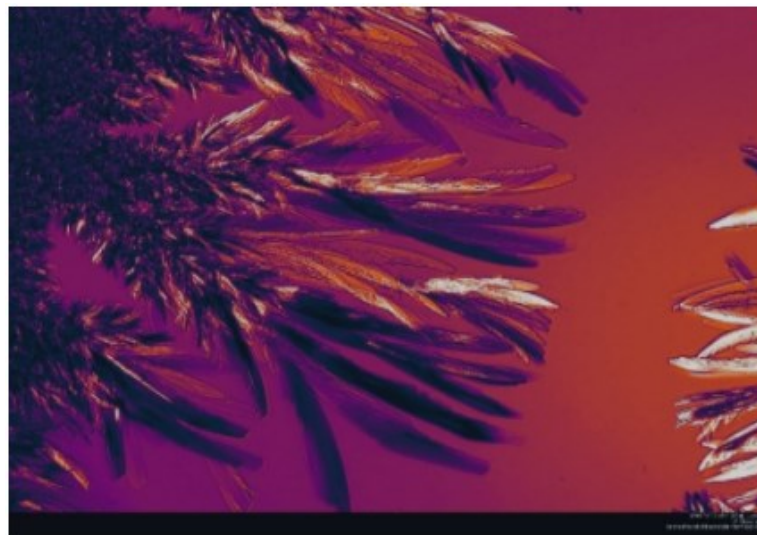
b.

Figure 2.18(a) a planar interface (under approximately isotherm condition) (left figure). A cellular interface (right figure). Adapted from (Jackson, 2004). (b). a feather-like interface (10% tristearin in dodecane solution).

Constitutional supercooling was the forerunner of modern I interfacial-dynamics (Glicksman, 2011; Laudise, Carruthers, & Jackson, 1971). The theory of constitutional supercooling allows us to estimate the kinetics at the interface about the processing conditions (e.g., interface speed, thermal gradient during solidification, and fat composition). However, the model for describing the constitutional supercooling is very complex. This is because the boundary conditions for the diffusion field are applied at a moving interface, and the location and velocity of the interface depend on the diffusion field (Jackson, 2004).

2.2.2 Nucleation

As we discussed above, when the temperature of a single component liquid fat falls below its melting temperature, this liquid fat will be in the supersaturated state, which is also known as the undercooled or supercooled state. The degree supersaturated or undercooled determines the driving forces that govern the fat nucleation rate. However, attaining supersaturated or subcooled state is not sufficient to promote nucleation because a certain energy barrier exists to form nuclei.

When the temperature is a few degrees below the melting point, usually 5 °C–10 °C, the liquid fat exists in a metastable region. The TAG molecules eventually begin to aggregate into tiny clusters called embryos. In a certain volume, the average size and number of embryos continue to increase over time while the single embryo continuously forms and breaks down until reaching the size of stable nuclei. Besides, to overcome the Brownian effects, there is an energy requirement that must be satisfied. This requirement is that the energy of attraction between TAG molecules must be greater than the thermal energy of the molecules in the melt (k_BT). TAG molecules will stay in a "liquid structure" until a critical size of monomers aggregates and then thermodynamically stable solid nuclei are formed (Marangoni & Wesdorp, 2013; Metin & Hartel, 2005; J. F. Toro-Vazquez, Dibildox-Alvarado, Herrera-Coronado, & Charó-Alonso, 2002).

Nucleation is generally classified into two categories, primary nucleation, and secondary nucleation. The primary nucleation may occur either homogeneously or heterogeneously, depending on the existence of foreign nucleating sites. The secondary nucleation may take place with the presence of a solid phase that is previously developed in the system or added

as seed crystals. The secondary nucleation can produce the development of additional solids at a lower supercooling than the one needed for primary nucleation (Hartel, 2001b; Metin & Hartel, 2005). Nucleation is a very strong function of the degree of undercooling. Under a low degree of undercooling, the energy barrier will be higher, causing a nearly zero nucleation rate (Metin & Hartel, 2005).

2.2.2.1 Fisher-Turnbull Model Applied to A Solution

Nucleation plays a key role in determining the properties of crystal networks, such as the number and size, the polymorphic form, and the final distribution in crystalline (Metin & Hartel, 2005). To better study nucleation, nucleation rate (J) is used to describe the number of nuclei formed per unit volume per unit time (William Kloek, Walstra, & van Vliet, 2000; Marangoni & Wesdorp, 2013; R.F.Strickland-Constable, 1968; Turnbull & Fisher, 1949).

When nucleation occurs from a liquid, the value of J depends on two terms: the activation Gibbs energy (ΔG_c) to develop a stable nucleus and the activation Gibbs energy (ΔG_d) for molecular diffusion. ΔG_d is associated with the work involved in the diffusion of molecules from the bulk toward the crystal interface. The relationship among ΔG_c, ΔG_d and J can be described by the Fisher-Turnbull equation (Turnbull & Fisher, 1949):

$$J = \left(\frac{Nk_BT}{h}\right) \exp\left\{-\frac{\Delta G_d}{k_BT}\right\} exp\left\{-\frac{\Delta G_c}{k_BT}\right\} \tag{32}$$

- Where: N is the number of molecules per mole (Avogadro's number 6.022×10^{23}), k_B is the Boltzmann constant (1.3806×10^{-23} J/(K·molecule)), T is the crystallization temperature, in K, and h is Planck's constant ($h= 6.6261 \times 10^{-34}$ J·s) (Herrera et al., 1999).

The Fisher-Turnbull equation has been widely used to describe homogeneous and heterogeneous nucleation (the only difference is surface tension term attributed to different nucleation mechanisms) (Marangoni, 1998). The Fisher-Turnbull analysis is used to compare nucleation in different systems and allows a bettter understanding of energy changes for the onset of nucleation (Herrera, Falabella, Melgarejo, & Añón, 1998; Hjorth, Miller, Woodley, & Kiil, 2015; Metin & Hartel, 2005).

For fat crystal, ΔG_c is related to two terms: the surface Gibbs energy of the crystal-melt interface (γ) and the energy of crystallization liberated (ΔG_m). Therefore, ΔG_c can be expressed as a modified Gibbs-Thomson equation for nanoplatelet (Y. Wang, 2016):

$$\Delta G_c = S_g \cdot \gamma_T{}^3 \left[\frac{V_m{}^3}{\Delta H_m} \left(\frac{T_m}{T_m - T} \right) \right]^2 \quad \therefore \quad S_g = \frac{4 g_s{}^3}{27 g_v{}^2} \tag{33}$$

$$\frac{\Delta G_c}{k_B T} = \frac{-S_g \cdot \gamma_T{}^3}{k_B T} \left[\frac{V_m^s}{\Delta H_m} \left(\frac{T_m}{T_m - T} \right) \right]^2 \quad \therefore \quad S_g = \frac{4 g_s{}^3}{27 g_v{}^2} \tag{34}$$

- Where: γ is interfacial energy, in J/m^2; T, temperature, in K; T_m is the melting temperature, in K; V^s_m is the molar volume, in m^3/mol.

Viscosity is a physical parameter that is inversely proportional to molecular diffusion. When the degree of undercooling increases, viscosity of liquid phase can be a limiting factor for nucleation or crystal growth (Hartel, 2001b). Diffusion of TAG molecules in solution follows Fick's laws: the molar flux due to diffusion is proportional to the concentration gradient; the rate of change of concentration at a point in space is proportional to the second derivative of focus with space (Fick, 1855; Jackson, 2004b).

The Fisher–Turnbull equation is originally derived from a single component system. The driving forces for crystallization depend on a single melting point. Besides, the Fisher–Turnbull equation can only be applied to a low degree of undercooling (*i.e.* <10 ℃). The Fisher-Turnbull analysis is not valid in the case of compound component crystallization and massive crystallization. However, the Fisher–Turnbull equation can also apply to the multi-component systems that have a narrow range of melting temperature (*e.g.* palm and sunflower oils) (Herrera, de León Gatti, & Hartel, 1999; Metin & Hartel, 2005; Widlak, Hartel, & Narine, 2001).

The value of the interfacial energy is very difficult to estimate with certainty. The geometrical model chosen for the hypothetical nucleus has a very big impact on its calculated value. Traditionally, a spherical nucleus has been assumed in the literature. This assumption, however, is clearly not applicable to TAGs. For example, the value of gamma for a nucleus from the FT equation is computed from the value obtained from Foubert (Foubert, Vanrolleghem, & Dewettinck, 2005).

The value of cst2 is obtained from experimental data. Its general definition would be, the value of gamma for a nucleus from the FT equation is computed from the value obtained from

$$cst2 = \frac{-S_g \cdot \gamma_T{}^3}{k_B} \left(\frac{V_m^s}{\Delta H_m}\right)^2 \quad \therefore \quad S_{gp} = \frac{4g_s{}^3}{27g_v{}^2} \quad or \quad S_{gs} = \frac{16\pi}{3} \tag{35}$$

For values of a = 3 and b =10, Sgp is 104.7. For the spherical nucleus assumption Sgs = 16.8.

$$\frac{-S_{gs} \cdot \gamma_{Ts}{}^3}{k_B} \left(\frac{V_m^s}{\Delta H_m}\right)^2 = \frac{-S_{gp} \cdot \gamma_{Tp}{}^3}{k_B} \left(\frac{V_m^s}{\Delta H_m}\right)^2 \tag{36}$$

The properties of the material and Boltzmann constant are the same, thus

$$S_{gs} \cdot \gamma_{Ts}{}^3 = S_{gp} \cdot \gamma_{Tp}{}^3 \tag{37}$$

$$\gamma_{Tp} = \sqrt[3]{\frac{S_{gs}}{S_{gp}}} \cdot \gamma_{Ts} \tag{38}$$

The value of the estimated interfacial energy for the nanoplatelet would be 0.54 times the value estimated from the spherical assumption.

Using the value of cst2, a value of 8.8 KJ/mol can be obtained for ΔG^* (KJ/mol) at 19 ° C for coco butter (Foubert et al., 2005). Similar values (at the same order of magnitudes) were reported in literature: ΔG^*= 8.44 KJ/mol for 80% palm stearin blend in sesame oil at 36 °C; ΔG^*= 7.5 KJ/mol for 30-70% high-melting (HMF) in low-melting (LMF) milk at 35 °C; ΔG^*= 1.89 KJ/mol for MF-TAG with 0.1 wt% DAG Standard (dipalmitin) at 25 °C (Herrera et al., 1999; J. Toro-Vazquez, Herrera-Coronado, Dibildox-Alvarado, Charo-Alonso, & Gomez-Aldapa, 2002; A. J. Wright & Marangoni, 2002)

A more difficult uncertainty is due to the absence of true 'bulk' molecules in nanoplatelets of a small number of layers, as discussed by Unruh & Bunjes (Bunjes & Unruh, 2007) . The melting temperature Tm of nanoplatelets can be as much as 15 C° lower than the bulk material. The molar volume is slightly larger, and the melting enthalpy ΔHm becomes

smaller. Disregarding the small increase in entropy due to the small increase in volume, a decrease of 10 C° in alpha monolayer nanoplatelets would cause a decrease in enthalpy from 107 KJ/mol to 104 KJ/mol. The increase in molar volume would be a factor of about 1.03. The impact of these changes, that are squared in the definition of cst2, is to increase the estimated interfacial energy by a factor of 3.5.

These two uncertainties, i.e., shape factors and non-bulk properties, require that the literature estimates of interfacial energy be taken with reservation.

Deviation from ideal equilibrium

Attractive or repulsive forces between solute and solvent modify the ideal Hildebrand equation presented earlier. An "activity coefficient, γ" is used to improve the estimate:

$$\ln(\gamma \cdot x) = \left(\frac{\Delta H_m}{R}\right)\left(\frac{1}{T_m} - \frac{1}{T}\right) \tag{39}$$

γ is the activity coefficient. There are several methods to estimate the activity coefficient. A common method is to use the Margules equation (Gokcen, 1996; Margules, 1895)

$$\ln(\gamma) = [(A_{12} + 2 \cdot (A_{21} - A_{12}) \cdot x] \cdot [(1-x)^2] \tag{40}$$

In the simpler case that $A_{12}=A_{21}=A$ then:

$$\ln(\gamma_1) = A \cdot (1-x)^2 \tag{41}$$

The coefficients A_i are determined experimentally for each mixture. For some materials, the coefficients can be estimated using predictive models of properties, such as UNIQAC (UNIversal QUAsiChemical, is an activity coefficient model used in description of phase equilibria).

Hildebrand's equilibrium equation for ideal solutes can be thus modified:

$$\ln(\gamma_1 \cdot x_e) = \left(\frac{\Delta H_m}{R}\right)\left(\frac{1}{T_m} - \frac{1}{T}\right) \tag{42}$$

$$\ln(\gamma_1) + \ln(x_e) = \left(\frac{\Delta H_m}{R}\right)\left(\frac{1}{T_m} - \frac{1}{T}\right) \tag{43}$$

$$A \cdot (1 - x_e)^2 + \ln(x_e) = \left(\frac{\Delta H_m}{R}\right)\left(\frac{1}{T_m} - \frac{1}{T}\right) \tag{44}$$

$$\ln(x_e) = \left(\frac{\Delta H_m}{R}\right)\left(\frac{1}{T_m} - \frac{1}{T}\right) - A \cdot (1 - x_e)^2 \tag{45}$$

$$\ln(x_e) = \left(\frac{\Delta H_m}{R \cdot T_m}\right)\left[\left(1 - \frac{T_m}{T}\right) - A' \cdot (1 - x_e)^2\right] \tag{46}$$

$$A' = \frac{A}{\left(\frac{\Delta H_m}{R \cdot T_m}\right)} = \frac{A}{\left(\frac{\Delta S_m}{R}\right)} \tag{47}$$
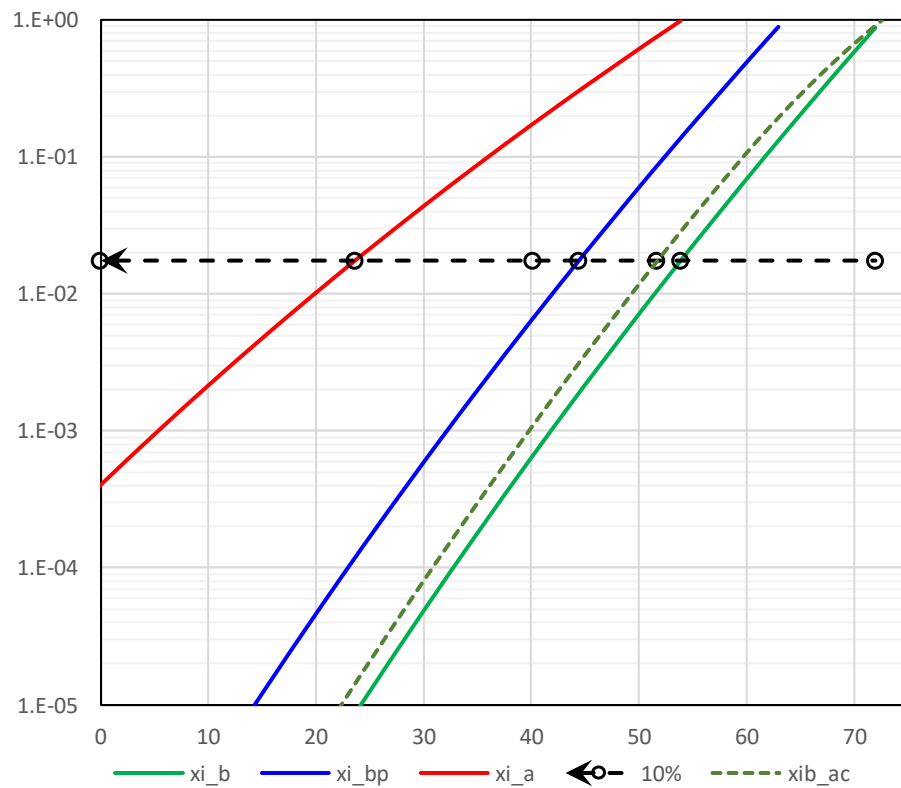
Figure 2.19 Equilibrium mole fraction of tristearin in a non-crystallizing solvent, as a function of temperature in °C. The solid lines correspond to ideal solubility. The dashed line (xib_ac) shows an example of non-ideal behaviour for β. Using $A'_\beta = 0.013$, the dashed line can pass through the intersection of the initial crystallization temperature and concentration of a solution.

As shown in Figure 2.21, **A'** is convenient because it is a non-dimensional ratio between the factor of a solute and the melting entropy of that solute divided by R, the universal gas constant. Hence, values of **A'** are easier to generalize between different solutes of analogous series.

2.2.3 Growth

Once nuclei formed, the following step is the enlargement of these nuclei, also known as "crystal growth". TAG molecules from a liquid may be incorporated into an existing crystal lattice (Nawar, 1996). In fact, nucleation and crystal growth are not mutually exclusive: nucleation crystals growth may take place at the same time. The separation of these two kinetics for each process is difficult (Boistelle, 1988).

Crystal growth depends on the probability that a TAG molecule is in the right configuration and binds into the correct site on a crystal surface. TAG molecules will return to the supersaturated system with wrong configurations or binding sites. Rearrangement of individual molecules or clusters (growth units) can take place at crystal surfaces to obtain the right configurations. And there are energy barriers of transitions between different configurations for TAG molecules. A slow growth of crystals may be due to the result of a high energy barrier in transition from multiple configurations to the correct configuration.

Moreover, the presence of multiple configurations in liquid has a competitive effect in binding into the corrects site on a crystal surface (Chang, 2000; Derdour, Pack, Skliar, Lai, & Kiang, 2011; Kessler et al., 1981; Kubota, 2001; Yu, Reutzel-Edens, & Mitchell, 2000). TAG molecules that are not in the right configurations may act as ''impurities'', which depresses the melting/dissolution temperatures and block surface integration sites (William Kloek, 1998).

Right after a TAG molecule is incorporated into the crystal lattice, a number of latent heat will be released, which may impede further crystal growth. Crystal growth will cease once the system is in phase equilibrium or fully crystallized (Marangoni & Wesdorp, 2013; Metin & Hartel, 2005). Crystal may be formed in meta-stable α phase and is followed by recrystallization and formation of more stable crystals (Hjorth et al., 2015; Mazzanti, Marangoni, & Idziak, 2008).

Fitting the Avrami model to DSC data

The Avrami model is perhaps the semi-empirical model applied most often to describe the kinetics of isothermal crystallization of TAGs (Dibildox-Alvarado & Toro-Vazquez, 1997; Kawamura, 1979; Metin & Hartel, 1998; J. Toro-Vazquez, Briceño-Montelongo, Dibildox-

Alvarado, Charó-Alonso, & Reyes-Hernández, 2000; Vanhoutte, Foubert, Duplacie, Huyghebaert, & Dewettinck, 2002; A. Wright, Hartel, Narine, & Marangoni, 2000). The Avrami model (Avrami, 1939, 1940, 1941) is a general approach to quantify the isothermal crystallization kinetics including nucleation, crystal growth, and impingement (Garti & Sato, 2001). In the 1940s, various authors independently developed this kinetic formulation, which is sometimes called the Johnson–Mehl–Avrami–Erofeev–Kolmogorov equation (A. Wright et al., 2000). The theory was initially developed for low molecular weight materials such as metals. Later it was extended to the crystallization of high polymers (Kawamura, 1979).

The Avrami model is used to analyze data that combine nucleation and crystal growth, allowing further understanding of the complex mechanism of a crystallization process. The Avrami model shows the relationship of the mass/volume change of the crystal and time (Figure 2.19) (Marangoni & Wesdorp, 2013):

$$\frac{SFC}{SFC_{Max}} = 1 - \exp[-(k \cdot t)^n] \tag{48}$$

- Where: SFC corresponds to the solid fat content at a particular time; SFC_{Max} corresponds to the maximum SFC achieved at a particular temperature; k is a crystallization rate constant that depends primarily on crystallization temperature; and n, the Avrami exponent, is a dimensionless constant that is determined by the dimensionality of the growth (Linear, planar, or spherical) and the type of nucleation (Instantaneous or sporadic).
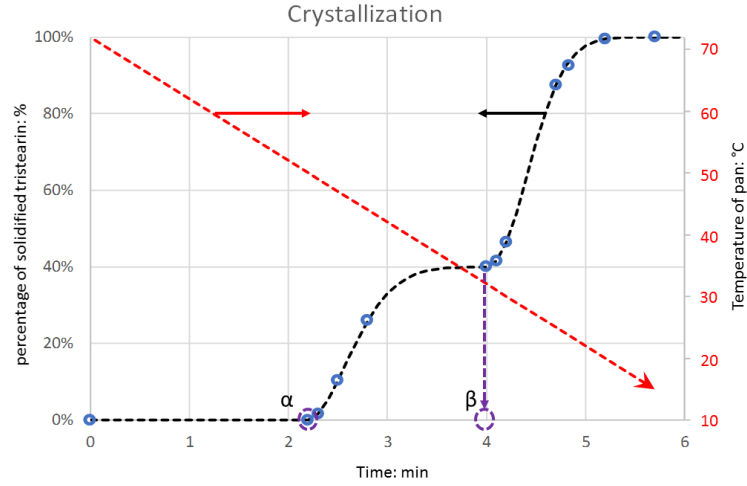
Figure 2.20 The primary y-axis (black) is percentage of solidified tristearin, as a function of time in minutes (x-axis), as described by the Avrami model. The secondary axis (red) shows the temperature of the sample pan, as function of the same time. The first purple circle indicates the initial time, $t_{0\alpha}$, for the α form crystallization. The second circle marks the onset time, $t_{0\beta}$, for the β form.

In practical cases where there are, for example, two crystallization steps, each step can be described by its own set of parameters: maximum, onset time, rate constant and characteristic index.

$$\frac{m_\alpha}{m_{\alpha_{Max}}} = 1 - \exp\{-(k_\alpha \cdot (t - t_{o\alpha}))^{n_\alpha}\} \qquad (49)$$

$$\frac{m_{\beta\prime}}{m_{\beta\prime_{Max}}} = 1 - \exp\{-(k_{\beta\prime} \cdot (t - t_{o\beta\prime}))^{n_{\beta\prime}}\} \qquad (50)$$

In fat crystallization, k depends on the crystallization temperature (Kawamura, 1979). Therefore, when the model is used for constant cooling rates, where the temperature is changed linearly with time, its application is very questionable. Although this application is far from being theoretically correct, it provides occasionally a semi-empirical method to summarize or smooth data.

The theoretical Avrami exponent, n, includes the time dependence of nucleation type (*i.e.,* instantaneously (0) or sporadic (1)) and the growth morphology of the crystallizing particles (*i.e.,* dimensions of crystal growth from 1 to 3). However, the meaning of the n value is not straightforward, since an n value of 2 and 3 can have more than one meaning (*e.g.,* n = 2 may correspond to a linear growth along with a sporadic nucleation, or a plate-

43

like growth following an instantaneous nucleation). Theoretically, only integer values should be obtained for **n** (*i.e.,* 1 to 4). However, fractional values of "*n*" often fit better to the data. The Avrami model needs to be modified to appropriately accommodate crystallization-specific TAG systems (Foubert, Dewettinck, & Vanrolleghem, 2003; Foubert, Vanrolleghem, Vanhoutte, & Dewettinck, 2002).

As shown in Figure 2.20 (a) and (b), the Avrami model and DSC experimental data are plotted together as a function of time. The onset times, t_0, for the α and β forms, have been used from the DSC experiment data in the Avrami model. However, the formation of the **α** crystals is faster than Avrami model, reaching a lower percentage of solidified tristearin. The formation of **β** crystals is also faster than the model value.

(a)
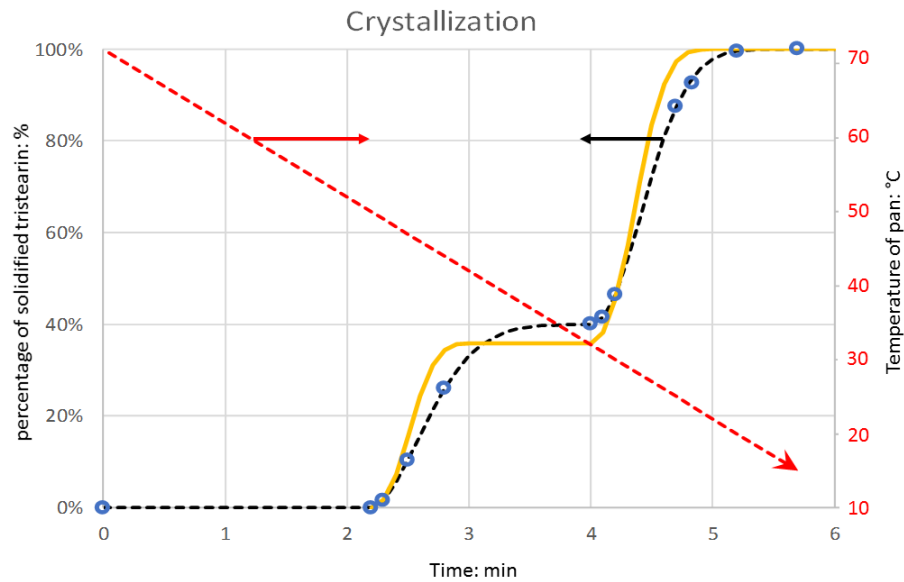
Avrami model Vs DSC data
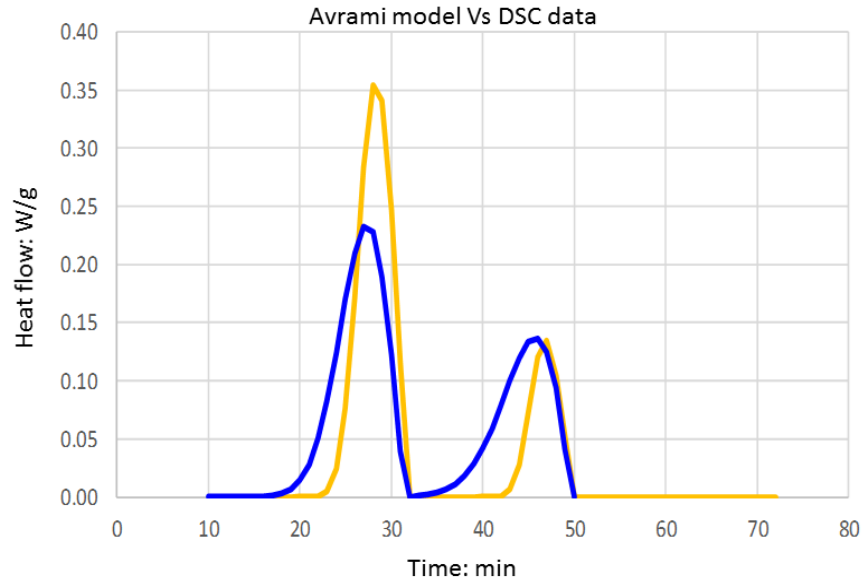
(b)

Figure 2.21 (a) The primary y-axis (black) is percentage of solidified tristearin as a function of time (in min, x-axis), as described by the Avrami model. The secondary axis (red) is the temperature of the sample pan as function of the same time. The orange line is from DSC data. (b) A DSC thermogram showing the heat flow (W/g) versus time (minutes) as described by the DSC data (orange line) and by the Avrami model (blue line).

Other models

The Gompertz model as developed by Zwietering, Jongenburger, Rombouts, Vantriet to describe the growth of bacteria (Zwietering, Jongenburger, Rombouts, & Vantriet, 1990). Kloek et al. (2000) and Vanhoutte (2002) used the Gompertz model to describe the kinetics of fat crystallization (William Kloek, Walstra, & Vliet, 2000; Vanhoutte, Dewettinck, Foubert, Vanlerberghe, & Huyghebaert, 2002). A benefit of the Gompertz model is that its parameters have a very straightforward physical interpretation. However, there are limitations of the Gompertz model in the application in the field of fat crystallization. The theoretical basis for using the Gompertz model in fat crystallization is rather weak. Bacterial growth can intuitively be compared with fat crystallization, but this provides no real theoretical justification (Foubert et al., 2003; Foubert et al., 2002).

45

The Foubert, Vanrolleghem, Vanhoutte, et al. model was developed by Foubert research team (Foubert et al., 2002). This model represents the crystallization process as if it is a combination of a first-order forward reaction and a reverse reaction of order n. This model is often easier to interpret the equation mechanistically. It only needs minor changes to the equation based on acquired knowledge. This model has an advertence over other models that it can be used to describe non-isothermal crystallization kinetics, by incorporation of secondary models describing the temperature dependence of the parameters. Besides, the Foubert model can fit asymmetric cases well, which may bring a better quantitative description of crystallization processes. On the other hand, the Foubert model is weak in theoretical basis. It is still not clear whether a true physical mechanism lays beneath this goodness of fit (Foubert et al., 2003).

2.2.4 Melting/Dissolution

Melting and dissolution of fats are important in food production. These two terms are similar. Both of them involve in the disappearance of solid fats. When a solid fat is incorporated into a solution, partial melting can take place when the ambient temperature increases and then become higher than the boundary temperature. When fat crystals are in contact with a solution, dissolution may take place at the same time. Melting and dissolution are not exclusive, they are closely related and even take place even at the same time. These two terms are both influenced by heat transfer, mass transfer, and interface kinetics *etc.* (Berk, 2009).

In thermal kinetics, melting of solid fats refers to the phenomenon of a solid-to-liquid phase transformation via increasing temperature above the solidus (*i.e.,* the maximum temperature at which a given substance is completely solid). When a solid fat melts, latent heat has to be removed and then mass transfer or diffusion follows. During this process, fat molecules need to be transported to the interface and rearranged at the interface, which is the controlling step of melting (Foubert et al., 2003).

Dissolution is a transport phenomenon, which is similar to crystallization but in the opposite direction. The dissolution of solids into a liquid or other solvent is a process,

where the passage of a soluble substance from a solid matrix to a liquid solution (Berk, 2009). Noyes & Whitney (1897) define dissolution in food production as the dispersion of an insoluble substance in a liquid (*e.g.,* dispersion of cocoa powder or milk powder in water) (Berk, 2009; Noyes & Whitney, 1897).

Dissolution kinetics has been studied extensively for over 100 years. The first step of dissolution of a solid in solvent is to wet the solid surface, which allows the solvent to penetrate the solid. The second step is the release and the migration of solute molecules from the wetted surfaces into the solvent via diffusion and convection. The rate limiting step is the migration of the solute away from the solid, which can be described by a diffusion controlled model. This model is based on assumption that the solid particles are uniform, compact and spherical; solid particles are suspended in a very large volume of liquid. Therefore, the concentration of the bulk liquid does not change noticeably as a result of the dissolution.

Wang & Flanagan (1999) developed a cubic root model allows to estimate the time necessary for the total dissolution of a particle of pure solute. The necessary time is proportional to the cubic root of the mass of that particle. The cubic root model assumes the size of particles are in a certain range (not too small). The cubic root model is simple ,intuitive, and quite accurate in studying dissolution kinetics (Berk, 2009; J. Wang & Flanagan, 1999).

2.2.5   Cooling Rates and Temperature Control

The thermal history of fats plays a key role in determining the size and the shape of fat crystals (Roos & Roos, 1995). when fat is cooled rapidly, it tends to form a harder network that is filled of small crystals along with more numerous interactions between these tiny crystal particles. A fast cooling rate indicates a higher driving force, which means nucleation and crystal growth events are forced to take place in a short timescale (*i.e.,* a higher nucleation rate). Under rapid cooling, crystallization kinetics are faster, which results in numerous crystallites with a higher surface free energy in a less stable polymorph. Consequently, fat crystals have a more homogeneous spatial distribution. A rapid cooling

will result in an increase in viscosity, which can limit molecular diffusion and crystal growth. Thus, a fast cooling rate yield a firmer fat (Figure2.22 (a) and (c)).
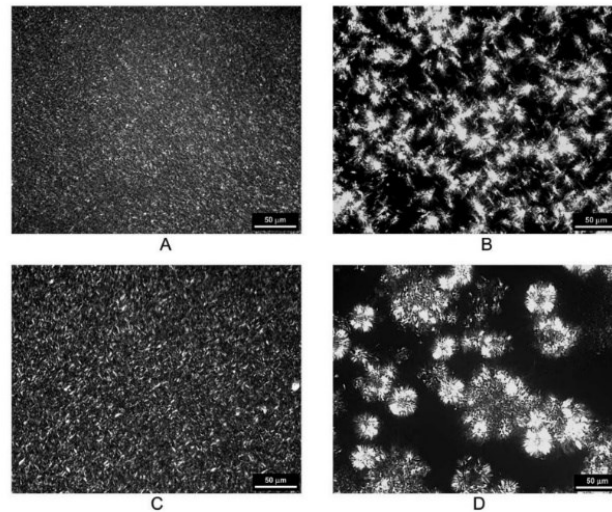
Figure 2.22 Polarized light micrographs of Anhydrous milk fat (AMF) cooled rapidly (A) and slowly (B), and lard cooled rapidly (C) and slowly (D). Adapted from (R. Campos et al., 2002).

On the other hand, when fat is cooled down slowly, it tends to form a softer network that is filled of large particles along with the weaker attractive forces. A slow cooling indicates a low driving force, which means a longer induction time (a lower nucleation rate). Under a slow cooling rate, fat crystals tend to form in more stable conformations with a lower surface free energy of the solid state (J. F. Toro-Vazquez, Diblidox-Alvarado, Herrera-Coronado, & Charo-Alonso, 2001). A slow cooling rate allows a longer time for TAGs with similar chain lengths to associate with each other, co-crystallize, and fractionate (Marangoni, 2013). As shown in Figure 2.22 (b) and (d), under a slow cooling rate, AMF and lard can form a crystal network composed of larger crystalline particles with a lower crystal volume fraction over a longer period. These larger particles are in stable polymorphic forms with heterogeneous spatial distributions of mass. In summary, different cooling rates can affect the properties of fat crystal network (R. Campos et al., 2002).

2.2.5.1 Difference Between Controlled Temperature and Temperature at The Sample

When fats are cooled down in a shear cell, there is a difference between temperature controlled and temperature at the sample. Ideally, the temperature profile obtained directly

48

via the instrument should match the actual sample temperature. In practice, there is a deviation from the ideal and real temperature profile due to several reasons. Most rheometer cells do not measure the temperature of the sample directly, but rather control the temperature near the interfaces of the sample. At high shear rates, the temperature of the material can differ significantly from the value commanded to the instrument, even in small gap instruments.

Even though the instrument can measure the temperature correctly, at high shear rates, there is a large temperature gradient across the sample with a significant departure from the radial shear rate. Under high shear rates, the temperature commanded to the sample holder of a rheometer does not match the actual temperature of the sample being tested. The heat produced by the intermolecular friction (*i.e.,* viscous heat) under high shear rate is non-avoidable. Under shear flow, the formation of a suspension will increase viscosity associated with a consequently increasing viscous heat generation. The increasing viscous heat generation can limit the amount of solids that can be crystallized (Fan, Michel, & Gianfranco, 2009; Mudge & Mazzanti, 2009).

2.2.6   Shear Flow

2.2.6.1   General Concepts of Shear Flow

In a shear flow, adjacent layers of fluid are displaced in a direction parallel to each other with different speeds (Smits, 2006). Couette flow is a simple example of shear flow. In fluid dynamics, Couette flow refers to the laminar flow (*i.e.,* fluid flows in parallel layers with no disruption between the layers) of a viscous fluid between two parallel plates where one plate is moving relative to the other (Falkovich & Falkovich, 2011).
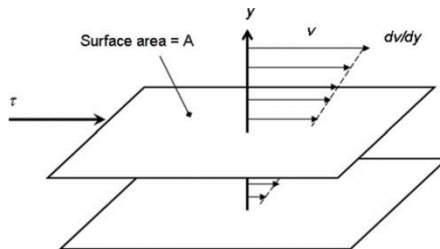
Figure 2.23 The concept of the definition of viscosity. Adapted from (Ortega-Rivas, 2012).

Shear Rate () refers to the velocity gradient established in a fluid, as a result of an applied shear stress (Figure 2.24) (Ortega-Rivas, 2012):

$$\dot{\gamma} = \frac{dv}{dy} \tag{51}$$

- Where: is shear rate, measured in the reciprocal seconds, s^{-1}; v is fluid velocity, m/s; y is a distance in y-axis, m.

2.2.6.2 Shear Rate in Circular Cell

As shown in Figure 2.25, Couette shear cells consist of two rotating coaxial concentric cylinders (R_1 and R_2). Sample is loaded in the middle gap (blue part). The inner cylinder (R_1) then rotates to generate shear. Then Rotation Couette flow is characterized geometrically by two parameters: μ ($\mu = \Omega_2/\Omega_1$, Ω is the angular velocity correspondingly) and η (annulus ratio) ($\eta = R_1/R_2$, R is the cylinder radius correspondingly) (Munson, 2013).
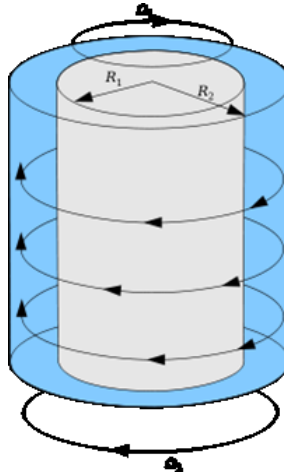
Figure 2.24 The concept of Taylor-Couette flow in literature (Munson, 2013).

Assuming no slip at the shaft or wall, a profile of shear rates is present only due to the curvature of the cell(Fan et al., 2009). The local viscosity is the proportionality factor between shear stress σ, and shear rate.

$$\sigma = \eta \, \dot{\gamma} \tag{52}$$

Its relationship to the measured torque and angular velocity, are given, for an effective shaft-fluid contact area A_s, by:

$$\sigma = \eta \, \dot{\gamma} \tag{53}$$

50

$$\sigma = \frac{\tau}{r_i A_s} \tag{54}$$

$$\dot{\gamma} = r \left(\frac{\partial \dot{\omega}}{\partial r}\right) = \frac{\partial u_\theta}{\partial r} - \frac{u_\theta}{r} \tag{55}$$

- Where: σ is shear stress, Pa; η is viscosity of the oil, Pa·s; is local shear rate, s^{-1}; τ torque at the shaft N·m, ω is the angular velocity, rad/s; r_i is the radius of the inner rotating cylinder, m; A_s is the effective contact area of the fluid on the shaft, m^2; and u_θ is the local tangential velocity, m/s.

The velocity distribution is independent of the magnitude of the Newtonian viscosity, when the material is considered isothermal. Thus, the non-dimensional ratio of the local velocity, u_θ, over the velocity at the shaft, $u_{\theta s}$, can be expressed solely as function of the non-dimensional radial position "x" and characteristic geometric ratio "κ" (Kappa).

$$u_x = \frac{u_\theta}{u_{\theta s}} = \frac{u_\theta}{\dot{\omega} \cdot r_i} = \frac{\kappa(x^2 - 1)}{x(\kappa^2 - 1)} \tag{56}$$

- Where: x is the non-dimensional radial position r/r_o; and κ is the characteristic geometric ratio r_i/r_o., with r_o as the radius of the outer static cylinder.

The corresponding profile for shear rate is:

$$\dot{\gamma}_x = \frac{u_{\theta s}}{r_o} \frac{\kappa}{(\kappa^2 - 1)} \frac{2}{x^2} \tag{57}$$

The volume-weighted average shear rate is (Fan et al., 2009):

$$\dot{\gamma}_{av} = \frac{-4\kappa^2 \ln(\kappa)}{(1 - \kappa^2)^2} \dot{\omega} \tag{58}$$

When: $\dot{\gamma}_{av}$ tends to 1, this volume-weighted average shear rate tends to the "large radius-small gap" (lrsg) approximation:

$$\dot{\gamma}_{lrsg} = \frac{\dot{\omega} r_i}{r_0 - r_i} = \frac{\kappa}{1 - \kappa} \dot{\omega} \tag{59}$$

The debate on whether shear enhances crystallization (by a shear-induced ordering) or shear suppresses crystallization is largely due to the different conditions of studies . Blaak

51

et al., (2004) explained that shear may suppress the birth of crystals by removing the substance from small crystals while shear may enhance a shear-induced ordering in the fluid which facilitates nucleation process (Blaak, Auer, Frenkel, & Löwen, 2004). However, according to Acevedo & Marangoni (2010), fats tend to crystallize in platelet shape rather than hard-sphere crystal, which means fat crystals have different behaviors in a Couette flow (Acevedo & Marangoni, 2010).

2.2.6.3   Viscous Heat Generation

Viscous heating refers to the irreversible transformation of work into heat by adjacent layers of a fluid moving at different velocity, due to shear forces. A measurable non-isothermal temperature profile can thus arise, when the rate of heat generated exceeds the rate of heat removed from the material. This non-uniform temperature field influences the kinetics of the flow, since viscosity is a function of temperature.

The thermo-mechanical coupling produces significant deviations from the isothermal velocity profiles. Viscous heating can cause significant viscometric errors, especially at high shear rates, in rotational viscometers (Papathanasiou, 1998). The viscosity of most liquids is exponentially dependent on temperature. Thus, small changes of temperature in the liquid can lead to significant errors in measurement. In the case where solutes are crystallized under shear flow, viscous heat can melt smaller less stable crystals while preserving larger crystals (G. Mazzanti et al., 2011).

The local rate of heat generation per unit volume (W/m^3), at a location "r" is

$$\dot{q}_V = \eta_r \cdot (\dot{\gamma}_r)^2 \tag{60}$$

This heat needs to be dissipated by transport from high to low temperature zones in the fluid. Hence, the fluid is colder near the cooling surfaces of the vessel where the crystallization is being conducted. The regions further from the surfaces have higher temperatures. For materials where the viscosity makes this problem relevant, convection is often not enhanced by mixing, since only laminar flow is present. Therefore, the fluid can experience considerable temperature gradients. Both the viscosity of the continuous liquid and the volume fraction of crystals change with temperature.

2.2.6.4 Rheology of Suspensions

The rheological properties of suspensions have been studied since the beginning of the twentieth century. The first research was done by Einstein, A. (1906,1911) in his classical study of the viscosity of the dilute suspension of rigid spheres (Einstein, 1906, 1911). When the nearest-neighbor interactions between particles in suspension are not negligible, Einstein's expression is corrected following Thus, Guth & Simha (1936). They established an equation for the first-order effect of spheres interacting with one another (Guth & Simha, 1936):

$$\frac{\mu}{\mu_0} = 1 + 2.5\varphi + 12.6\varphi^2 \tag{61}$$

- Where: μ is the viscosity of the suspension; μ_0 is the viscosity of the pure solvent; φ is the volume fraction of the spheres in the suspension. (Guth & Simha, 1936).

The $\boldsymbol{\beta}$ crystals of tristearin have a density of 1030 kg/m^3 (Van Langevelde et al., 1999), whereas the mass density of liquid dodecane is around 750 kg/m^3 (Ferguson & Lutton, 1941) depending on the temperature. Crystallization of the 10% w/w tristearin solution of this thesis yields a volume fraction "φ" around 0.018. The ratio of viscosities $\boldsymbol{\mu/\mu_o}$ would then be 1.027. This small variation, less than 3%, would be measurable by a rheometer. The values of dodecane viscosity calculated by the Einstein & Guth model are slightly higher than the Andrade viscosity equation and reference data, as shown in Figure 2.26.
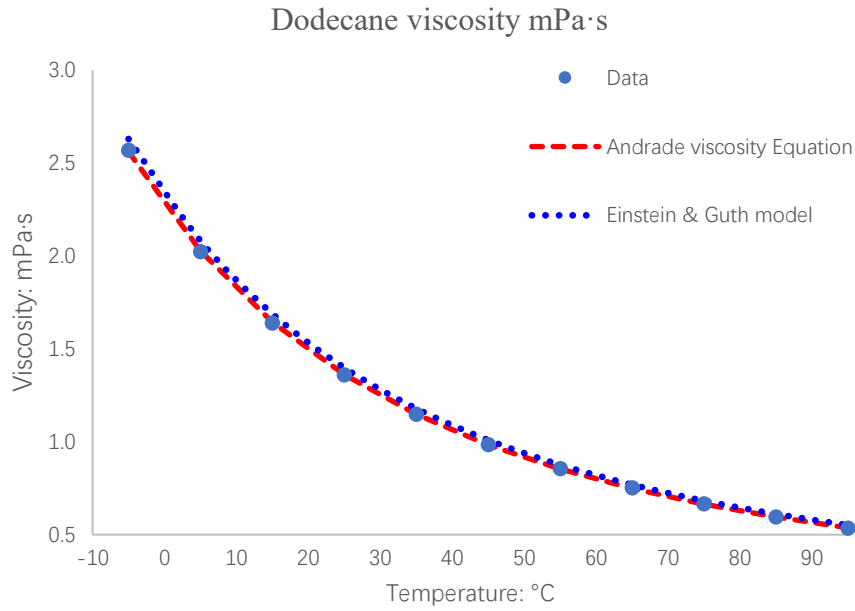
Figure 2.25 Viscosity of dodecane as a function of temperature. The blue dot represents the viscosity data from references. The red dash line represents the calculated value based on Andrade viscosity equation; The blue dot line represents the calculated value based on Einstein & Guth model (Ambrose & Tsonopoulos, 1995; Caudwell et al., 2004; Guth & Simha, 1936; Rosenthal & Teja, 1989).

There are many models that attempt to describe the viscosity of concentrated suspensions of rigid spherical particles. Mooney (1951) developed an equation for a suspension of finite concentration (Mooney, 1951):

$$\ln\left(\frac{\eta}{\eta_s}\right) = [\eta]\frac{\varphi}{\left(1 - \frac{\varphi}{p}\right)} \tag{62}$$

- Where: η is the apparent viscosity of the suspension; η_s is the apparent viscosity of the continuous phase (or liquid phase); $[\eta]$ is the intrinsic viscosity of the particles; φ is the volume fraction; p is called the packing fraction since the approach to infinite viscosity is usually ascribed to the attainment of the close-packed structure.

The intrinsic viscosity $[\eta]$ is a measure of the solid's contribution to the viscosity η of a suspension. It is defined as:

$$[\eta] = \lim_{\varphi \to 0} \frac{\frac{\eta}{\eta_s} - 1}{\varphi} \tag{63}$$

- Where: η is the viscosity of the suspension; η_s is the viscosity in the absence of the

54

particles; φ is the volume fraction of solids in the suspension.

The intrinsic viscosity of hard spheres [η] is 5/2, regardless of size. However, according to Larson (1999), big particles in suspension have large intrinsic viscosity values. The values, however, depend on the shape of the particles (Larson, 1999).

Based on Mooney's model, Krieger and Dougherty (1959) extend the equation to:

$$\frac{\eta}{\eta_s} = \left(1 - \frac{\varphi}{\varphi_M}\right)^{-[\eta]\varphi_M} \tag{64}$$

- Where: φ_M is the maximum volume fraction of solids, which depends on particle-size distribution and shape.

For mono-disperse spherical particles, the maximum practical volume fraction typically falls between 0.6 and 0.7 (Larson, 1999), since the maximum packing is 0.745. In the case of nanoplatelets the value would be practically 1, if the platelets were perfectly aligned. For random distribution the value is lower, but depends on the spatial ordering of the particles. For instance, if the observed change in viscosity was 10 % ($\eta/\eta_s = 1.1$), for a volume fraction φ of 0.018 (tristearin crystallized from dodecane), and a maximum fraction φ_M of 0.9 (nanoplatelets), then the intrinsic viscosity would be [η] = 5.23 (non-dimensional).

The Krieger-Dougherty equation is a successful model, which can be used in many complex systems. It can fit data from an entire range of volume fractions (between η_0 to η_∞) of latex spheres. It also works for ground particles, glass rods and fibers (Barnes, 1989; de Kruif, van Iersel, Vrij, & Russel, 1985; Papir & Krieger, 1970; Woods & Krieger, 1970).

These models, unfortunately, provide estimates that are not shear rate dependent, *i.e.* they are limited to describe the viscosity of a Newtonian fluid.

However, dispersions and suspensions of solids in liquids normally have non-Newtonian characteristics, *i.e.* their viscosity depends on shear rate and/or the deformation history (Ortega-Rivas, 2012). This is even more pronounced if the particles are anisotropic, such as the TAG nanoplatelets and their aggregates. The non-Newtonian behavior is the result of the perturbation of the Brownian motion of the suspended particles by the shear stress and by the collisions between particles.

Apparent Viscosity

Apparent viscosity (η_{app}) is defined as the ratio between the shear stress applied to a fluid and the shear rate:

$$\eta_{app} = \frac{\sigma}{\dot\gamma} = \frac{K_\sigma \cdot \tau}{\dot\gamma} \qquad (65)$$

- Where: σ is the shear stress, Pa; is the shear rate, s^{-1}; K_σ is the conversion factor for the rheometric device, Pa/(N·m); and τ is the torque value, N·m.

A common model that describes many shear dependent complex fluids is the power law relationship, simplified from Herschel-Buckley's equation when the yield stress is zero:

$$\sigma = k \cdot (\dot\gamma)^n \rightarrow \eta_{app} = k \cdot (\dot\gamma)^{n-1} \qquad (66)$$

The exponent "**n**" is known as the behaviour index, and the constant "**k**" is known as the consistency index. The value of **n** for shear thinning (thixotropic) materials is less than one, and for shear thickening (dilatant) fluids it is larger than one. It is seldom possible to calculate the behaviour index quantitatively from the characteristics of the particles of the fluid. The power law expression does not account for time dependent behaviours, or for viscoelastic characteristics of the complex fluid.

Complex Viscosity

The rheological properties of a solution of tristearin in dodecane change, as the tristearin crystallizes out of solution forming suspended nanoplatelets. During cooling, statically or under shear, the solid particles form and organize themselves in the remaining solution. The suspension of nanocrystals can even form a crystalline network. In both cases, simple suspension or network, the complex liquid-solid material will likely have an elastic modulus. This makes the material viscoelastic.

When a complex fluid, such as a paste or a semisolid cream, has a viscoelastic structure, one possible way of summarizing its "fluidity" is by computation of the complex viscosity. The complex viscosity is computed from data obtained using small amplitude oscillatory rheological experiments. The limit of the small deformation is the magnitude of perturbation that does not disrupt the structure. It is meant to only "jiggle" it, as if it was a

three-dimensional array of springs immersed in a viscous liquid. The massless dashpot and spring model is often used to represent these materials.

The complex viscosity ($|\eta^*|$)) is computed as the ratio between the complex modulus and the angular frequency. Its magnitude is:

$$|\eta^*| = \left(\eta'^2 + \eta''^2\right)^{1/2} \qquad (67)$$

- Where: η' is the viscous portion of complex viscosity, $\eta' = \frac{G''}{\omega}$ (G'' is the viscous modulus); η'' is the elastic portion of complex viscosity, $\eta'' = \frac{G'}{\omega}$ (G' is the elastic modulus)

Even materials with very low solid contents, such as the 10 % crystallized tristearin in dodecane (0.018 volume fraction), can form a network of solids strong enough to produce a viscoelastic semisolid. This crystalline network is present in fats (Acevedo & Marangoni, 2010). Its mechanical characteristics are heavily dependent on the process of formation, and not only on the % solids (Marangoni & Narine, 2002a)

2.2.7 Nucleation and growth from a solution under shear

Shearing fluids is an important manufacturing operation in industry, which improves mass and heat transfer, and facilitates product homogeneity. Judicious application of shear can also enhance process optimization. Shear flow is used to develop novel products, *e.g.* tempering of chocolate to induce desired crystal polymorphs of cocoa butter for improving bloom resistance. Shear can also help to alter organoleptic properties of lipid shortenings, and improve the consistency and spreadability of butter and margarine (Rodrigo Campos & Marangoni, 2014; Mazzanti, 2005; S. S. Narine & Humphrey, 2004; Stapley, Tewkesbury, & Fryer, 1999). Even a new phase (phase X) of cocoa butter was found by Mazzanti et al. (2004) when crystallizing it under shear flow. This new phase was not observed under static conditions previously (Mazzanti, Guthrie, Marangoni, & Idziak, 2007).

Shear can accelerate the speed of nucleation and can induce the orientation of crystalline nanoplatelets. Under shear flow, fats tend to form smaller crystals, which form stronger fat crystal networks. Also, shear can reduce phase transition time and alter the phase composition of the final product (Mazzanti, Guthrie, Sirota, Marangoni, & Idziak, 2003;

Tran & Rousseau, 2016). Dhonsi and Stapley (2006) and Mazzanti *et al.* (2007) found that the induction time for the transition of cocoa butter to the stable polymorph depends on shear rates. Cocoa butter crystallized under high shear rate had higher melting point than its low shear counterparts, due to the formation of higher melting fractions (Dhonsi & Stapley, 2006; Mazzanti et al., 2007)

Shear has a significant influence on nucleation in food processing. Shear can increase the rate of primary nucleation by providing enough energy to overcome activation energy barriers for nucleation (Hartel, 2001a). Shear can also enhance secondary nucleation by fracturing newly formed crystals and distributing them throughout the melt, which provides more seeds/interfaces for nucleation and crystal growth (Wiliam Kloek, Van Vliet, & Walstra, 2005; Maleky & Marangoni, 2008). When shear enhances nucleation, the material has a larger number of smaller crystals. These smaller crystals can translate into fat crystal networks with higher mechanical strength. Under shear flow, fats tend to have higher initial SFC values, but over time, SFC will reach equilibrium values similar to statically-crystallized fats (Kaufmann, Graef, Dewettinck, & Wiking, 2012; Kaufmann, Kirkensgaard, Andersen, & Wiking, 2013; Maleky & Marangoni, 2008; Marangoni & Narine, 2002b; Suresh S. Narine & Marangoni, 1999).

Shear fosters crystallite collisions, which may facilitate polymorphic transitions to more stable polymorphs via secondary nucleation (Dhonsi & Stapley, 2006; S. Sonwai & M. R. Mackley, 2006).

Shear may result in viscous heat generation that can produce enough heat to melt smaller, less-stable crystals, while larger crystals remain in suspension. With enough energy provide by shear, most of the crystal mass of lower polymorphs disappears, and nuclei left behind can act as templates for growth of higher polymorphs. At a high shear rate, solid fat content (SFC) is lower due to the viscous heat generation produced by the shear energy (G. Mazzanti, M. Li, A. G. Marangoni, & S. H. J. Idziak, 2011; Mazzanti et al., 2005; Mazzanti et al., 2008). Mazzanti (2005) studied the shear effect on the crystallization of palm oil in a Couette cell with synchrotron x-yay diffraction. He found that shear can induce the acceleration of the phase transition from α to β'. Besides, an increase in shear rates can promote the crystallization of the higher melting fraction and affect the composition of the

crystallites (Mazzanti et al., 2005).

At the nanoscale level, shear may affect crystal nanoplate (CNP) size. According to Maleky et al. (2011), shear can influence the nanostructure of CNPs. At a high shear rate, CNPs are observed to have smaller lengths and widths, associated with a narrower size distribution (Maleky, Acevedo, & Marangoni, 2012; Maleky, Smith, & Marangoni, 2011). However, a reduction in CNP size does not necessarily result in the reduction of meso crystals and vice versa (Acevedo & Marangoni, 2014).

The influence of shear on nucleation depends on shear rate. Below the critical shear rate, shear can increase the frequency of collisions and contact time between crystallites, which results in larger crystals (Tarabukina, Jego, Haudin, Navard, & Peuvrel-Disdier, 2009). Above the critical rate, the average size of crystals can be reduced either through the breakage of larger crystals or inhibition of growth and aggregation of clusters (Wiliam Kloek et al., 2005; Maleky et al., 2011).

The acceleration of polymorphic transitions due to shear can be also explained by another hypothesis: that shear influences the structure of nanoplatelets formed upon nucleation. Then these nanoplatelets can act as templates for higher, more organized polymorphs (Maleky et al., 2011).

Shear effects on x-ray diffraction data

Shear flow can influence x-ray diffraction patterns of fats, such as integrated intensity, average thickness, crystalline orientation, and average lamellar spacing of the crystalline nanoplatelets (Mazzanti et al., 2011).

Mazzanti et al. (2009) found that the lamellar thickness, computed from the diffraction peak position, was influenced by the applied shear. Under shear flow, the value of d-spacings tends to be larger (Mazzanti et al., 2009). Kaufmann et al. (2013) studied the effect of shear on the polymorphic behavior of milk fat via x-ray diffraction. They reported that shear can affect long spacings: statically-crystallized samples showed both 2L and 3L packing, but high shear rates destroyed 3L packing crystals and left only 2L packing ones (Kaufmann et al., 2013).

2.2.8　Steady-state structures under shear flow

The orientation of suspended anisotropic particles depends on the interplay between shear, interparticle, and Brownian forces. At early stages of crystallization, particles are separated by relatively large distances and inter-particle forces are negligible. The effect of shear can induce ordering, which dominates over disorder-inducing Brownian forces. Thus, crystals above a critical size may be oriented (Wiliam Kloek et al., 2005; Mazzanti et al., 2003; Tran & Rousseau, 2016).

Mazzanti et al (2003) found that shear can induce orientation of crystallites for a variety of fats (*e.g.,* cocoa butter, milk fat, milk fat stripped from polar lipids, and palm oil). A low shear rate (90 s^{-1}) resulted in little or no orientation in palm oil, while different degrees of orientation were observed in milk fat and cocoa butter. Higher shear rate (1440 s^{-1}) caused orientation in all the fats. Palm oil probably formed spherical clusters that moved and tumbled in the shear field rather than being oriented (Mazzanti et al., 2003), whereas the other fats had predominantly free anisotropic nanoplatelets. Crystals with large aspect ratios, and with larger longitudinal size, (*e.g.* cocoa butter) are more readily oriented than smaller ones (Mazzanti et al., 2003).

The effect of shear on nanoplatelet (CNP) size depends on the shear rates. According to Tran & Rousseau (2016), CNP size is a function of shear rate, as there is a critical shear rate above which the size is reduced. Below that critical shear rate, increasing the shear rate resulted in an increased thickness of nanoplatelets (Tran & Rousseau, 2016).

Above a critical shear rate, crystal breakage and secondary nucleation were promoted (Acevedo & Marangoni, 2014). According to Mudge et al. (2009), a critical shear rate for viscous heat generation exits (between 360 and 720 s^{-1}) for cocoa butter under laminar shear in a Couette-type shear cell. Above the critical shear rate, solid fat content decreased, and polymorphic transitions were suppressed (Mudge & Mazzanti, 2009).

According to Tran & Rousseau (2016), a spheroidal crystal structures, solid lipid meso-particles (SLMs), was observed in the narrow gap (2.5 mm) of a Couette cell. SLM size depended on the applied shear rate. Below a critical shear rate, crystal aggregation and growth were promoted due to a rapid surface integration on a damaged crystal surface.

Above the critical shear rate, aggregation of crystals was inhibited and even broke down. SLMs formed at an intermediate shear rate (30 s^{-1}) were thus larger than the those formed at a higher rate (240 s^{-1}) (Tran & Rousseau, 2016).

According to Acevedo and Marangoni (2014), the elastic modulus (G′) and yield stress (σ*) were reported to decrease for shared samples compared to statically-crystallized samples. This decreased elastic modulus (G′) and yield stress (σ*) for shared samples was contradictory to the general belief that smaller crystals lead to higher mechanical strength. This may due to differences in crystal growth mechanisms during storage. (Acevedo & Marangoni, 2014; R. Campos et al., 2002; Ghosh, Tran, & Rousseau, 2011; Suresh S. Narine & Marangoni, 1999; Pérez-Martínez, Alvarez-Salas, Charó-Alonso, Dibildox-Alvarado, & Toro-Vazquez, 2007).

3 EXPERIMENTAL METHODS AND MATERIALS

3.1 Research Plan

Figure 3.1 summarizes the research plan which consisted of four subplans: Differential scanning calorimetry (DSC), Rheometry, Polarized light microscopy (PLM), and X-ray diffraction (XRD). Although conducted separately, these subplans are closely linked. The details of these four subplans are discussed in the following sections.
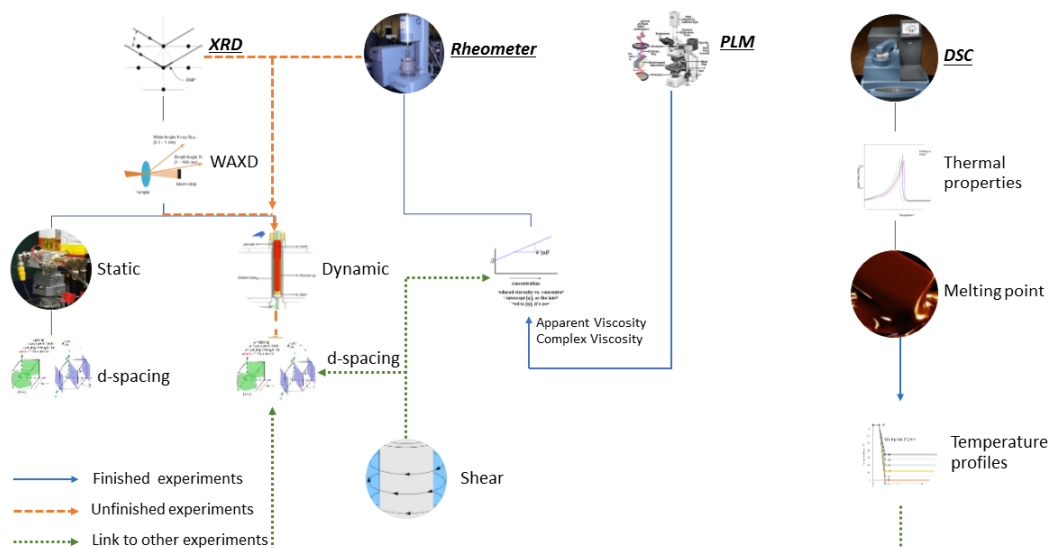
Figure 3.1 A research plan.

3.2 Differential Scanning Calorimetry Measurements

3.2.1 Materials

3.2.1.1.1 Sample Preparation

Tristearin (SSS) and Dodecane (DODE) were purchased from Sigma-Aldrich Chemical Co. and had a purity of at least 99%. No further purification was carried out. The 10% tristearin in dodecane solution was prepared by mixing the weighted materials in proportion on a weight per weight basis (w/w) (*e.g.,* The 10% tristearin solution was prepared by mixing 1.036 g tristearin in 9.012 g dodecane).

The 10% SSS solution was heated at 100 °C via water bath (Cole Parmer, USA) for 5 mins, which allows fat solids to completely melt and mix. Then hermetic aluminum pans and lids

were selected carefully and weighted via a microbalance (Cahn Instruments, C-33 Microbalance Model Number 13633-013, US) with a precision of ≤ 0.001 mg. The paired pan and lid must be close to the weight of the reference pan (the difference between the two sets within the range ± 0.05 mg). After selection, the pan and its lid were then immersed in acetone and dried by clean air, which can help to minimize possible contamination. During these operations, clean tweezers were used to avoid any contamination. Typical weight of an empty pan and lid is 50 mg.

Approximately 5 to 10 mg of melted sample was transferred to an empty hermetic aluminum pan by disposable capillary tubes with a wire plunger (Drummond Scientific Company, Wiretrol® II, US, 5 µL and l0 µL). After the sample was transferred, the pan and its lid were hermetically crimped by TA Instruments blue crimping press and then weighted again. Thus, the sample weight can be calculated as the difference of the weight of empty pan-lid set before and after loading of the sample. Sample pans and reference pan were stored in Eppendorf 1 mL plastic vials and labeled with the name and net weight of the sample. Weight of a samples were between 4 and 7 mg.

3.2.1.2 Differential Scanning Calorimetry (DSC)

Differential scanning calorimetry (DSC) measures the heat flow that is related to thermal events in a material as a function of temperature and time. These thermal events include exothermic peaks (heat evolution during crystallization), endothermic peaks (heat absorption during melting), and shifts in the baseline (change in the heat capacity). DSC has been used to study the thermal properties of fats, such as melting and boiling points, specific heat capacity, crystallization time and temperature, heats of fusion, *etc.*

In this research, DSC Q100 (TA Instruments Q100, New Castle, DE, US) was used to measure the thermal properties of 10% SSS solution. DSC Q100 (Figure 3.2) is comprised of a two-stage refrigerated cooling system (RCS) and can perform modulated DSC (MDSC®). DSC Q100 is connected to compressed nitrogen and air cylinders. The software Q Series™ Explorer is used to control DSC Q100 and record the experiment data (Al-Qatami, 2011).

In DSC Q100, there are chromel-constantan Type-E area thermocouples, which are fixed

to the underside of the disk platforms and measure the temperature difference between the reference and the sample thermocouples (ΔT). When the temperature of the furnace changes linearly, the differential heat flow between the sample and the reference can be estimated from ΔT via the thermal equivalent of Ohm's Law:

$$\frac{dq}{dt} = \frac{\Delta T}{R_D} \tag{68}$$

- Where: dq/dt is heat flow; ΔT is the temperature difference between the reference and the sample thermocouples, and R_D is the overall thermal resistance between these thermocouple disks

Figure 3.2 TA Instruments heat flux DSC Q100 equipped with modulated DSC connected to a refrigerated cooling system, RCS.

3.2.1.3 Calibration

To detect the possible contaminants, a cyclic empty cell run was performed from -60 to

200 °C at 20 C°/min. If the data is a deviation from the normal trace, a clean procedure must be done (please see Appendix A 6.1).

3.2.1.4   Experimental Procedures

A conditioning cycle was first done with an empty pan between the highest and the lowest temperature settings (0 °C to 80 °C) three times at 20 C°/min. After the conditioning step, sample and reference pan were loaded into the corresponding platform in the cell. Sample information was then recorded into the TA program. The procedure for DSC was programmed as follows (Figure 3.3):
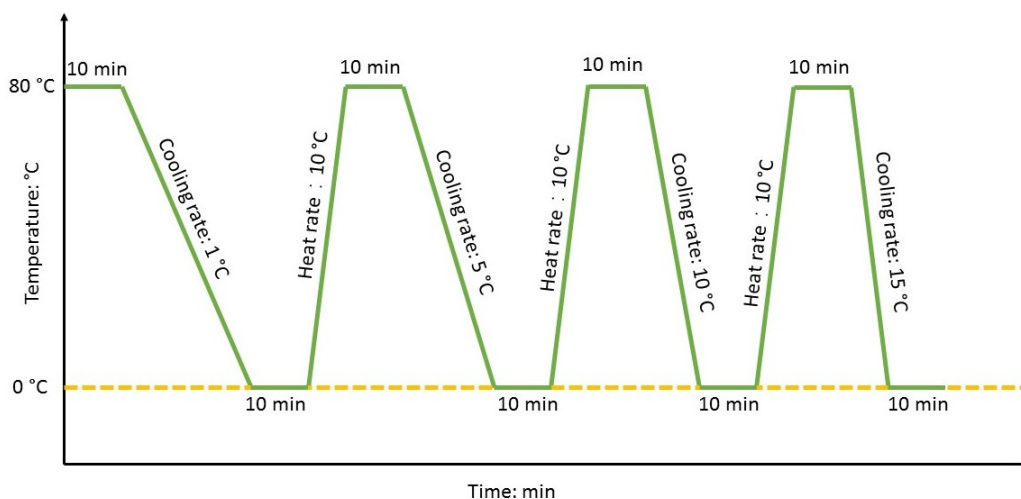
Figure 3.3 A temperature-time profile for 10% SSS solution in DSC experiment

The steps are described as follows:

  i.   Isothermal step, keeping the sample at 80.00 °C for 10 min.
 ii.   Cooling ramp to 0 °C at 1.00 C°/min to 0.00 °C
iii.   Isothermal step, 10 min isothermal plateau at 0 °C
 iv.   The heating ramp at 10.00 C°/min to 80.00 °C.
  v.   Isothermal step, keeping the sample at 80.00 °C for 10 min.
 vi.   Cooling ramp to 0 °C at 5.00 C°/min to 0.00 °C.
vii.   Isothermal step, 10 min isothermal plateau at 0 °C.
viii.   The heating ramp at 10.00 C°/min to 80.00 °C.

ix.   Isothermal step, keeping the sample at 80.00 °C for 10 min

x.   Cooling ramp to 0 °C at 10.00 C°/min to 0.00 °C.

xi.   Isothermal step, 10 min isothermal plateau at 0 °C.

xii.   The heating ramp at 10.00 C°/min to 80.00 °C.

xiii.   Isothermal step, keeping the sample at 80.00 °C for 10 min.

xiv.   Cooling ramp to 0 °C at 15.00 C°/min to 0.00 °C.

xv.   Isothermal step, 10 min isothermal plateau at 0 °C.

The experiment data was collected by TA software (New Castle, DE, US). In TA 2000 universal analysis (V4.5, New Castle, DE, US), the data can be opened as thermograms, which include signals of temperature, time, and heat flow. The analysis can be done in TA software or Microsoft Excel (exported data).

3.2.1.5   Data processing

As shown in Figure 3.4, a thermogram can be created with three synchronized signals data, heat flow (*i.e.,* the energy flow difference between reference pan and sample pan), temperature and time.
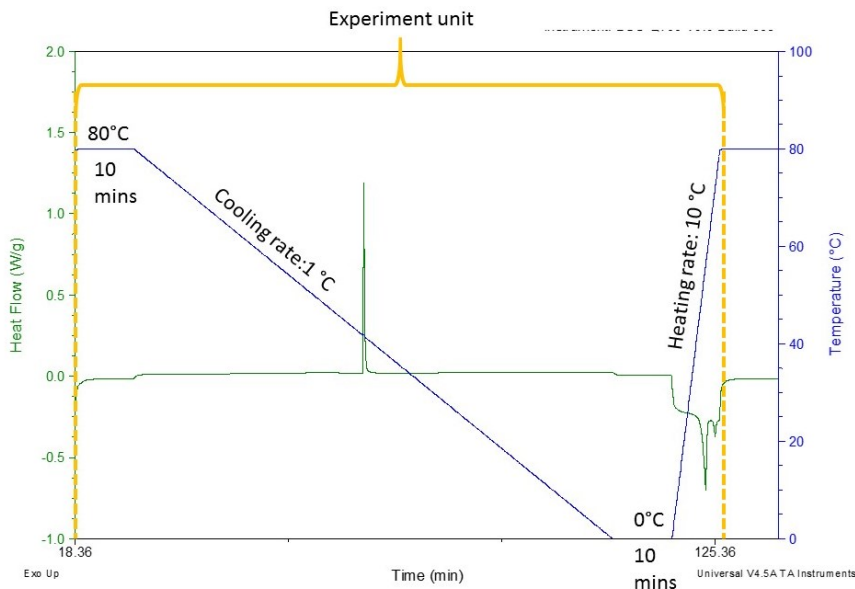
Figure 3.4 Example of a heat flow versus time versus temperature thermogram of 10% SSS solution.

Plots like Figure 3.4 can easily compare three factors (time, temperature, and energy) together. In this research, for convenience, the heat flow versus temperature plot was used

66

to analyze the thermal properties of the sample (Figure 3.5). The peaks in the upper plot are exothermic and are associated with heat evolution during crystallization. In the lower part, the endothermic peaks are related to the heat absorption during melting. TA universal analysis (V4.5A, New Castle, DE, US) provides an automatic integration function to estimate the enthalpy with a sigmoidal baseline (purple dash area). This function is limited to horizontal take-off and landing. Therefore, one drawback is that the function does not successfully account for the change in specific heat (*i.e.*, the slope of the signal before and after the transition) (Wang, 2016b). Also, the onset/peak temperature can be estimated automatically by TA software. The preliminary analysis was done in TA Universal Analysis and the result was then exported to a spreadsheet for further study.
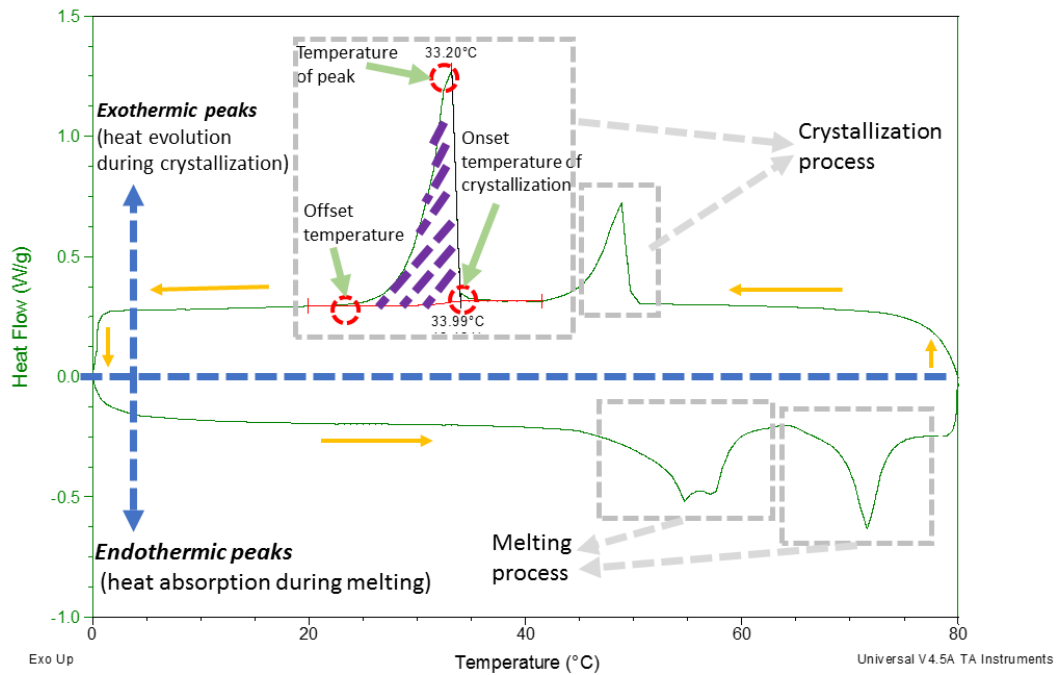
Figure 3.5 Example of a heat-flow versus temperature thermogram of 10% SSS solution. In this thermogram, the yellow arrows show the temporal sequence of events. The onset of crystallization is around 33 °C.

3.3 Rheology Measurements

3.3.1 Material

3.3.1.1 Sample Preparation

The 10% SSS solution was heated at 100°C via water bath (Cole Parmer, USA) for 5 mins,

which allows fat solids to completely melt and mix. 12.5 ml of melted sample was transferred to the rheometer cell via Fisherbrand™ Disposable Borosilicate Glass Pasteur Pipets (Waltham, MA USA). After loading the sample, the two-piece cover (Figure 3.6 (b)) was installed on the top of the rheometer cup to reduce volatile compound loss.

3.3.2 Instruments and Methods

3.3.2.1.1 AR 2000 Shear Dynamic Rheometer

AR 2000 shear dynamic rheometer (TA Instruments, Mississauga, Ontario, Canada) (Figure 3.6 (a)) was used to measure the rheological properties of 10% SSS solution (*e.g.,* viscosity, storage modulus, loss modulus) as SSS crystallized out from the solution. This crystallization formed a suspension of crystals and crystal clusters in a saturated solution of SSS in dodecane.

For AR 2000, the main unit is mounted on a cast metal stand, with the electronic control circuitry contained within a separate electronics control box (Figure 3.6 (a)). The main unit includes the motor, an optical encoder, and the concentric cylinder geometry (*i.e.,* a standard cup configured with a DIN (German Industrial standards) rotor). The standard cup is on the base of the main unit and includes a Peltier temperature-controlled system connected to a water bath. AR 2000 is an advanced rheometer, which has broad torque range, superior strain resolution, wide frequency range, and can control strain and monitor stress performance.
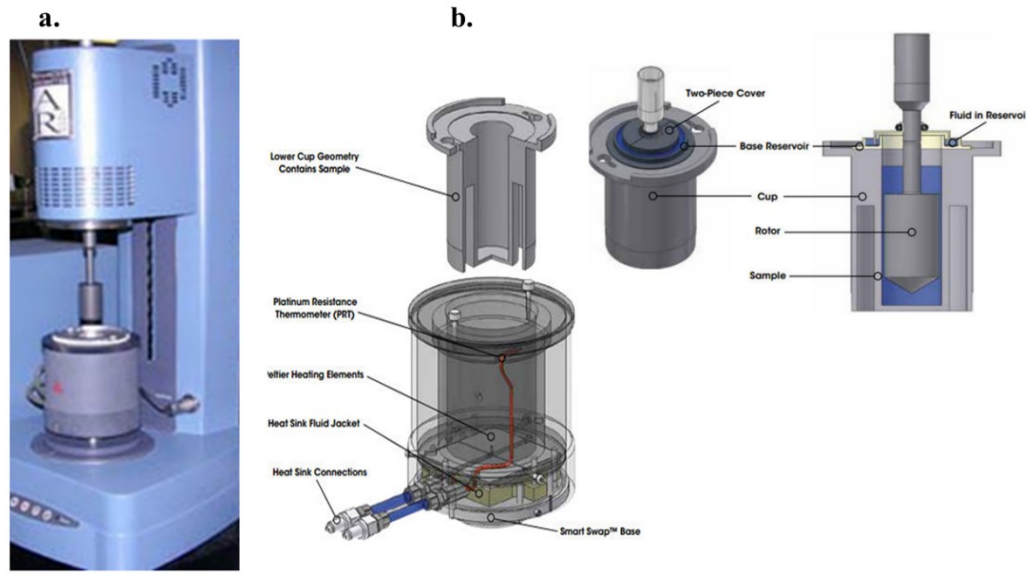
Figure 3.6 (a) AR 2000 shear dynamic rheometer (TA Instruments, Mississauga, Ontario, Canada) (b) A geometry (cup and cone) in this experiment. Modified from AR 2000 manual.

3.3.2.1.2 Calibration

When the instrument has finished the system check, a series of calibration procedure was done before the experiments (*i.e.,* geometry inertia, bearing friction correction, rotational mapping, zero the gap and system inertia). Please see appendix A 6.2 for details.

3.3.2.1.3 Experimental Procedure

The temperature and shear profiles were set as follow:

- Crystallization temperature: -5, 0, 5, 12, 20, 28, 35 °C
- Shear rate: 0.9, 9, 90, 900 s^{-1}

Thus, a five steps procedure was designed as follows (Figure 3.7):

a. ***Conditioning step:*** samples were kept at 65 °C for 5 mins with shear 100 s^{-1} to erase all crystal memory.

b. ***Cooling step:*** samples were cooled to the crystallization temperature (-5, 0, 5, 12, 20, 28 and 35 °C) without shear (cooling rate: 1.7 to 4.5 C°/min).

c. ***Pre-Oscillatory step:*** After reaching the desired crystallization temperature, an oscillatory rheology test was applied for 200 s to measure dynamic moduli (G', G") at a strain of 4.500E–3 and a fixed frequency of 1 Hz.

69

The combination of a very low strain (4.500E–3) and frequency (1 Hz) can help to avoid disturbances to the crystallization process as much as possible while maintaining a sufficiently high data sampling rate (De Graef, Van Puyvelde, Goderis, & Dewettinck, 2009).

d. ***Shear step:*** the selected shear rate is maintained for 1200 s at the selected crystallization temperature.

e. ***After-Oscillatory step:*** After the shear step, an oscillatory rheology test was applied for 200 s to measure dynamic moduli (G', G") at a strain of 4.500E–3 and a fixed frequency of 1 Hz.
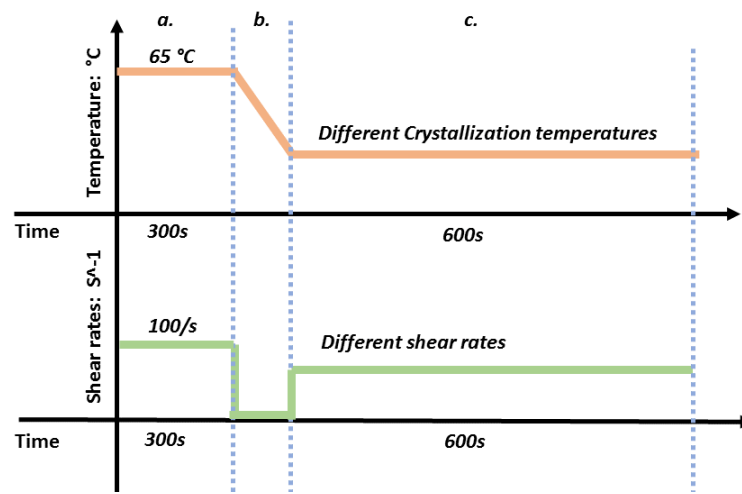
Figure 3.7 The temperature and shear profile of the rheology experiments for 10% SSS solution.

3.3.2.1.4 Data Processing

AR-2000 is controlled by the Rheology Advantage software (TA, New Castle, DE, US) (Figure 3.8). The data can be collected in this software. After experiments, the data will be saved (in. rsl format) and imported into the Data Analysis software (TA, New Castle, DE, US).
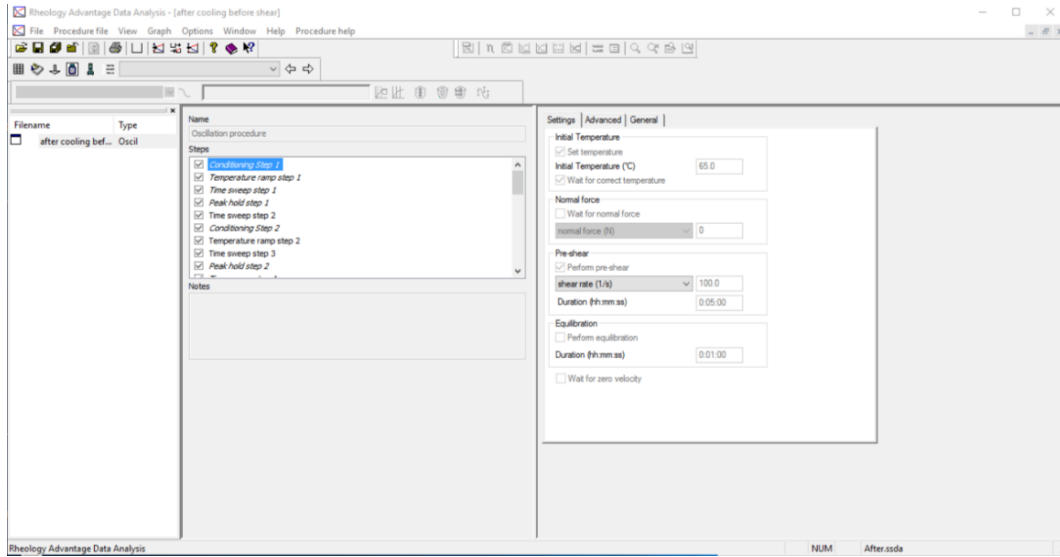
Figure 3.8 An example of the Rheology advantage software GUI.

In the Data Analysis software, a plot can be created as a function of time. The y-axis can be modified to various parameters (*i.e.,* apparent viscosity, complex viscosity, dynamic modulus, *etc.*). An example of complex viscosity versus time is shown in Figure 3.9. A plot of complex viscosity versus time was created and analyzed. The data was then exported to a spreadsheet for further analysis.
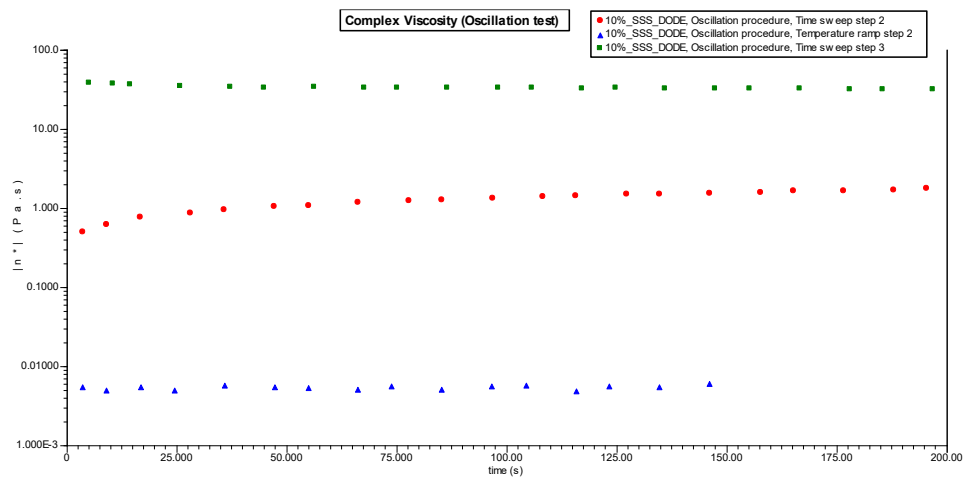
Figure 3.9 An example of complex viscosity versus time plot.

3.4   Polarized Light Microscopy Measurements

3.4.1   Material

3.4.1.1   Sample Preparation

The 10% SSS solution was heated at 100 °C via water bath (Cole Parmer, USA) for 5 mins, which allows fat solids to completely melt and mix. Approximate 70 µL of melted sample was transferred to the empty shear cell by disposable capillary tubes with a wire plunger (Drummond Scientific Company, Wiretrol® II, US, 5 µL and l0 µL). The melted sample was then kept at the center of Linkam cell. When the lid was winded down to the 100 µm (gap distance), the sample would be squeezed and distributed, forming a thin layer over the cell surface.

3.4.2   Instruments and Methods

3.4.2.1   Polarized light Microscopy

Polarized Light Microscopy (PLM) can directly observe the birefringent solid microstructural elements of the fat crystal network as sharp, bright features against a dark background. PLM can be used to image early crystal growth. PLM can also estimate the crystallization induction time (τ) (*i.e.*, the time when crystals reach the critical size that allows them to be visible). The crystallization induction time (τ) measured from the PLM reflects the early crystallization events (Rodrigo Campos, 2013).

In this research, a polarized light microscope (Olympus BX 51, Shinjuku, Japan) is used to obtain the polarized light images of the samples (Figure 3.10). The Olympus BX 51 is connected to a Charge-Couple Device (CCD) camera (Retiga 2000R, Qimage, Canada), a phase contrast (ph1) long working distance (WD 10.0 mm) 10X objective lens (UPlanFl), and a Linkam CSS 450 cell (Linkam CSS 450, Linkam, Surrey, UK). The shear rates and temperatures are controlled by software, Linksys 32 (Linkam, Surrey, UK) during experiments.
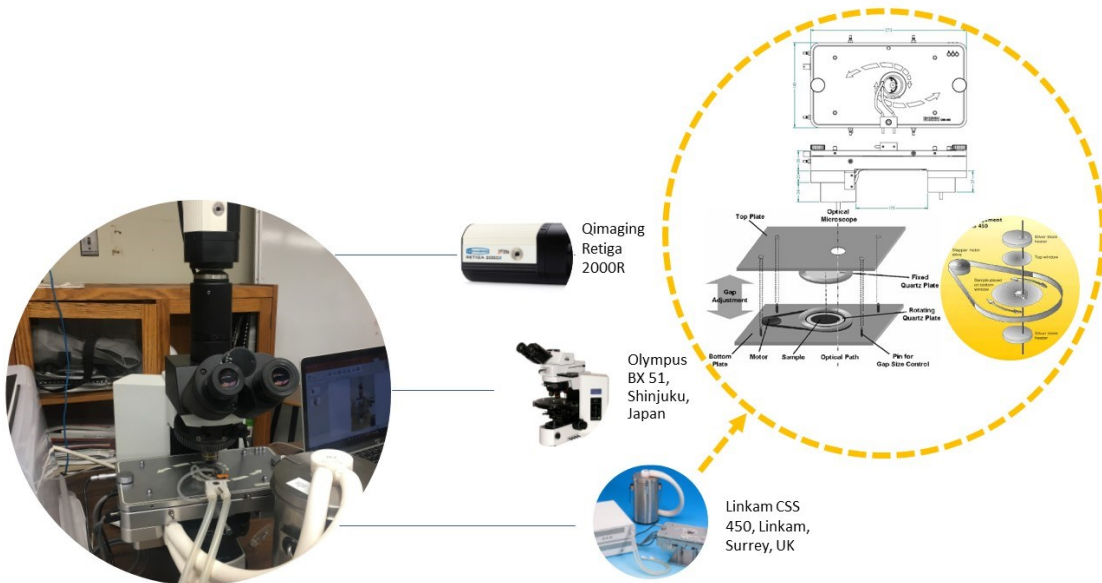
Figure 3.10 Olympus BX51 Polarized Light Microscope with Linkam CSS 450 cell. Modified from (Ma, Mackley, & Chinesta, 2008).

Linkam Optical Shearing Stage CSS 450

As shown in Figure 3.10, Linkam CSS 450 is an optical shearing stage, which allows a direct observation of a complex fluid via any standard optical microscope (*e.g.,* polarized optical microscope). This Linkam stage can provide a straightforward viewing of the change in fat microstructure during crystallization. The cell can control temperature from -50 to 450 °C with a temperature stability of ± 0.2 °C, with heating/cooling rate from 0.01 to 30 C°/min

The gap between the lid and stage can be adjusted from 5 to 2500 µm via Linkam 32. In this research, the gap was set to 100 µm. The amount of sample can be calculated via:

$$V_{sample} = \pi \cdot r^2 \cdot \left(\frac{\delta}{1000}\right) \tag{69}$$

- Where: r=15mm (radius of the sample cell); δ =100 µm

Therefore, the maximum amount of sample for 100 µm gap is approximate 70 µL.
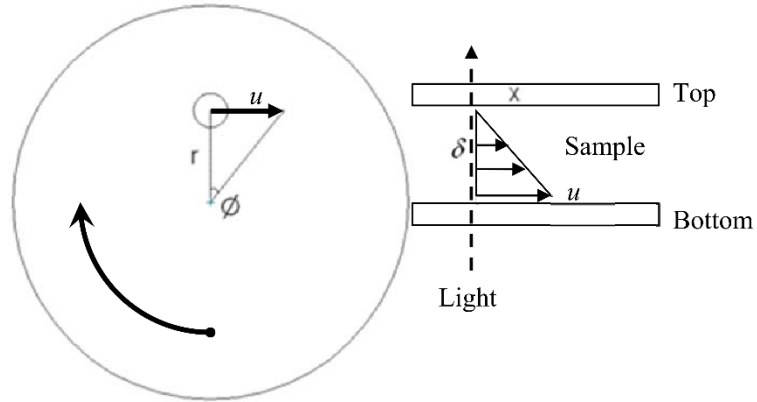
Figure 3.11 Simple schematic of shear cell. Modified from Linkam's manual (CSS 450).

For CSS 450 cell (Figure 3.11), shear is produced by the rotation of the bottom window (the top window is stationary). Therefore, a velocities gradient is formed. The velocity is zero at the top and maximal at the bottom. The value of vertical shear rate ($\dot{\gamma}$) can be calculated from the ratio between the tangential velocity 'u' and the gap 'δ':

$$u = r\dot{\omega} \tag{70}$$

$$\dot{\gamma} = \frac{u}{\delta} \tag{71}$$

$$\dot{\gamma} = \frac{r\dot{\omega}}{\delta} \tag{72}$$

- Where: is the angular velocity (radians/second); r is the observation radius (from the center of the bottom window of the shear cell stage to the center of the hole in the aperture, r=7.5mm for CSS 450 shear cell); and δ is the gap between the top and bottom plates of shear cell (δ=100 μm in this experiments).

QIMAGING RETIGA 2000R CAMERA

As shown in Figure 3.10, the CCD digital camera, Qimaging Retiga 2000R, was used to obtain the images during experiments. The camera is featured with a resolution of 1.9 megapixels (1600 x 1200) with a pixel size of 7.4 μm x 7.4 μm. The images can be exported in 12-bit/pixel digital format. 2000R sensor has a maximum frame rate of 190 frames per second (fps). The camera can capture up to ten fps in full resolution if enough light is available.

LINKSYS32

In this research, the Linksys 32 software (Linkam, Surrey, UK) was used to communicate with the CSS 450 stage and display the output of the QIMAGING RETIGA 2000R camera. In the Linksys32 software, the temperature and shear rate can be controlled directly (Figure 3.12) or programmed in a new window. The video capture toolbar (Figure 3.12 (a)) can help to adjust the delay time (s) for two subsequent images. The movement of the shear cell (*i.e.,* angular velocity and direction) and the gap between two plates (from 0 to 2500 µm) can be controlled in the shear control toolbar (Figure 3.12 (b)).
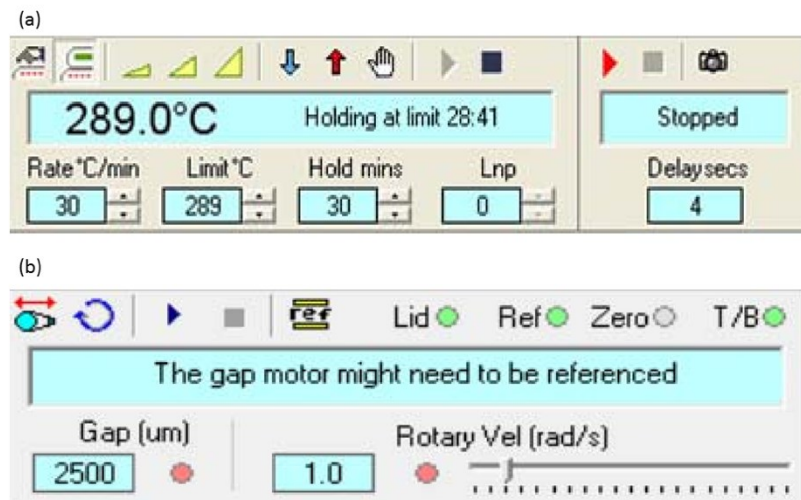
Figure 3.12 (a) Temperature and video capture toolbar. (b) Shear control. Modified from (Arora, 2015).

3.4.2.2   Calibration and alignment

The optical components of PLM must be aligned before image acquisition. To obtain a high quality image, the light source needs to be centered and in line arrangement with the condenser and field diaphragm. After alignment, 10X objective lens needs to be calibrated using a stage micrometer For 10X objective lens, the physical size of an image is aprroximately 1.2 x 0.9 mm (calibration scale: 0.7 µm/pixel). Please see appendix A 6.3 for details.

3.4.2.3 Experimental Procedure

Imaging

In this research, QImaging Retiga 2000R camera was used to acquire images. The quality of the image depends on the balance of several factors (*e.g.,* exposure time, light intensity, aperture of diaphragm, *etc.*). The parameters were adjusted to maintain the quality of images and keep the necessary frame rate in the different shear rates set experiment. The images were collected and saved (JPEG-LS lossless format) in the Linksys 32 software.

Temperature and shear control

Before any experiment, a condition step (a) was first performed to erase all crystal memory. After step a, the sample was cooled down at 15 C°/min to a selected crystallization temperature statically. In the next step, the sample was kept at a selected shear rate isothermally. The detailed experimental procedures are described as follows (Figure 3.13):
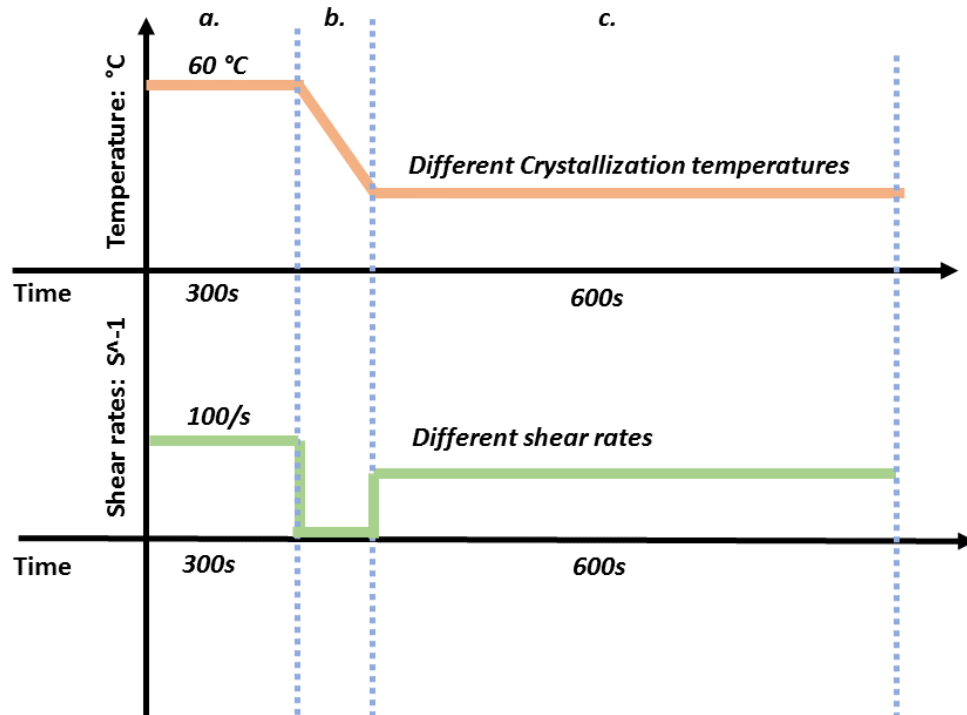
Figure 3.13 Temperature and shear profile for polarized light microscope measurement.

a. ***Conditioning step:*** sample was kept at 60 °C for 5 mins with 100 s^{-1} to erase all crystal memory.

b. ***Cooling step:*** sample was cooled at 15 C°/min to the crystallization temperature (-5, 0, 5, 12, 20, 28, 35 °C).

c. ***Shear step:*** sample was kept at a constant shear rate (0.9/9/90/900 s^{-1}) under constant crystallization temperature.

3.4.2.4   Data Analysis

Image analysis

The first step in image analysis is to use the threshold function in ImageJ (Figure 3.14 (a)) to process the accumulated images. Threshold function can convert a grayscale image into a binary image or removes pixels that comply with a specified rule. Threshold function separates out regions of the image corresponding to the objects that need to be analyzed. After thresholding, images in the range of 0-255 (grayscale) can be divided into a foreground and background. Generally, 0 is regarded as complete black and 255 as complete white (Arora, 2015). The threshold point should be carefully chosen because it must represent the microstructure imaged in the original grayscale images and will be applied to all the micrographs in the series (Rodrigo Campos, 2013). The threhold value can be set automatically by using the "auto" function in ImageJ.

In Figure 3.14 (c), the threshold image was obtained by setting the value of threshold point at 128. Thus, in Figure 3.14 (b), anything below 128 will appear as black while anything above 128 will display as white. The SSS crystals are represented by white feathers on a black background. After applying the same threshold value in one stack, the result (ratio of white pixels / total pixels) of each image will be displayed in a new window. A plot of % white versus time can be made in a spreadsheet after importing the threshold data from ImageJ (Figure 3.15).

(a)   (b)   (c)
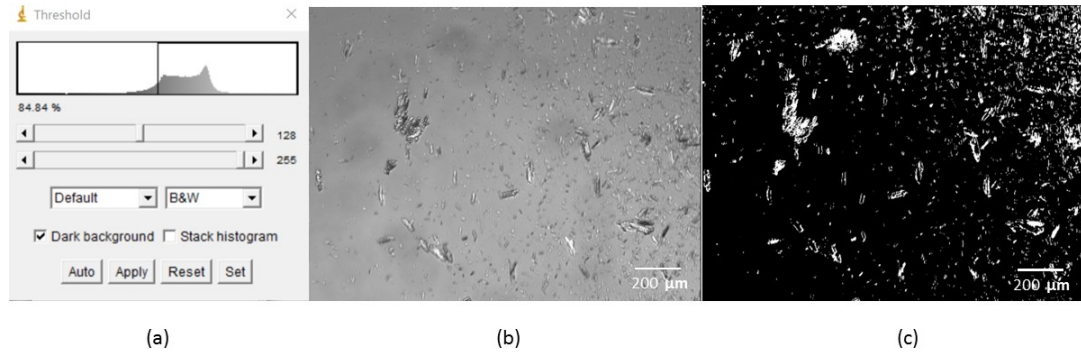
Figure 3.14(a) Thresholding GUI of ImageJ. (b) Micrograph of 10% SSS crystal suspension at 35°C and 0.9 s^{-1}. (c) The thresholded image of image (b).
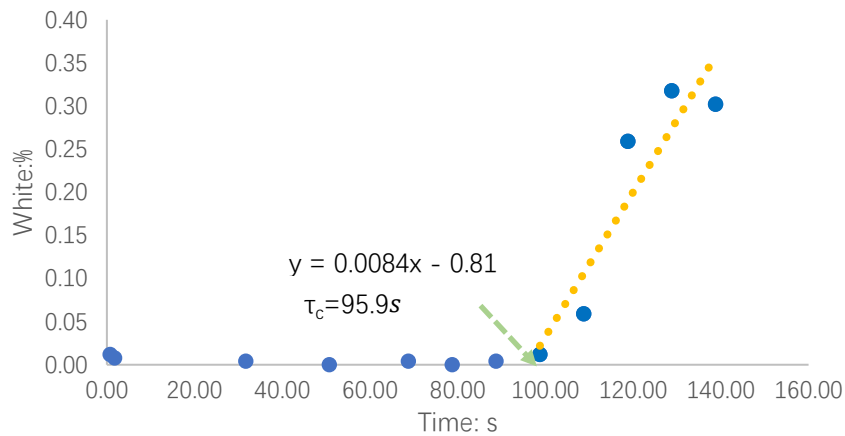
Figure 3.15 Estimation of the time (τ_c) required for SSS crystals to reach the critical size allows them to be visible under PLM (at 35°C and 0.9 s^{-1}).

Figure 3.15 can be used in imaging early crystal growth. Here, early crystal growth, in this case, refers to the instance when SSS crystals reach the critical size and can be detected by the microscope (at the magnification scaled used) under the designed temperature and shear rate.

In other words, PLM allows us to estimate the time (τ_c) that is required for crystals to reach the critical size and be visible under microscopy. In Figure 3.15, time zero is referred to the beginning of the cooling step. The value of τ_c can be determined by extrapolating from the linear trendline of the crystallization data to the time axis. The value of x-axis intersection point is refered as τ_c.

3.5 In-House Wide-Angle X-Ray Diffraction Measurements

3.5.1 Material

3.5.1.1 Sample Preparation

The 10% tristearin solution was melted at approximately 75 °C using a hot plate (Cole-Parmer, USA). 20-30 µL of sample was transferred to a capillary (Charles Supper Co., 1.5 mm diameter, 10 µm wall) by using a preheated disposable capillary tube with a wire plunger (Drummond Scientific Company, Wiretrol® II, Cat. Number 5-000- 2010, 5 µL and l0 µL), and sealed by fire.

3.5.2 Instruments and Methods

3.5.2.1 In-house Wide-Angle X-Ray Diffraction

The instrument setup of in-house WAXD is shown in Figure 3.16. The X-rays were generated by a Commercial GeniX X-ray source (Xenocs Corporation, Sassenage, France). This GeniX X-ray source produces Mo Kα radiation X-rays, with 0.7093 Å wavelength. X-rays are focused by a mirror and then collimated by two sets of scatterless slits, which are aligned on a small diameter vacuum fly-path. Right after passing the fly-path, X-rays (beam size: around 0.4 mm x 0.5 mm) are projected to the sample capillary in the capillary holder.

A XRI-UNO/Si 2D X-ray detector (XRAY-IMATEK, Barcelona, Spain) was used in this research. The detector is built was a single chip array of silicon sensors and its active area was 14 mm × 14 mm (pixel size (ps) was 0.055 mm ×0.055 mm). A 'XRI-UNO' software was used to control the detector and collect images. The in-house XRD system was isolated from the surrounding to minimize the possible environment influence and danger of X-ray exposure.
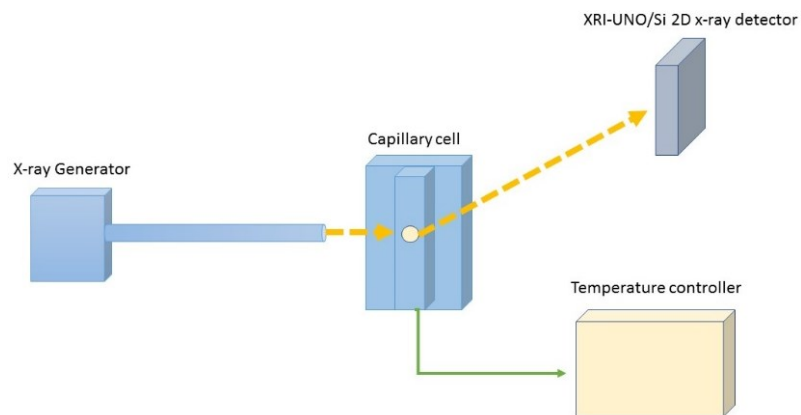
Figure 3.16 in-house WAXD set up.

3.5.2.1.1 Experimental setup

Temperature control system

The temperature control system set up is shown in Figure 3.17. The temperature control system consists of five parts: capillary cell, water bath, flow switch, temperature controller, and computer.
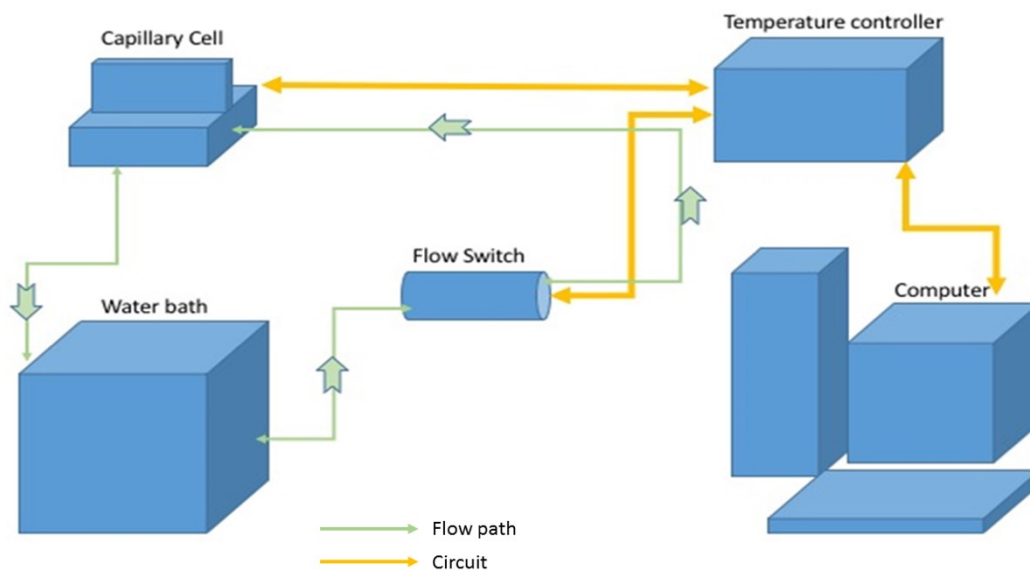
Figure 3.17 Schematic representation of temperature control system configuration.

Water bath

A water bath (Thermo Fisher Scientific, USA) was installed and connected to the capillary

cell (heat unit). The water tank was filled with a mixture of distilled water and glycol (prevent freezing below 0 °C). The temperature of the water bath was set at 0 °C. Moreover, the pipes between the water bath and the capillary cell were wrapped by an insulation foam to minimize the thermal loss.

Flow switch

The in-house X-ray system consists of many high-power types of equipment that can release a significant amount of heat. Therefore, the air is hotter and drier, which can absorb more moisture from the water bath. The cooling medium will stop the circulation when the mixture (distilled water and glycol) is not sufficient in the tank. The capillary cell might burn out without cooling, especially in longer time experiments.

A flow switch (Figure 3.18) was installed between the outlet of the water bath and inlet of the capillary cell. The flow switch connects to a relay in the temperature controller. The switch works as a "fuse", which can protect the capillary cell by opening the circuit when there is no flow passing the switch. Three modes, Auto, Off, and Manual, were designed to control the flow switch. When in "Auto" mode, the flow switch can open the circuit automatically when there is no flow in the switch. When in "Manual" mode, the flow switch could be operated manually. The "Off" mode would disable the function of the flow switch.
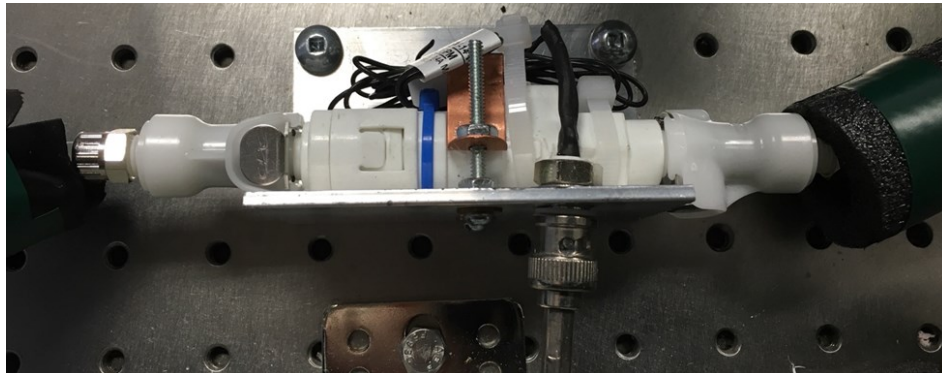
Figure 3.18 The configuration of the flow switch.

Capillary cell

A capillary cell was connected to the temperature controller. This capillary cell can heat up or cool down the capillary. To reduce thermal loss, a customized insulation foam cage (Figure 3.19) was made and installed on the capillary cell. This insulation cage includes a removable lid and a fixed bottom. There are inlet and outlet for X-ray beam on the front and back of the bottom foam. The inlet was designed as a tiny hollow cylinder, sealed by a Kapton ® polyimide film on both ends. The outlet was designed as a hollow 60 ° cone, sealed by Kapton ® tape at both ends. This design can help to reduce intensity loss of X-ray and keep a good insulation for the cell.
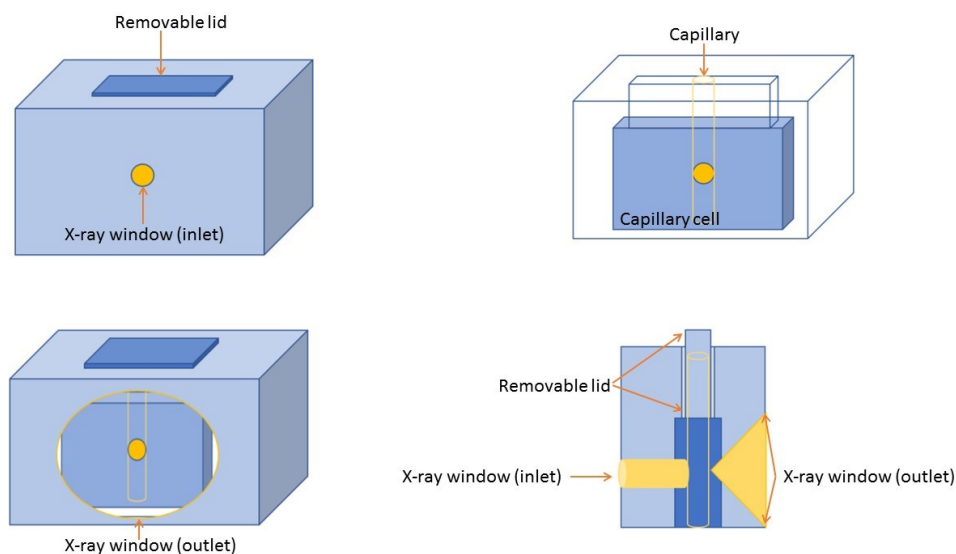
Figure 3.19 Schematic representation of the insulation foam cage (with the cell).

Temperature controller

A temperature controller (Figure 3.20) was connected to the computer, allowing the communication between a LabVIEW program (computer) and temperature control system. The LabVIEW program was designed by Dr. Gianfranco Mazzanti and Dr. Stefan Idziak, and upgraded by Pavan K. Batchu. The experiment temperature can be monitored and recorded precisely via this software.
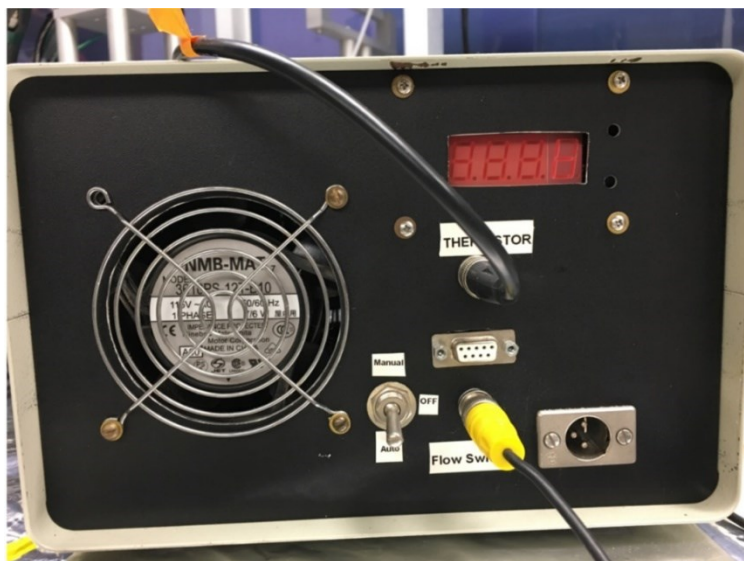
Figure 3.20 The temperature controller.

3.5.2.2 Calibration

Before any experiments, a series of centering procedures must be applied in order to obtain an accurate result (please see appendix A 6.4 for details).

3.5.2.3 Experimental Procedure

Imaging

In this research, a XRI-UNO detector was used to acquire images. The quality of images depends on several parameters (*e.g.,* exposure time, X-ray intensity, frame rate, *etc.*). These Parameters were then adjusted to optimize quality of images. Images were collected and saved by the XRI-UNO software (XRAY-IMATEK, Barcelona, Spain) in .bin format.

Temperature control

A condition step (a) was first performed to erase all history. After conditioning step (a), sample capillary was then cooled down at 3 C°/min to a selected crystallization temperature. The detailed procedures are described as follows (Figure 3.21):

a. ***Conditioning step:*** sample was kept at 70 °C for 10 mins to erase all history.
b. ***Cooling step:*** sample was cooled at 3 C°/min to the selected crystallization temperature (-5, 0, 5, 12, 20, 28, 35 °C).

c. ***Isothermal step:*** After reaching the selected crystallization temperature, an
isothemal step was applied for 600 mins.
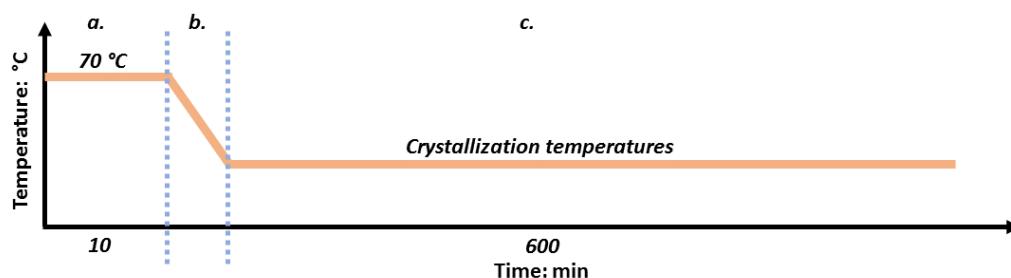
Figure 3.21 Temperature profile of in-house WXRD experiment for 10% SSS solution.

In this research, the temperature of capillary cell was controlled by a LabVIEW program (Figure 3.22), which was developed by Dr. Gianfranco Mazzanti and Dr. Stefan Idziak and upgraded by Pavan K. Batchu. This program allows user to input the temperature profile via a graphical user interface (GUI). The system information, such as the time, actual temperature, and set point temperature of capillary cell for each temperature cycle, was also saved in the log file.
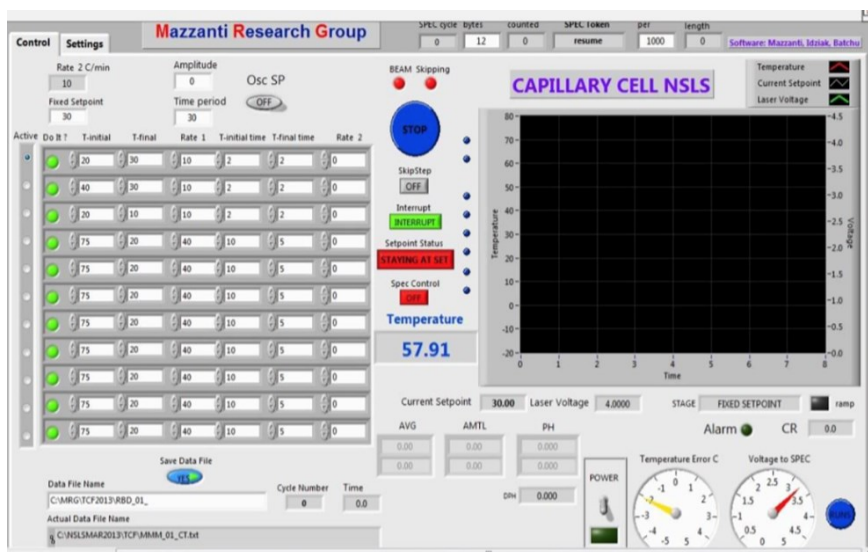
Figure 3.22 A GUI interface of the capillary cell temperature control program (Provided by Pavan K. Batchu).

3.5.2.4 Data processing

Images (8-bit raw) taken under the same temperature were opened as a stack (a series of images that shares a single window) with size 256 X 256 pixels in ImageJ software. A single image was then made from this stack via Z project function. At last, this single image was saved in a 16-bit format, which allows to create a radial plot via ImageJ plug-in program, XR2D (developed by Stefan Idziak, Gianfranco Mazzanti, Maochen Hannah Wang, and Kisun Park).

In XR2D program, XRD 2D image can be reduced to 1D plot of intensity as a function of scattering vector q. This 1D plot is made by taking a radial average of intensity at increasing value of q or pixel values. Thus, a radial plot can keep the XRD information such as peak position, X-ray scattering intensity and full width at half maximum (FWHM), which was then exported in "text image format" (standard tab-delimited ASCII text file) for curve fitting and peak fitting in Igor Pro 6.0 (Wavemetrics Inc). Please see appendix B 7.1.

4 RESULTS AND SOME DISCUSSION

4.1 DSC

In this research, the thermal properties of 10% SSS solution were studied at different cooling rates. Thermal behavior data were analyzed using thermograms as shown in Figure 4.1. In these thermograms, there are two peaks during crystallization. The peaks are seen in the cooling portion of the thermogram (either 1, 5, 10 or 15 C°/min), which is above the blue dotted zero line. At least two peaks are also observed during melting-dissolution, as the sample was heated. These peaks are under the zero-heat flow line, *i.e.,* they appear inverted. With this information, we can provide an educated hypothesis about the thermal events that caused these peaks. Peak 1 and Peak 2 are exothermic peaks, due to the heat released during formation of two types of crystalline forms. Recall that the tristearin is crystallizing from solution, and that the dodecane does not crystallize from -5 °C to 35 °C. Peak 3 and Peak 4 are endothermic peaks that corresond to the heat absorption during melting. The exothermic and endothermic peaks will be reported and discussed separately in the following section (Pan 1: 4.142 mg, Pan 2: 6.369 mg).
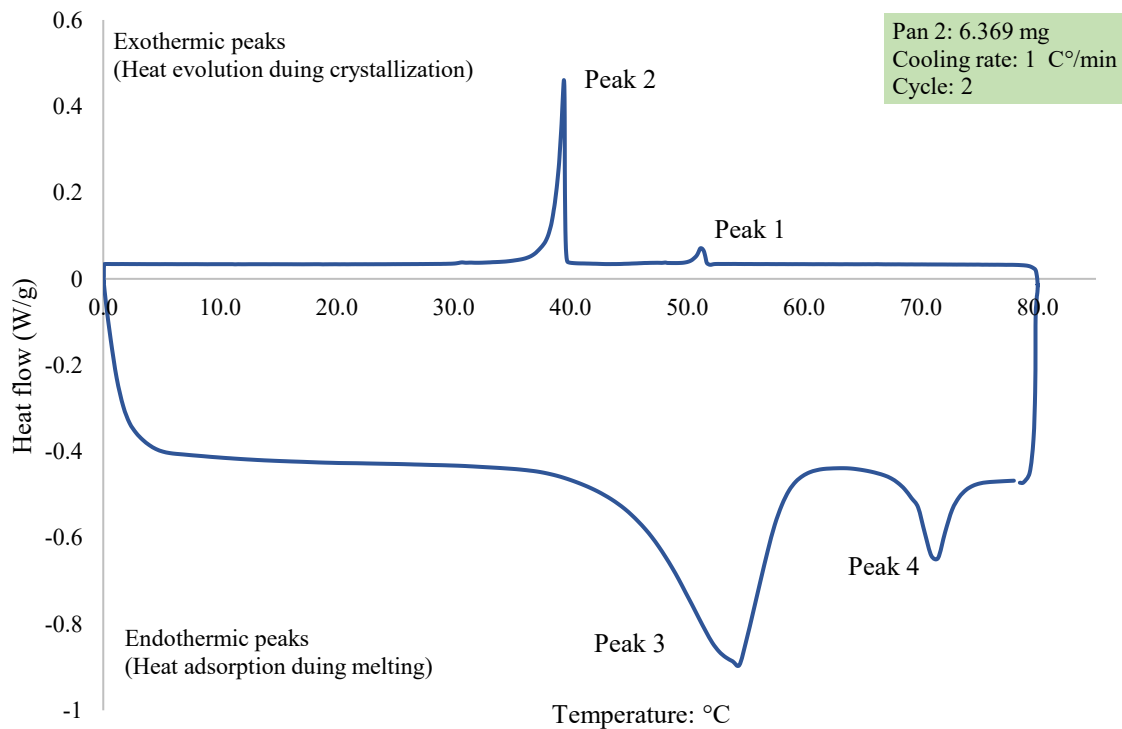
Figure 4.1 An example of a raw heat flow (W/g) versus temperature (°C) thermogram of 10% SSS solution, cooled at 1 C°/min. Peak numbers are clearly indicated.

4.1.1 Crystallization Temperature

In Figure 4.2, the exothermic peaks obtained at different cooling rates were overlaid together in a single plot for each kind of peak, (a) for Peak 1, and (b) for Peak 2. The onset and peak temperatures were calculated using "TA Universal Analysis V4.5A" software. The temperature values from ten replicates (2 pans, each pan 5 cycles) were averaged and plotted.
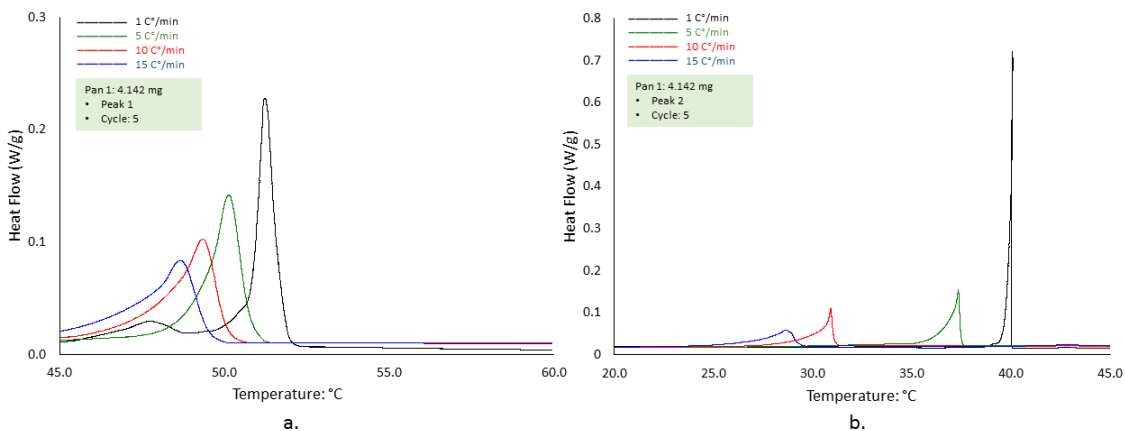
Figure 4.2 An example of analysis of the onset temperature for Peak 1 (a) and Peak 2 (b) of 10% SSS solution (under the same cycle) for Pan 1 (4.142 mg) (all the data is normalized to 1 C°/min).
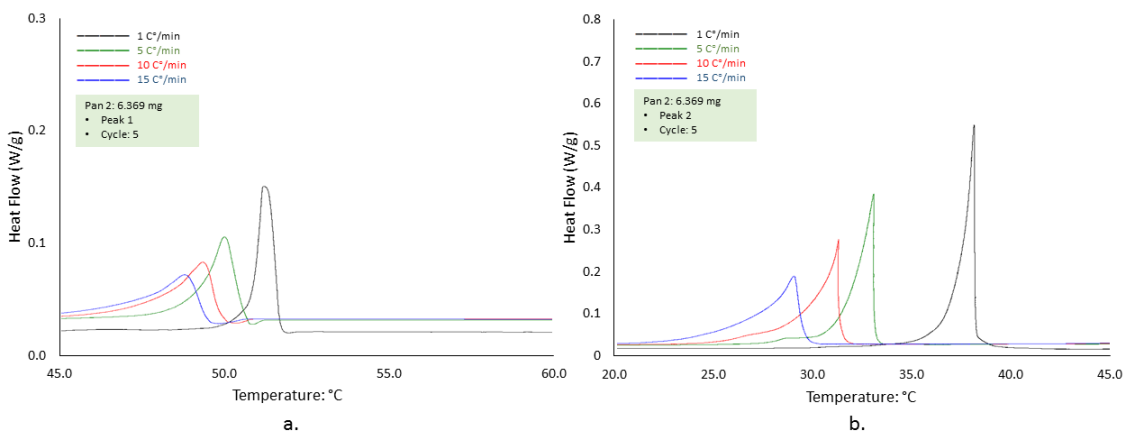
Figure 4.3 An example of analysis of the onset temperature for Peak 1 (a) and Peak 2 (b) of 10% SSS solution (under the same cycle) for Pan 2 (6.369 mg). (all the data is normalized to 1 C°/min).

Peak 1

As shown in Figure 4.1, Peak 1 is associated with the first exothermic event during cooling.

87

Figure 4.2 (a) shows that when the cooling rate increases, the onset temperature and peak temperature of Peak 1 shift to a lower value. Very little difference was observed between onset and peak temperature values. Hence, in Figure 4.4, the difference between the onset temperatures at 1, 5 and 10 C°/min and the onset value at 15 C°/min are plotted as a function of the cooling rates. The maximum value of the onset temperature (51.65 ± 0.07 °C) as expected, corresponded to cooling at 1 C°/min. When cooling rate increases, the difference between peak onset temperatures decreases, which means the onset temperature became lower and close to the reference value (at 15 C°/min).
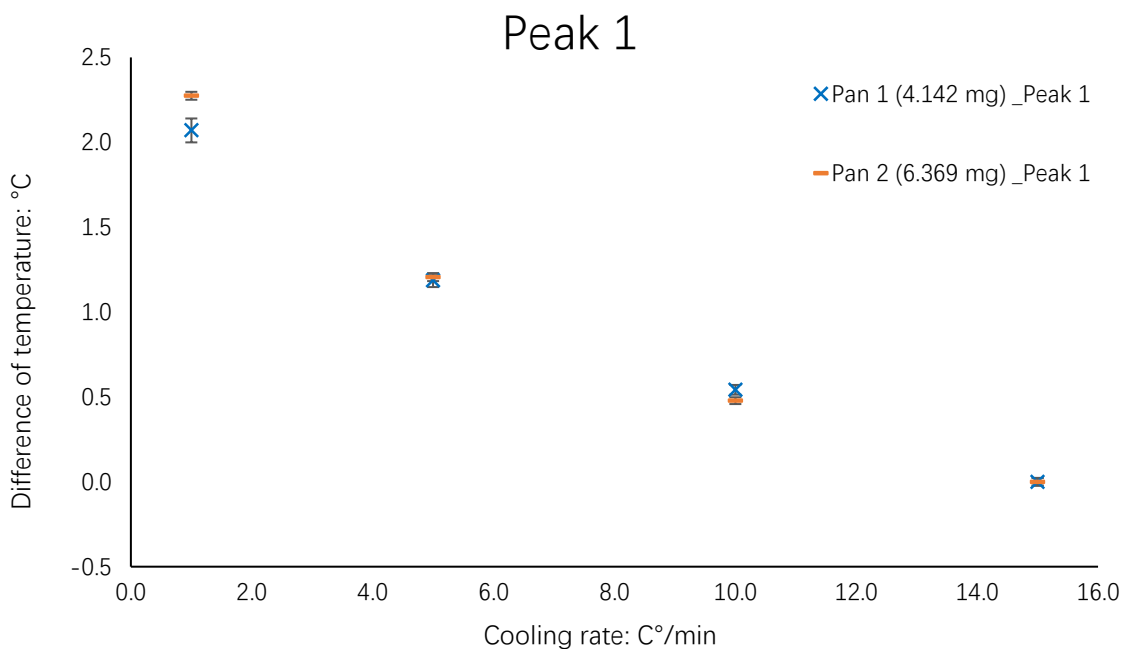
Figure 4.4 Difference between the onset temperatures of Peak 1 at 1, 5 and 10 C°/min and the onset value at 15 C°/min (internal reference for each pan) are plotted as a function of the cooling rates for Pan 1 and Pan 2 separately. Error bars are smaller than the symbols in the graph.

Peak 2

As shown in Figure 4.2 (b), Peak 2 is associated with the second exothermic event during the cooling step. Peak 2 has a larger area under it than Peak 1, which corresponds to a larger enthalpy value (e.g., at 1 C°/min, Peak 2 is 23.24 ± 1.72 J/g and Peak 1 is 2.92 ± 0.39 J/g).

At the slowest cooling group (1 C°/min), the onset temperature is 40.20 ± 0.85 °C, which is the maximum value among other groups. For comparison between different groups, the temperature differences between 15 C°/min and other cooling rates (1, 5, and 10 C°/min) are plotted as a function of cooling rate for Pan 1 and Pan 2 separately (Figure 4.5). When cooling rate increases, the difference of onset temperature decreases, which means the onset temperature became smaller and closer to the reference value (15 C°/min). However, the span of the variation is 10 C°, whereas for the first onset the span is only 2.2 C°.
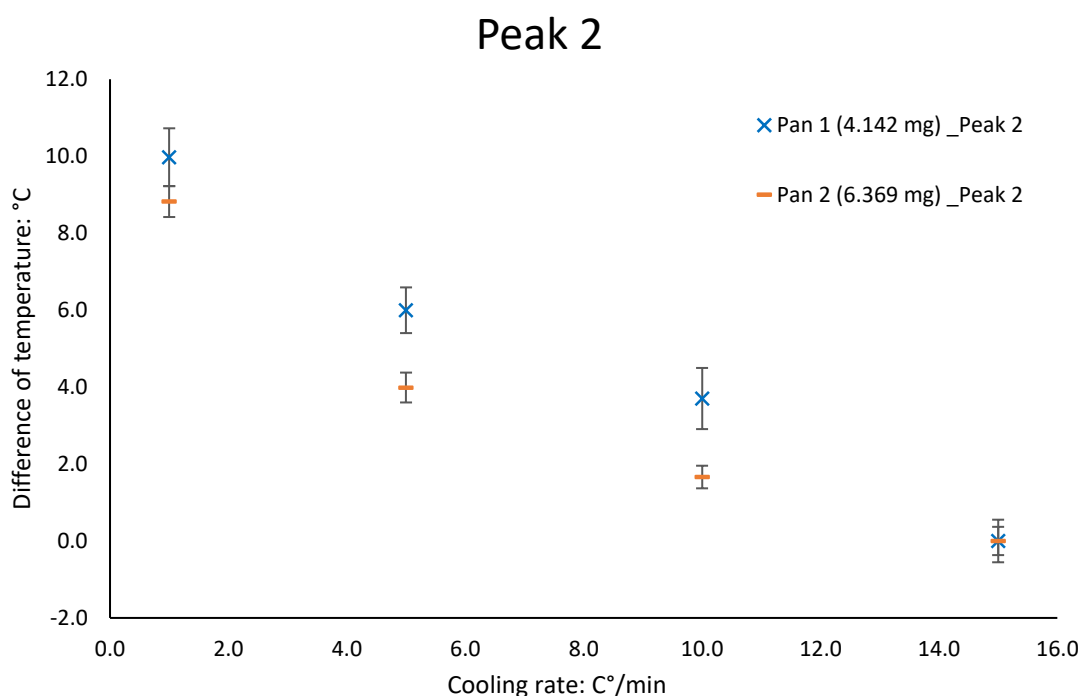
Figure 4.5 Difference between the onset temperatures of Peak 2 at 1, 5 and 10 C°/min and the onset value at 15 C°/min (internal reference for each pan) are plotted as a function of the cooling rates for Pan 1 and Pan 2 separately (no crossing analysis between pans). Error bars are smaller than the symbols in the graph.

Summary

The onset temperature of Peak 1 and Peak 2 decreased as cooling rates increased, in all pans and replicates. As shown in Figure 4.4 and 4.5, for Peak 1 and Peak 2, the difference of onset temperature becomes smaller and closed to the onset value at 15 C°/min when cooling rate increases. The presence of two peaks for tristearin in dodecane solution

contrasts with the single peak observed during crystallization of pure tristearin. In a previous study by Wang (2016), pure tristearin only showed one big broad crystallization peak under a cooling rate of 20 C°/min. The onset temperature of this broad peak was 49.58 °C (Y. Wang, 2016). That onset value was close to the onset of Peak 1 (51.65 ± 0.07 °C). Both of them are lower than the melting point of the α polymorph, 54.1 °C.

The difference between the melting point of α polymorph and the observed onset temperature may be due to the different TAG liquid structures formed in pure SSS and 10% SSS solution. Specifically, in pure SSS, the liquid is made only of the same type of molecules as the crystal network. In the 10% SSS solution, SSS molecules are distributed in the bulk dodecane, forming a diluted solution. SSS molecules may be entangled with dodecane molecules due to the affinity of their aliphatic chains. This affinity would help to disperse the SSS molecules in the dodecane continuum. On the other hand, SSS molecules may also form clusters due to the attraction between their glycerol cores. These cores would form moderately polar regions, in the non-polar sea of aliphatic chains. When the solution is cooled down, SSS molecules need to adapt their liquid structures to crystalize. Thus, for 10% SSS solution, the occurrence of two peaks during crystallization could be explained by a two-step structural change hypothesis. SSS molecules may first form a metastable polymorph, releasing energy. Hence, as indicated in Figure 4.1, a shallow peak, Peak 1, appeared first in the thermogram. After this first step, a structural rearrangement may occur, which shifts toward a more stable polymorph. This rearrangement process is also exothermic. For example, at 1 C°/min, the formation of a more stable polymorph releases 40.20 ± 0.85 °C J/g, which is larger than the 2.92 ± 0.39 J/g of Peak 1 (at 1 C°/min). As shown in Figure 4.1, a sharp-onset and broad-tail peak, Peak 2, appeared later in the thermogram. For pure SSS, a similar exothermic structural conversion from α to β was observed to take place at 55 °C (Nielsen, 2010).

On the other hand, there is also a possibility that SSS molecules formed two different polymorphs but no total conversion between these structures took place. A portion of SSS molecules may first form one metastable polymorphs, which is associated with the shallow Peak 1. The rest of SSS molecules then may crystallize in another polymorphic form, which is associated with the larger Peak 2. These two different structures co-exist and no structure

rearrangement take place during exothermic process. A definite conclusion cannot be made without the data from XRD measurements which helps to identify the structures during the crystallization. However, analysis of the enthalpies can provide additional insight. The clustering hypothesis the initial crystallization happens into the alpha polymorph, in the clusters that already have their TAG molecules very close together, forming an almost "dodecane free" region.

This DSC test provided a thermal reference for selecting the temperature profiles for the polarized light microscopy, rheology, and XRD experiments. From Figure 4.4 and Figure 4.5, it is possible to estimate the highest temperature allowed to ensure that complete crystallization has happened, for a given cooling rate. For example, the maximum cooling rate is 3 C°/min for static XRD. At this cooling rate, the onset temperatures of Peak 1 and Peak 2 are approximately 51 °C and 38 °C. In order not to exceed the upper limit, a lower temperature, 35 °C was set as the maximum crystallization temperature. 35°C was chosen to keep consistent in setting the other crystallization temperature in the order of multiple five.

4.1.2   Melting-dissolution Temperature
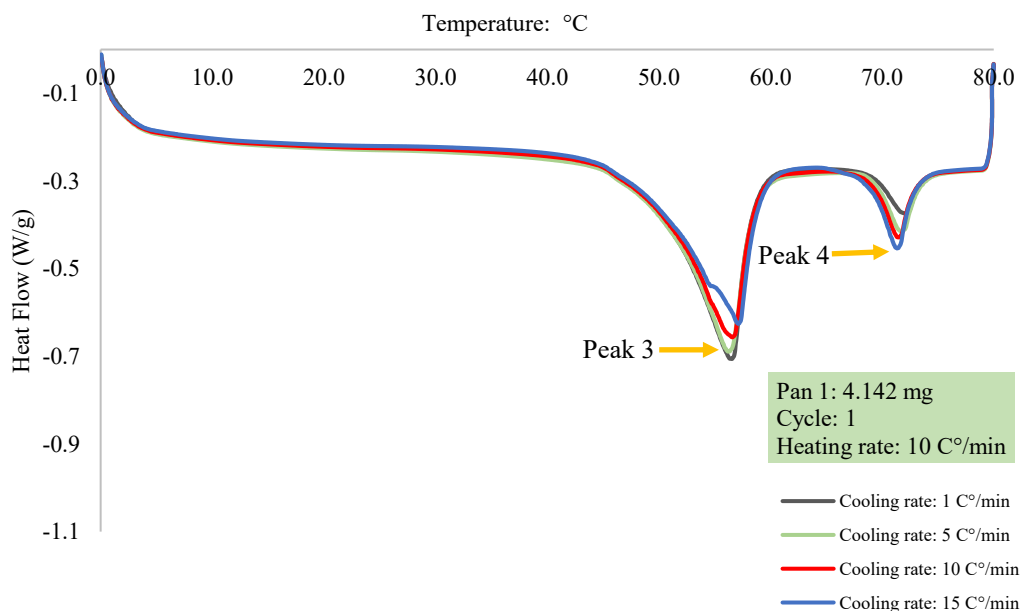
a.
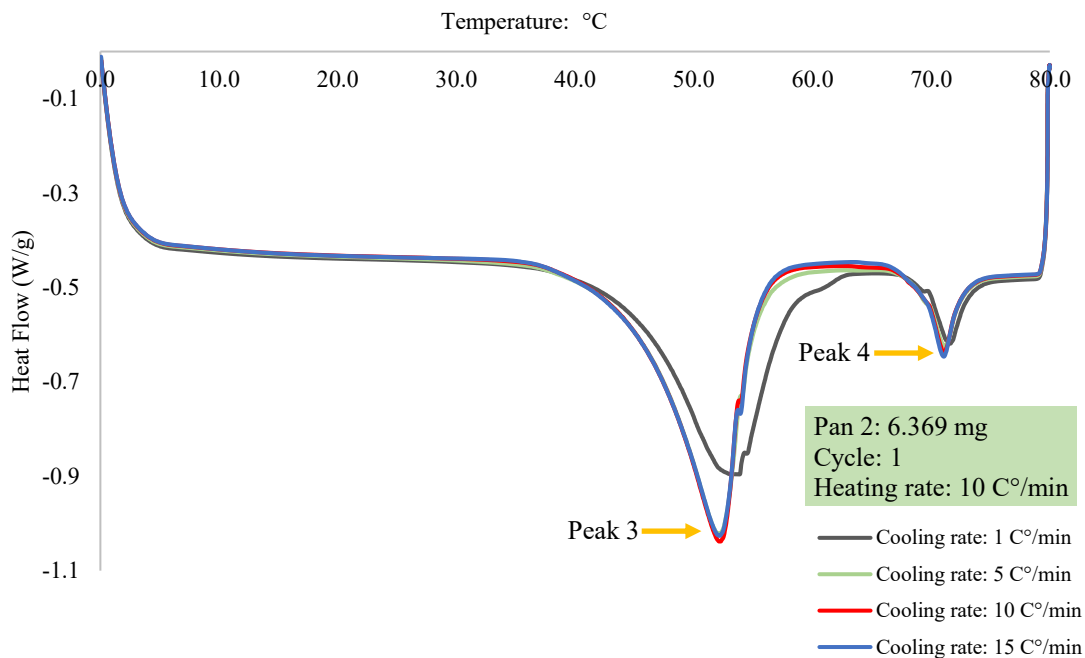
b.

Figure 4.6 (a) An example of analysis of the onset temperature for Peak 3 and Peak 4 of 10% SSS solution (under the same cycle 1) for Pan 1 (4.142 mg). (b) An example of analysis of the onset temperature for Peak 3 and Peak 4 of 10% SSS solution (under the same cycle 1) for Pan 2 (6.369 mg).

After being kept isothermally at 0 °C for 10 min, the sample was then heated up to 70 °C at 10 C°/min. As shown in Figure 4.6, Peak 3 and Peak 4 are produced by an endothermic event during the heating step. Peak 3 is a group of peaks overlaid together. The onset temperature of Peak 3 is 44. 81 ± 0.09 °C), which is lower than the melting point of 53.24°C (Literature m.p. is 54.3 °C, (Wesdorp)) from a previous study of pure SSS (α polymorph) by Wang (2016). For Peak 4, the onset temperature is hard to calculate accurately due to the influence of Peak 3. The onset value of Peak 4 is around 69 °C, which is lower than the melting point of pure SSS in β polymorph (72.5 °C) (Lavigne et al., 1993).

For 10% SSS solution, the appearance of Peak 3 and Peak 4 may be explained by the coexistence of two different structures. Additional XRD experiments are necessary to identify the possible structures that are associated with these two peaks.

This DSC test provided a thermal reference for selecting the conditioning temperature for

the polarized light microscopy, rheology, and XRD experiments. For static XRD experiments, the conditioning temperature is set at 70 °C, which is lower than 80 °C that is recommended for pure TAGs and TAG mixtures (Marangoni & Wesdorp, 2013). The lower conditioning temperature is chosen to minimize the evaporation of dodecane. For experiments under shear flow, the applied shear enhances the mass and heat transfer. The onset temperature of melting takes place at a lower temperature (depends on shear rate) compared to static condition (e.g., the onset temperature of melting was observed around 54 °C at 0.9 s^{-1} in PLM test). Hence, for experiments under shear flow, the conditioning temperature was set at 60 °C to protect the volatile solvent.

4.2 RHEOLOGY

The 10% SSS suspension was first melted (step a) and then cooled down to the selected crystallization temperature (*i.e.,* 35, 28, 20, 12, 5, 0, -5 °C). Before shear step **d**, a pre-shear oscillatory step **c** (200 s) was performed to measure the primary structure of 10% SSS suspension after cooling step b. In the following step **d**, the sample was sheared at the selected shear rate (0.9, 9, 90, 900 s^{-1}, ideal estimate for Newtonian) for 1200 s. A subsequent after-shear oscillatory step e was applied for 200 s. Each experiment is replicated three times and the average values are discussed in the following sections.

4.2.1 Apparent viscosity after initial crystallization

First, we discuss the behaviour of apparent viscosity (η) with respect to time within each shear rate group, as a function of temperature (horizontal analysis). The average values of η (after 1000 s) are plotted in Figure 4.10.

4.2.1.1 Apparent viscosity: 0.9 s^{-1} in step d

The data for η with respect to time under a shear rate of 0.9 s^{-1}are shown in Figure 4.7 (a). The applied shear 0.9 s^{-1} caused a dramatic reduction in η in the first 200 s compared to its initial value, except for the 28 and 35 °C data. Notice how in Fig 4.7 (a), after 200 s, η slightly fluctuated until the end of step d. At 28 °C, η decreased rapidly in the first 200 s, as in in other temperatures, but then increased slowly for the rest of step d. At 35 °C, η exhibited a slow increasing pattern through the whole step **d**.

At the end of step d, among different temperature groups, the final value of η slightly decreased as temperature dropped down except the 28 °C data. For 28 °C, η obtained the largest value among the all temperature data

In the first 200 s, the applied shear 0.9 s^{-1} caused a reduction in η, which may indicate a breakdown of the previous structure formed in step c. As shown in Figure 4.7 (a), a periodical pattern was present in all temperature groups. There are two possible explanations for this fluctuation behavior. First, the periodical curve may indicate oscillations growing with time and scaling with the rotation period of the rheometer. According to Tarabukina, Jego, Haudin, Navard, & Peuvrel-Disdier (2009), at low shear rates, these oscillations may arise due to the formation of a fat network and subsequent phase rearrangements under shear, which leads to more compact zones and releases interstitial liquid. This process results in the network rupture. And these oscillation network formations will be prevented at high shear rates (Tarabukina, Jego, Haudin, Navard, & Peuvrel-Disdier, 2009). On the other hand, the fluctuation may be an artifact of the rheometer under small shear rate (0.9 s^{-1}). In this experiment, our sample is a diluted solution rather than a viscous TAG mixture. Therefore, the oscillation network formation may not likely occur in 10% SSS suspension. The periodical curve is most likely caused by the limitation of AR-2000 under small shear rate.

4.2.1.1   Apparent Viscosity: 9 s^{-1} in step d

The data for η with respect to time under a shear rate of 9 s^{-1} are shown in Figure 4.7 (b). The applied shear 9 s^{-1} caused a two step pattern in η except for the 35 °C data. η increased rapidly in the first 400 s compared to its initial value and then grew slowly during the rest of step d. At 35 °C, η increased slowly during the whole step d. At the end of step d, among different temperature groups, η increased as temperature dropped down except the 28 °C data (*i.e., η* obtained the highest value at 28 °C among the 5, 12, 20 and 35 °C data).

4.2.1.2   Apparent Viscosity: 90 s^{-1} in step d

The data for η with respect to time under a shear rate of 90 s^{-1} are shown in Figure 4.7 (c). The applied shear 90 s^{-1} caused a dramatic increase in the first 200 s in η compared to its initial value and then slightly decreased through the rest of step d except for the 35 °C data. At 35 °C, η kept increasing slowly during the whole step d. At the end of step d, among

different temperature groups, η increased as temperature dropped down.

4.2.1.1 Apparent viscosity: 900 s⁻¹ in step d

The data for $\pmb{\eta}$ with respect to time under a shear rate of 900 s^{-1} are shown in Figure 4.7 (d). The applied shear 900 s^{-1} caused a slight reduction in $\pmb{\eta}$ compared to its initial value except the 35 °C data. At 35 °C, $\pmb{\eta}$ started to increase dramatically in the first 200 s compared to its initial value and then slow decreased through the rest of step d. At the end of step d, among different temperature groups, $\pmb{\eta}$ increased as temperature dropped down except for the 35 °C data. At 35 °C, $\pmb{\eta}$ reached the maximum value among the all temperature group.

$\pmb{\eta}$ almost kept constant under the shear rate 900 s^{-1} (except for the 35 °C data). One possible explanation is the strongest shear force produced by the applied shear 900 s^{-1}. The structure changes may take place so fast that rheometer cannot record them and then only exhibits the steady state value of $\pmb{\eta}$.
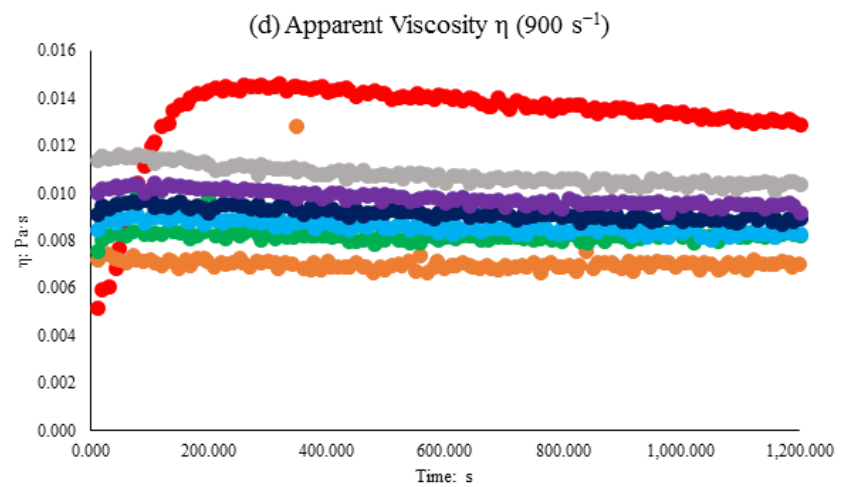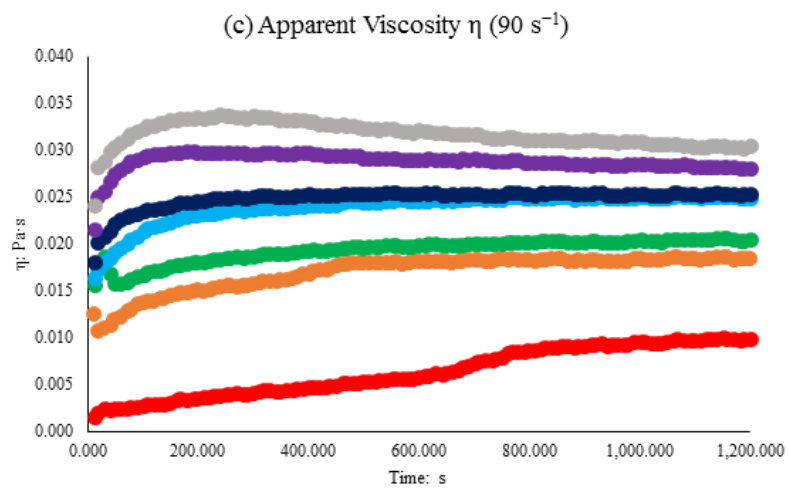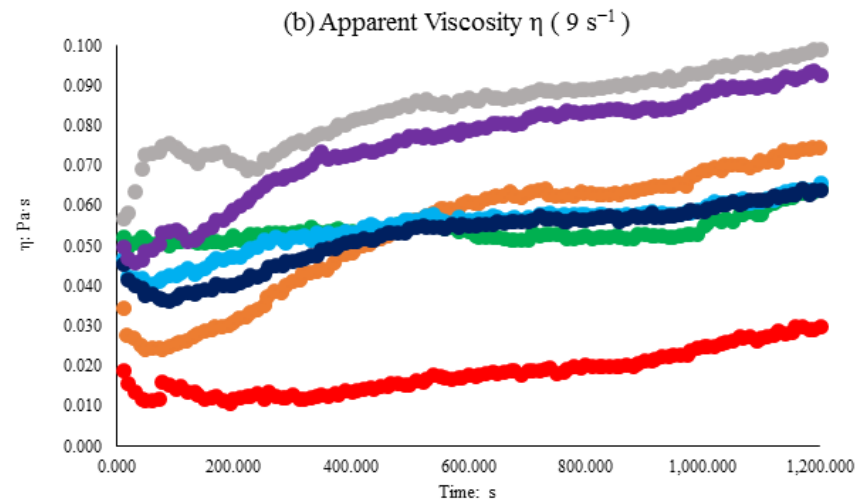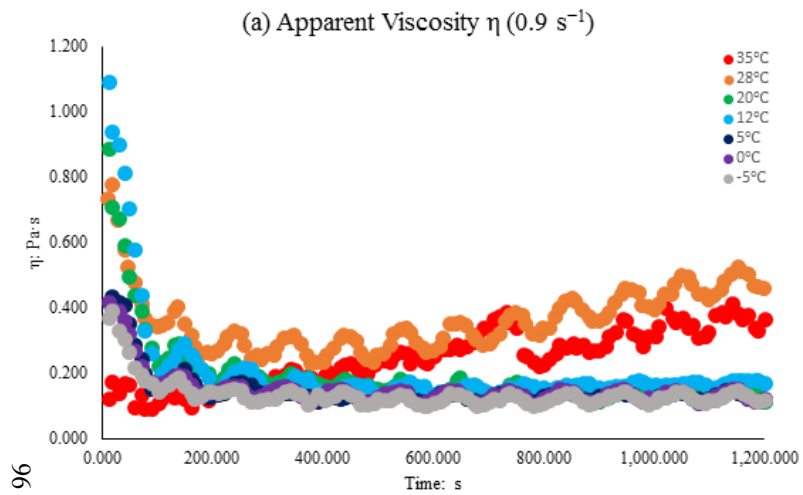
Figure 4.7 Apparent viscosity as a function of time (step d), for shear rates (a) 0.9 s^{-1}, (b) 9 s^{-1}, (c) 90 s^{-1}, (d) 900 s^{-1}.

4.2.2 Complex viscosity before and after application of shear

First, we discuss the behaviour of complex viscosity (η^*) with respect to time within each shear rate group, as a function of temperature (horizontal analysis) in step c (*pre-shear oscillatory*) and step e (*after-shear oscillatory*).

As shown in Figure 4.8 and Figure 4.9, in step c, the applied shear (0.9, 9, 90 and 900 s^{-1}) caused a reduction in η^* compared to its initial value and then kept almost constant during the rest of time except for the 35 and 28 °C data. At 28 and 35 °C, η^* slightly increased during step c. At the end of step c, among different temperature groups, η^* decreased as temperature dropped down except for the 35 and 28 °C data (i.e., η^* obtained the smallest value at 35 and 28 °C among all data). The values of η^* at the end of step c and e are plotted in Figure 4.10.
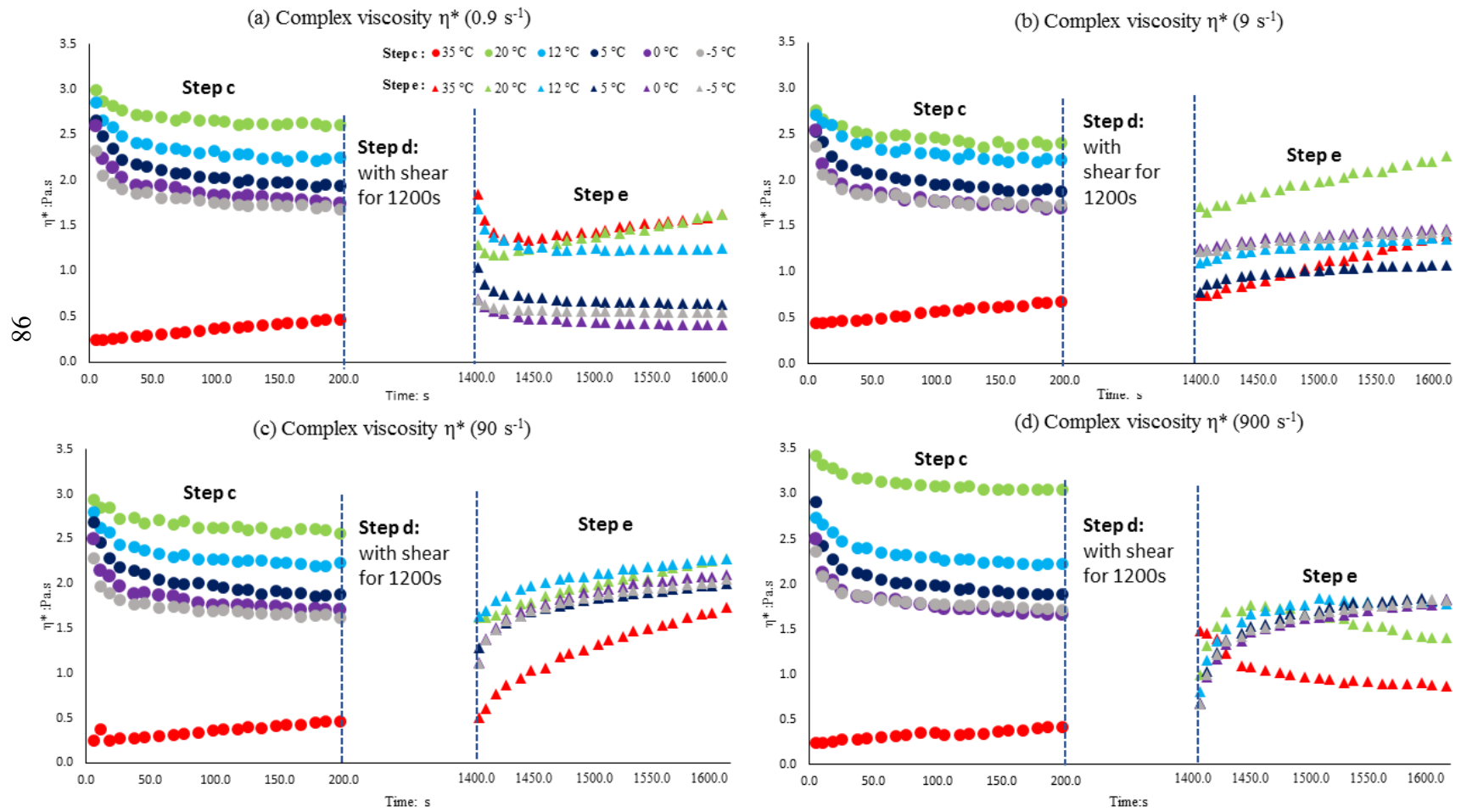
Figure 4.8 Complex viscosity η* as a function of time, for shear rates (a) 0.9 s⁻¹, (b) 9 s⁻¹, (c) 90 s⁻¹, (d) 900 s⁻¹. The data for 28 °C are plotted separately.
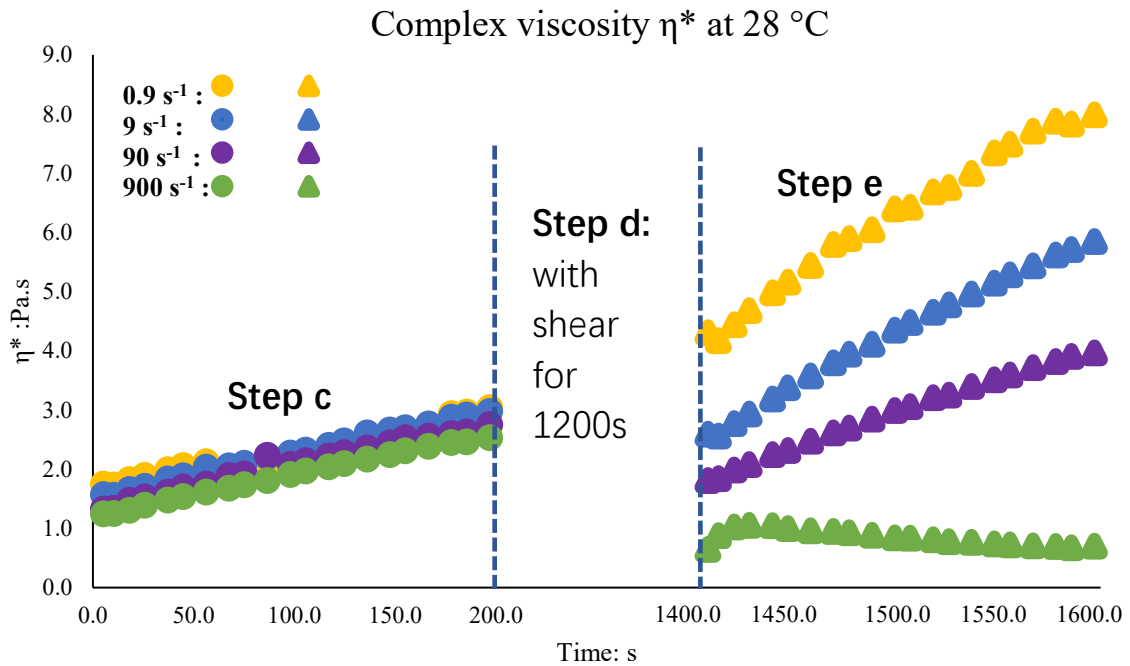
Figure 4.9 Complex viscosity η* as a function of time for 28 °C, including all shear rates.

4.2.2.1 Complex viscosity: 0.9 s⁻¹

In step e, the data for $\boldsymbol{\eta^*}$ with respect to time under a shear rate of 0.9 s^{-1} are shown in Figure 4.8 (a) and Figure 4.9. $\boldsymbol{\eta^*}$ begun to decrease rapidly in the first 50 s compared to its initial value (lower than the end value of step c) and then kept almost constant during the rest of time except for the 35, 28 and 20 °C data. At 35 and 20 °C, after the first 50 s, $\boldsymbol{\eta^*}$ slightly increased during the rest of step e. At 28 °C, $\boldsymbol{\eta^*}$ kept increasing during the whole step e.

At the end of step e, among different temperature groups, $\boldsymbol{\eta^*}$ decreased as temperature dropped down (smaller than its end value of step c) except for the 28 °C data (i.e., $\boldsymbol{\eta^*}$ obtained the maximum value at 28 °C among all the temperature groups).

4.2.2.2 Complex viscosity: 9 s⁻¹

In step e, the data for $\boldsymbol{\eta^*}$ with respect to time under a shear rate of 9 s^{-1} are shown in Figure 4.8 (b) and Figure 4.9, the applied shear caused an slight increase in $\boldsymbol{\eta^*}$ except for the 35, 28 and 20 °C data. At 35, 20 and 28 °C, $\boldsymbol{\eta^*}$ exhibited an fast growth rate.

At the end of step e, among different temperature groups, $\boldsymbol{\eta^*}$ decreased as temperature

dropped down except for the 35 °C data (i.e., at 35 °C, η^* is smaller than the value at 20 and 12 °C data).

4.2.2.3   Complex viscosity: 90 s⁻¹

In step e, the data for η^* with respect to time under a shear rate of 90 s^{-1} are shown in Figure 4.8 (c) and Figure 4.9, the applied shear caused an increase in η^*. A slowly increasing pattern was observed at 35 °C.

At the end of step e, among different temperature groups, η^* decreased as temperature dropped down except for the 35 °C data (*i.e.,* at 35 °C, η^* is smallest among all the temperature groups).

4.2.2.4   Complex viscosity: 900 s⁻¹

In step e, the data for η^* with respect to time under a shear rate of 900 s^{-1} are shown in Figure 4.8 (d) and Figure 4.9, the applied shear caused a rapid increase in η^* in the first 150 s and then kept almost constant during the rest of step except for the 35 °C data. A slowly decreasing pattern was observed at 35 °C.

At the end of step e, among different temperature groups, η^* decreased as temperature dropped down except for the 35 and 28 °C data. (*i.e.,* at 35 °C, η^* is smallest among all the temperature groups).

4.2.3   Summary

The influences of different shear rates (0.9, 9, 90 and 900 s^{-1}) and temperatures (-5, 0, 5, 12, 20, 28 and 35 °C) on 10% SSS solution are shown in Figure 4.10 and Figure 4.11.

In Figure 4.10 (a) and (b), $\eta_{average}$ (from 1000 s to 1200 s) is plotted as a function of temperature and shear rate separately. Under the same temperature, $\eta_{average}$ decreased as shear rate increased. From -5 to 35 °C, $\eta_{average}$ showed different changing trends: at the lowe shear rate (0.9 s^{-1}), $\eta_{average}$ increased slightly as temperature increased; at the medim shear rate (9 s^{-1}), $\eta_{average}$ gradually decreased as temperature decreased; at the highest shear rate (90 and 900 s^{-1}), n kept almost constant regardless of temperature. This different pattern in $\eta_{average}$ at 0.9 s^{-1} may be due to an artifact of the rheometer under small shear rate.

There is a possibility that a critical shear rate exists between 90 s^{-1} and 900 s^{-1}. Below this

critical shear rate, the applied shear may enhance the crystallization of SSS in suspension and leaves a harder structure in step e (*e.g.,* $\eta^*_{90\ s-1} > \eta^*_{9\ s-1} > \eta^*_{0.9\ s-1}$). Once exceeds this critical value, the applied shear may weaken the crystallization of SSS in suspension and result in a softer structure in step e (*e.g.,* $\eta^*_{90\ s-1} > \eta^*_{900\ s-1}$). A definite conclusion cannot be made without the data from XRD measurements under the same conditions.

In Figure 4.10 (c) and (d), at the end of step e (*after-shear oscillatory*), $\eta^*_{average}$ (from 1550 s to 1600 s) is plotted as a function of temperature and shear rate separately. $\eta^*_{average}$ showed a two-step pattern (except for the 0.9 s^{-1} group), where $\eta^*_{average}$ increased as temperature increased from -5 to 20 °C and then decreases as temperature increased up to 35 °C. $\eta^*_{average}$ reached the maximum value at 20 °C while obtained the minimum value at 35 °C. At 0.9 s^{-1}, $\eta^*_{average}$ slowly increased during the whole step e. The fluctuation of data may be an artifact of the rheometer.

In Figure 4.10 (e) and (f), at the end of step c (*before-shear oscillatory*), $\eta^*_{average}$ (from 150 s to 200 s) is plotted as a function of temperature and shear rate separately. $\eta^*_{average}$ showed a two-step pattern, where $\eta^*_{average}$ increased as temperature increased from -5 to 20 °C and then decreased as temperature increased up to 35 °C. $\eta^*_{average}$ reached the maximum value at 20 °C while obtained the minimum value at 35 °C.

In Figure 4.11 (a) and (b), $\eta_{average}$ is plotted as a function shear rate in a log-log scale graph. Most of data (from 28 to -5 °C) followed a linear trend, which can be explained by the power law model. The k and n value calculated from the fittings showed that 10% SSS suspension is a shear thinning material. At 35 °C, the scattering data of $\eta_{average}$ resulted in a poor fitting of pow law model, which needs further investigations. In Figure 4.11 (b), η/η_0 is plotted as a function shear rate in a log-log scale graph. Although η_0 (dodecane) decreased as temperature increased, the values of η/η_0 followed the similar trend in Figure 4.11 (a). The change of η_0 did not influence η significantly.

(a) Apparent Viscosity (average)

(b) Apparent Viscosity (average)

(c) Complex viscosity (average) at step e

(b) Complex viscosity (average) at step e

the data at 28 °C for shear rate 0.9/9/90 s^-1 were not plotted
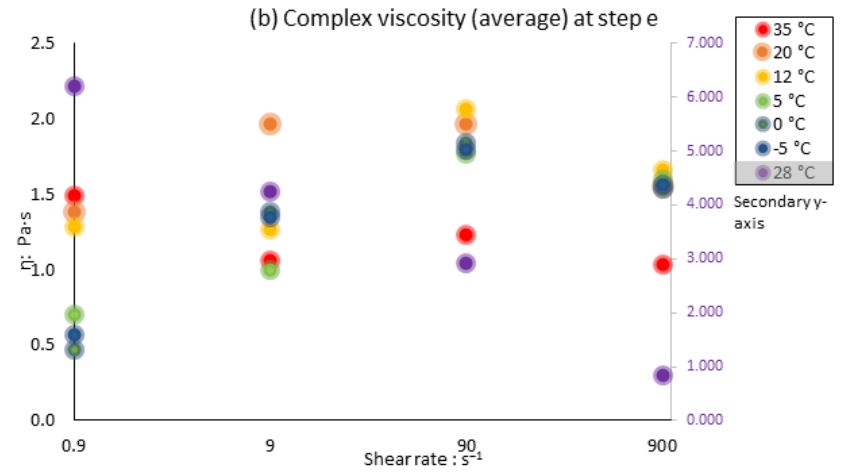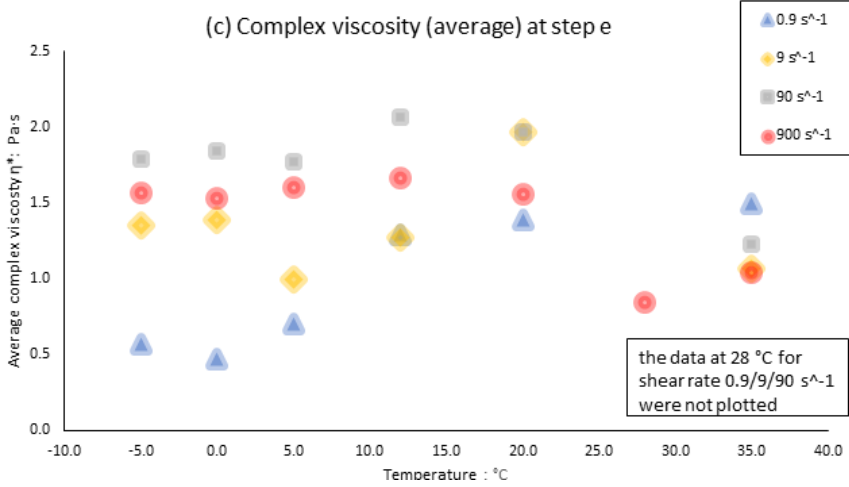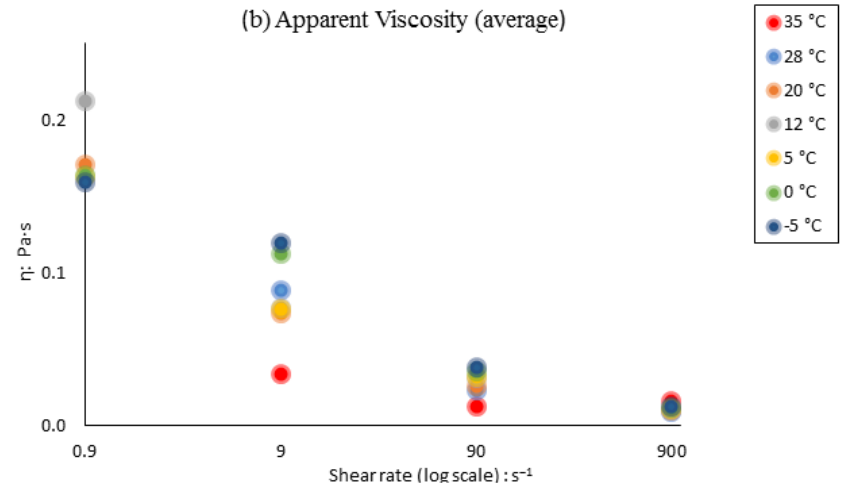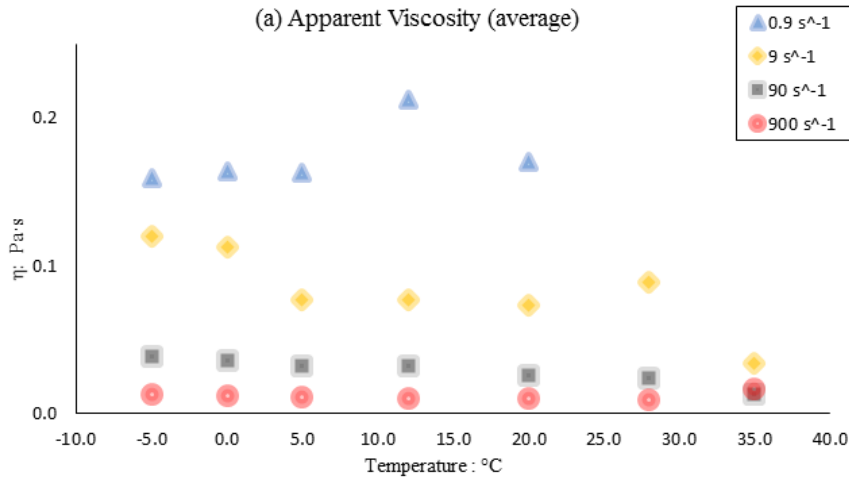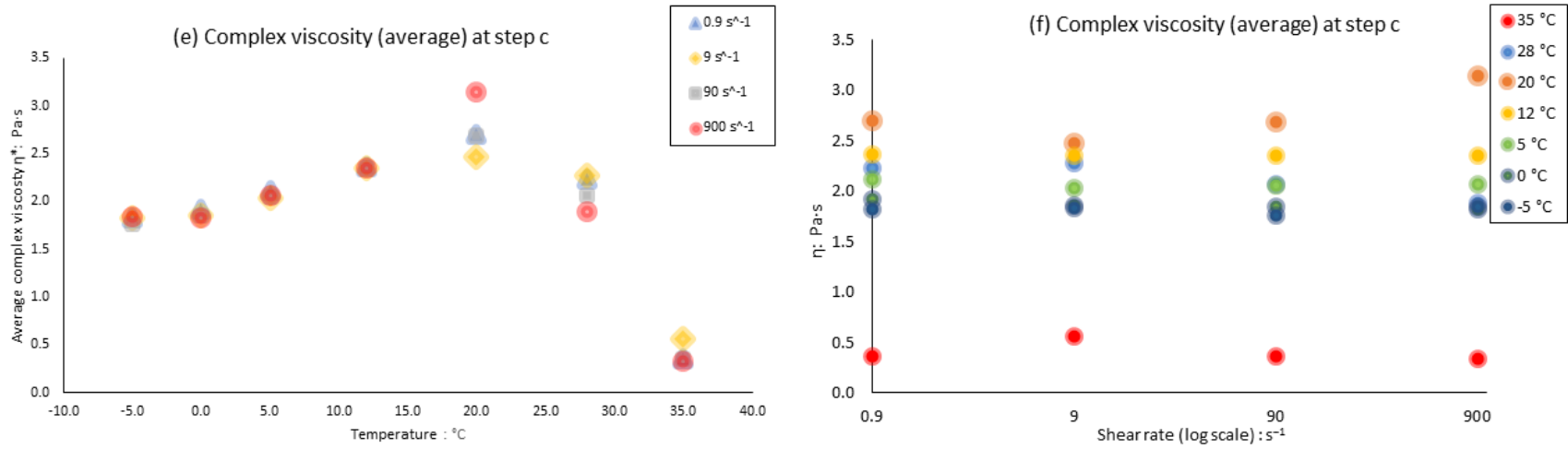
Figure 4.10 (a) A plot of average apparent viscosity versus temperature (after 1000 s) (b) A plot of average apparent viscosity versus shear rate (after 1000 s). (c) A plot of average complex viscosity versus temperature in **step e**. (d) A plot of average complex viscosity versus shear rate in **step e**. (d) A plot of average complex viscosity versus temperature in **step c**. (e) A plot of average complex viscosity versus shear rate in **step c**.
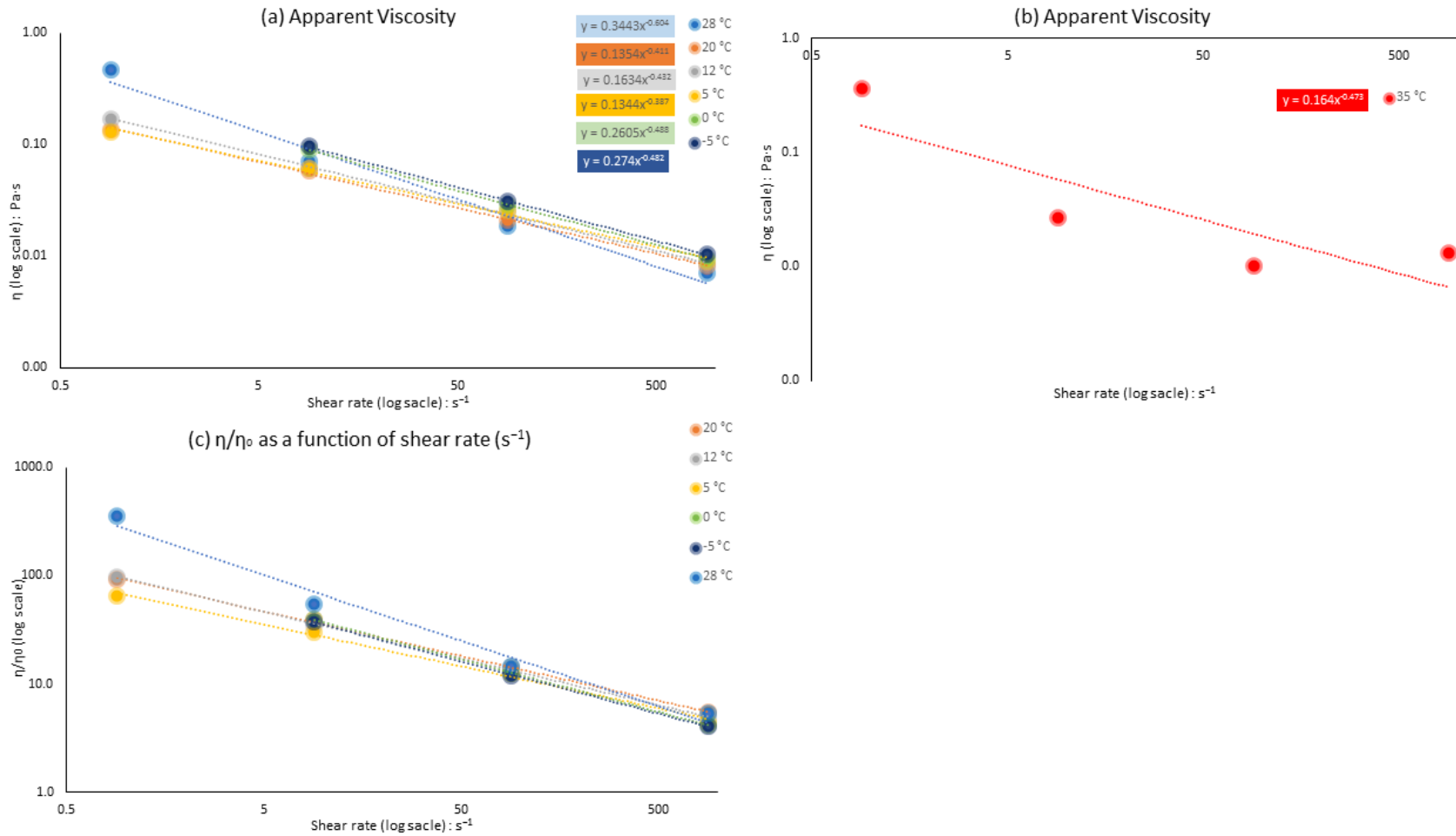
Figure 4.11(a) A log–log plot of average apparent viscosity versus shear rate (after 1000 s) at 28,20, 12, 5,0, and -5 °C. At -5 °C, the data at 0.9 s⁻¹ was not plotted. (b) A log–log plot of average apparent viscosity versus shear rate (after 1000 s) at 35 °C. (c) A log–log plot of η/η_0 as a function of shear rate at at 28,20, 12, 5,0, and -5 °C. At -5 °C, the data at 0.9 s⁻¹ was not plotted.

The influence of the applied shear on SSS crystal structure is shown in Figure 4.12 with the data at 5°C. In step c, η^* decreased slow and reached a stead end value. After shear, the value of η^* changed in different patterns: after the applied shear of 0.9 s^{-1}, η^* decreased rapidly in the first 50s and kept almost constant during the rest of time; after the applied shear of 9, 90 and 900 s^{-1}, η^* increased rapidly in the first 50s and kept almost constant during the rest of time. However, the end of step d, η^* are closed to the end value last step c in the 90 and 900 s^{-1} data.
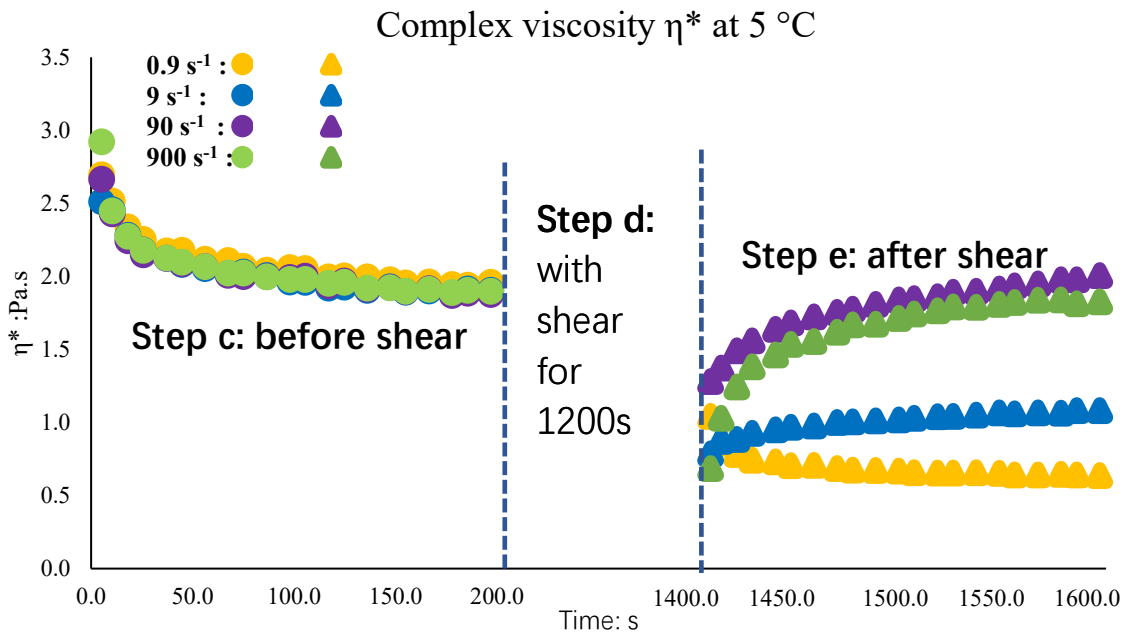
Figure 4.12 Complex viscosity η* as a function of time for 5 °C, including all shear rates.

4.3 PLM

Polarized light microscopy (PLM) was used to look at the microstructural development under shear flow (corresponding to the shear step d in the rheology measurements).

4.3.1 Morphology

After cooling down to the selected crystallization temperature, 600 s of a constant shear was applied to the sample. Figure 4.13 and 4.14 show clusters of crystals crystallized under static and shear (0.9 s^{-1}) condition at 35 °C. In Figure 4.13, optically detectable cluster was observed after approximately 1 min, where a large cluster of crystals appeared within the dark liquid background. At 2 min, the amounts of clusters had increased. Some of the

clusters began to grow into a spherulitic shape. At 3 min, the number of clusters had increased slightly. The shapes of these clusters of crystals were developed in different ways in 3 mins. In the rest of experiment, most of the clusters developed into a spherulitic morphology and some clusters had been attracted to each other. According to Sonwai & Mackley (2006), van der Waals forces are presumed to lead to some forms of aggregation, which readily occurred as soon as the fat clusters attained a certain minimum size (Sonwai & Mackley, 2006).
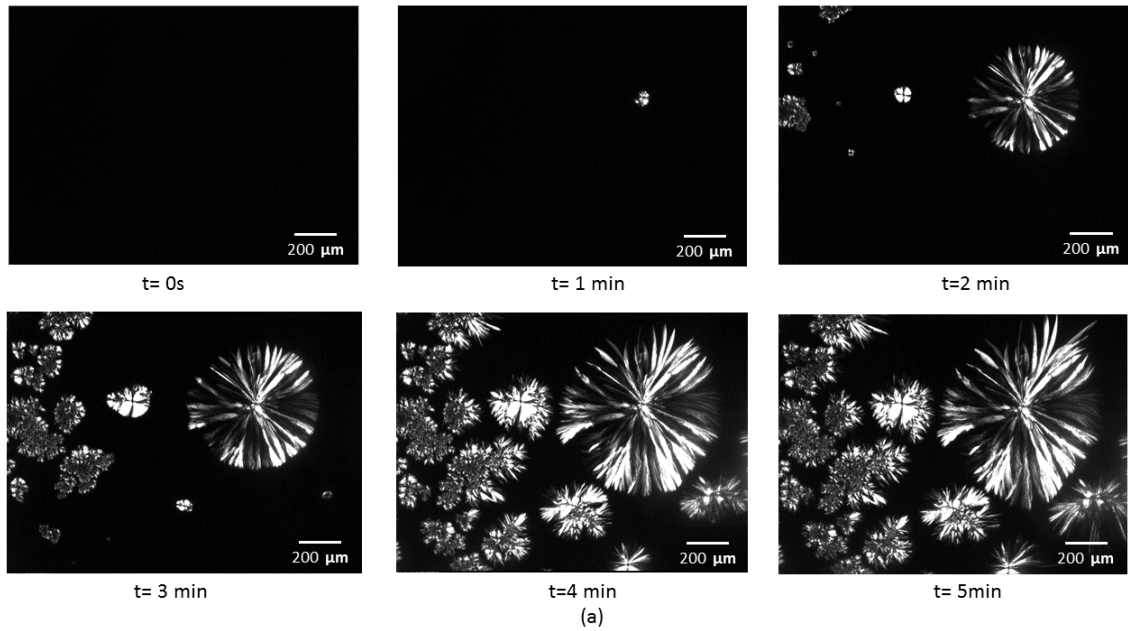
Figure 4.13 PLM images of 10% SSS solution at 35 °C immediately after a cooling step (horizontally: 0,1,2,3,4 and 5 min) in static condition.

The shapes of clusters of SSS crystals formed at a low shear rate of 0.9 s^{-1} is shown in Figure 4.14. This low shear rate significantly changed the morphology of clusters. The first optically detectable cluster was observed within 10 s. The number of clusters increased as time elapsed. Some of the clusters exhibited a mixed morphology (needle-like structure and platelets).

The applied shear seems to prevent the formation of large spherulites to some extent. Some clusters are forced to exist as small fragments. These little clusters may be broken pieces formed by collisions among the big spherulites under shear. In this experiment, clusters of SSS crystals started aggregation after 20 s. Between 30 s and 50 s, there were no significant

changes in size of these clusters of SSS crystals. At 50 s, the size of the largest cluster was obviously smaller than the largest cluster in the static experiment at the same crystallization temperature. Besides, there were more aggregations of clusters than the static experiment.

A low shear rate can increase the chances of SSS molecules in the solution to contact each other and integrate into the crystal surface. Besides, a low shear rate can increase the possibility of small clusters of SSS meeting one another and forming larger clusters. The applied shear can also facilitate the heat transfer and then prevent the inhomogeneous and instable temperature distribution in suspension.
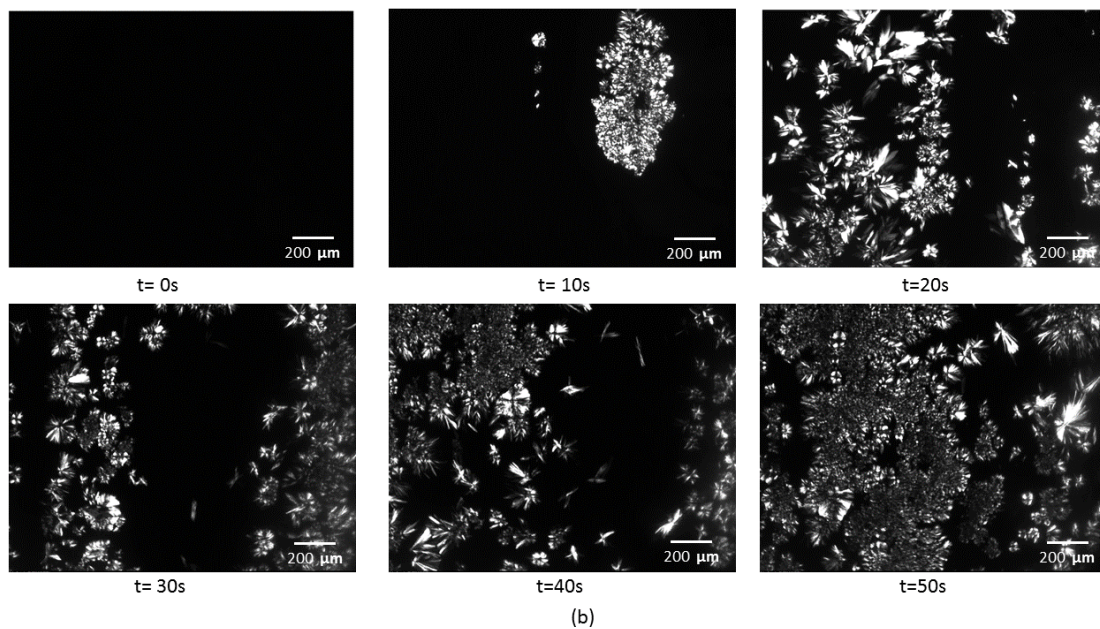
Figure 4.14 PLM images of 10% SSS suspension at 35 °C immediately after the cooling step b at a shear rate of 0.9 s⁻¹ (images were taken at 10 s interval).

The shape and structure of clusters of SSS crystals under shear flow (0.9 s^{-1}) were quite different from the one under static condition. The presence of more crystalline material immediately after the shear step indicates that shear enhanced the crystallization process. Under static conditions, the sample crystallized on and in between the cluster, resulting in larger aggregates. A shear of 0.9 s^{-1} resulted in a large number of compact clusters. Small aggregations and network formations took place during the shear step. According to Kaufmann, Graef, Dewettinck, & Wiking (2012), the network structure under the shear condition is different from the structure under static condition. The latter is firmer with the

107

formation of solid bridges between existing crystal structures (Kaufmann et al., 2012).

However, the polymorphic structure and phase transition of the sample crystallized in the CSS450 cannot be determined without XRD data. In this research, the imaging of SSS crystallized under higher shear rates and crystallization temperatures is problematic. The non-repeatable behaviors of clusters of SSS crystals will be discussed in the next part.

4.3.2 Early crystal growth

PLM is a well-developed technique for the image analysis of the microstructure of fat crystal networks. PLM allows us to estimate the time (τ_c) that is required for crystals to reach the critical size and be visible under microscopy. After obtaining images, a procedure of thresholding was done to convert the acquired grayscale images (*i.e.,* images that consist of a broad range of gray tones that go from pure white to pure black) to binary images (*i.e.,* images that are merely in black and white). This procedure can help to separate clusters of SSS crystals and background.

Figure 4.15 shows an example of thresholded images of polarized light micrographs under 35°C with shear 9 s^{-1}. In these three replicates, the first cluster of SSS crystals was observed at different times. This non-repeatable behavior also took place among other replicates at higher shear rates. In some replicates, there was even no clusters observed during the whole experiment. On the other hand, when clusters were observed among replicates, the shape and size of clusters were different as shown in Figure 4.15 (e), (g), and (n). Replicate 1 exhibited a mixed morphology of spherulites and needle-like clusters. Replicate 2 showed a sand-like structure with much smaller spherulites. For replicate 3, clusters exhibited a rhomb-like structure.

Replicate 01   Replicate 02   Replicate 03

(a) t=0s   (f) t=0s   (k) t=0s
(b) t=2s   (g) t=2s   (l) t=2s
(c) t=4s   (h) t=4s   (c) t=4s
(d) t=6s   (i) t=6s   (m) t=6s
(e) t=8s   (g) t=8s   (n) t=8s

200 μm
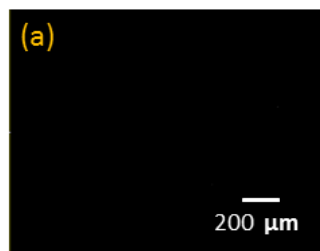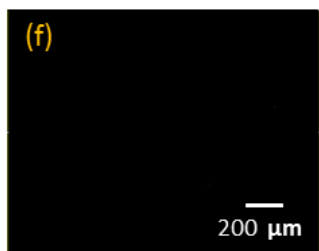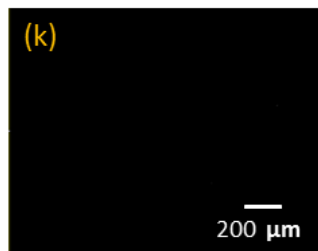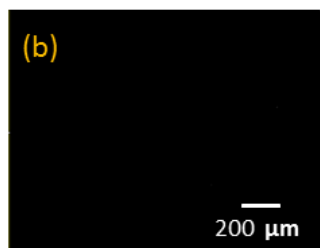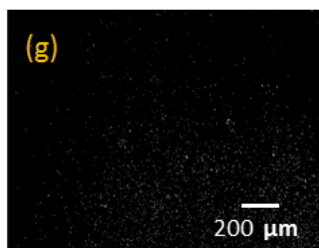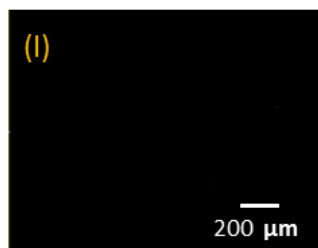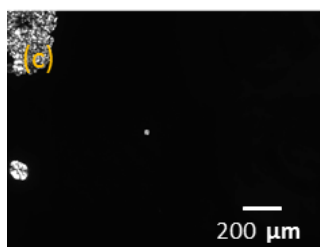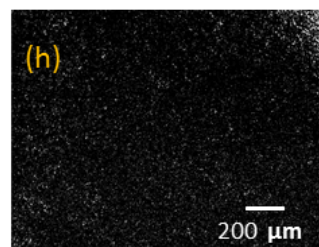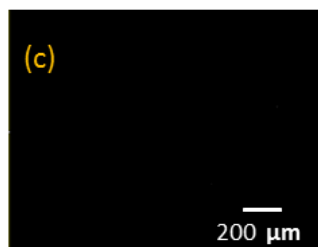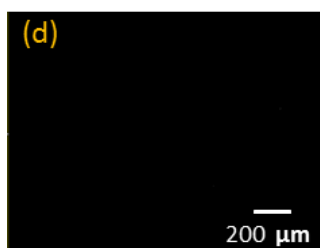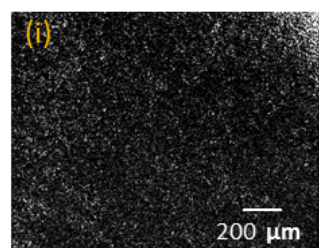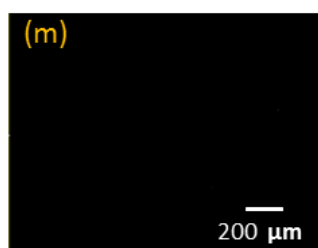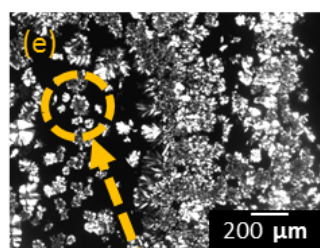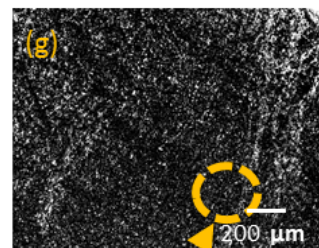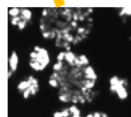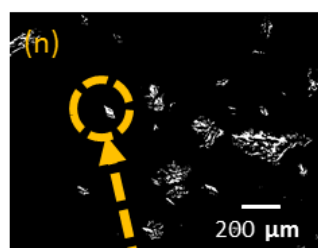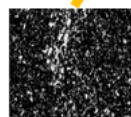
Figure 4.15 An illustration of thresholded images of polarized light micrographs under 35°C with shear 9 s^{-1}. Three replicates are chosen to show the low repeatability of τ_c and crystal morphology (Replicate: (a) to (e), Replicate 2: (f) to (g), Replicate 3: (h) to (n)).

There are several possible explanations for these phenomena. The crystallization of SSS out of solution may take place before the start of step c. Ideally, the step b (cooling step) should be an instantaneous step where temperature drops down to the designed temperature instantaneously. In fact, it took approximate 1.7 mins to lower temperature from 60 °C to 35 °C during step b (cooling rate: 15 C°/min). Nuclei may appear earlier then we expected during this cooling period. Moreover, these nuclei can act as crystallization sites for secondary nucleation, where new clusters form on contact with existing nuclei, or crystal fragments. The secondary nucleation will happen once the primary nucleation has occurred. Hence, the crystallization of SSS can occur earlier before step c due to the induction by some earlier formed nuclei in the cooling step b. In other words, the time zero we set may not really match the actual start point of crystallization of SSS, which may explain the low repeatability among the replicates.

Another possible explanation is the limitation of relatively small observation area of the lid of CSS 450 stage, as shown in Figure 4.16 (a). The area of window is 6.15 mm^2. When the sample is loaded on the bottom plate, the effective observation area is equivalent to a 57 mm^2 ring per turn during shear measurements (*i.e.,* an orange area in Figure 4.16 (b)). If considering that the 1600x1200 field of view was the only one being recorded, the size of filed of view is 1.2 x 0.9 mm. This ring takes up less than 8% of total area of the whole quartz plate per turn during shear tests. The images obtained from the small observation area may not really capture the first optical cluster of SSS crystals. The nucleation may already occur outside of the ring. Hence, the time zero we set may not really match the actual start point of crystallization of SSS. The time we recorded should be a sum of two terms: the time of the first optical cluster appeared and the time of this cluster diffused to the observation area. On the other hand, in this research, 10% SSS solution is a dilute sample, which means the possibility of observing an SSS crystal in the ring area is much lower than pure SSS. Thus, the second term, diffusion time, cannot be ignored.
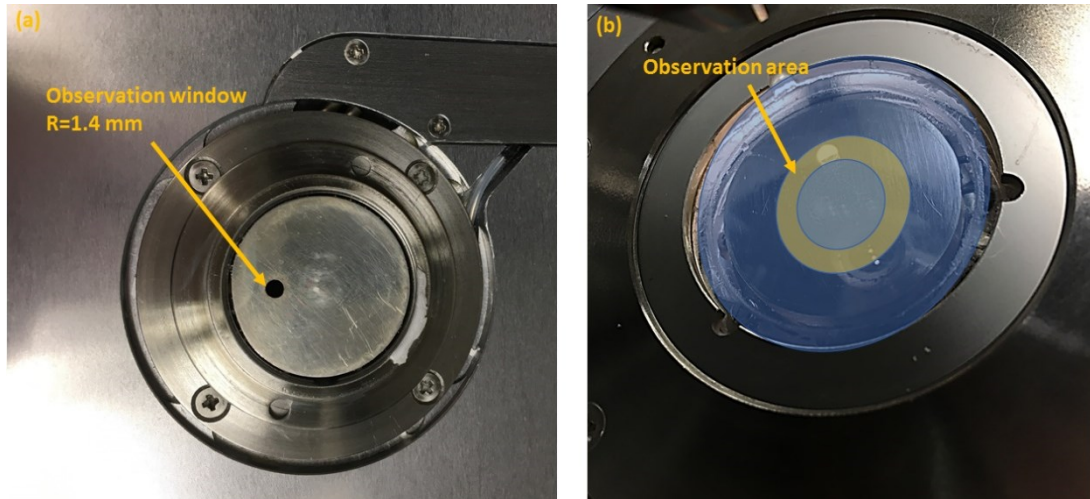
Figure 4.16 (a) The configuration of the quartz plate on the lid. (b) The configuration of the quartz plate on the bottom plate.

As shown in Figure 4.17, from 0 to 4s, the clusters of SSS crystals "ring" shrank quickly from the outer edge to the centre of the quartz plate. This phenomenon was observed by opening the lid right after cooling the sample down to 35 °C. The crystallization of SSS may first occur at the outer edge of quartz circle plate and move towards the centre. In this case, the τ_c is the sum of two terms, nucleation time (*i.e.,* the time needed to form the first crystal) and diffusion time (*i.e.,* the time needed for the first cluster of SSS crystals diffused into the observation area and be captured by the camera). The non-repeatable data for τ_c can be explained by the difference in the diffusion time and difference of the possibility of a cluster of SSS crystals first captured by the camera.

<div align="center">t=0s   t=2s   t=4s</div>

Figure 4.17 The movement of SSS molecules on the quartz plate on the bottom plate

4.4 XRD

Tristearin (SSS) can form three different polymorphic forms, α, β′, and β. The form α is arranged in a hexagonal chain packing and characterized by a short spacing from 4.1 to 4.2 Å. The β' from is arranged in an orthorhombic chain packing and identified by a short spacing at 4.2 and 3.8 Å. The β form is arranged in a triclinic chain packing with a strong reflection at 4.6 Å, and the other two strong peaks at 3.85 Å and 3.7 Å (Table 4.1).

	Tmelting (°C)	short spacings (Å)	long spacings (Å)
α	54,5	4,1-4,2	50,6
β′	64,5	4,2 ; 3,8	46,2
β	72,5	4,6 ; 3,85 ; 3,70	45

Table 4.1 The characteristic XRD peaks for tristearin from literature (Lavigne, C. Bourgaux, & M. Ollivon., 1993).

4.4.1 Effect of temperature on polymorphism of 10% SSS solution

Wide angle (small d-spacing) ($2\theta = 5°$–$30°$) is used to identify the polymorphic form present in samples. The obtained d-spacings define subcell within the crystal lattice via Bragg's equation (Small, 1966). Figure 4.18 shows an example of a histogram of signal intensity as a function of 2θ for SSS cooled down from 80 °C to 20 °C at a cooling rate of 5 C°/min. The presence of peaks (at 3.65, 3.82, and 4.562 Å) confirms that the predominant

form is β (Figure 4.20) (Marangoni, 2013).

(a)
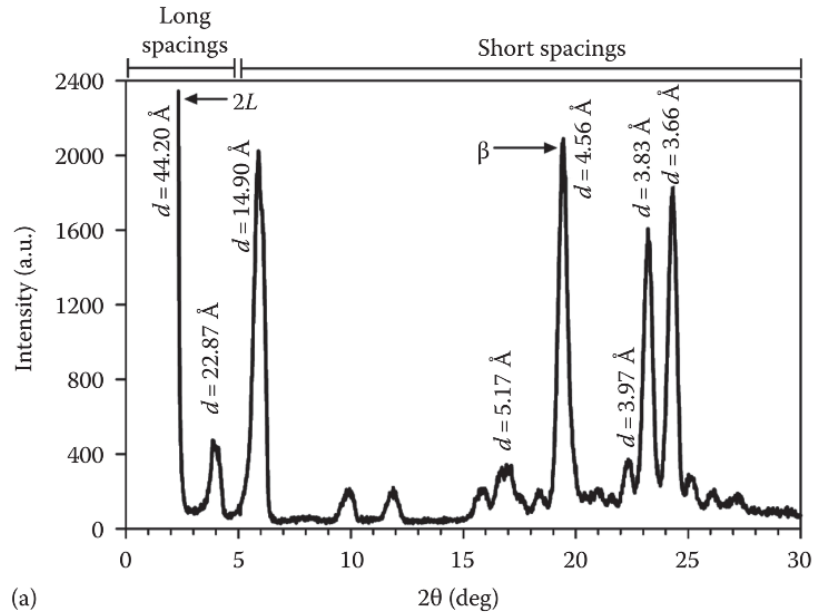
Figure 4.18 A histogram of signal intensity as a function of diffraction angle 2θ (1° to 30°) for SSS after being cooled down at 5 C°/min from 80 °C to 20 °C (Marangoni, 2013).

A similar result was obtained in this research. 10% SSS was first melted to erase all history (step a) for 10 minutes and then cooled from 70 °C to the designed temperature (35, 28, 20, 12, 5, 0, -5 °C) at a rate of 3 C°/min (step b). After reaching the set temperature, 10% SSS was then kept isothermal for 600 mins. To guarantee the quality of images, a long exposure time was chosen due to the low signal intensity of our x-ray beam. Each image was taken every 60 s, hence there were 600 images for each temperature.

An example of peak fitting results of WAXD data of 10% SSS solution at 35 °C via Igor Pro is shown in Figure 4.19. The residual plot (Figure 4.19 (b) upper plot) shows the error of fitting is no more than 1.1%. The data plot (Figure 4.19 (b) (middle plot) is the original WAXD of 10% SSS (intensity versus q). The fitting plot (Figure 4.19 (b) bottom plot) shows the fitted results of WAXD peaks of 10% SSS solution (intensity versus q). The green line is the baseline of the fitting. There are six peaks obtained from Igor fitting results. Among these peaks, it is found that peak 1, peak 4, and peak 6 are at 4.6 Å, 3.85 Å, and 3.7 Å, correspondingly. The locations of these three peaks indicate that SSS crystallized in

$\boldsymbol{\beta}$ form when kept at 35 °C. Following the same method, the d-spacings of peak 1, peak 4, and peak 6 at other selected crystallization temperatures are summarized in Table 4.2. The high consistency in locations of these three peaks indicates that SSS crystallized in the β form under all temperature groups.
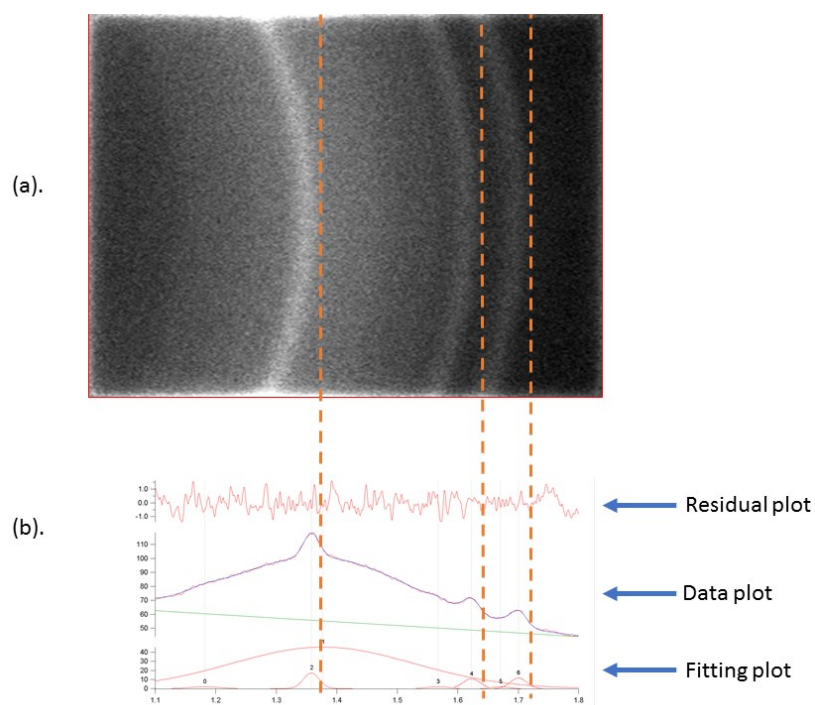
Figure 4.19 (a) An example of a stack of WAXD image of 10 % SSS solution at 35 °C with a cooling rate of 3C°/min. (b) An example of the corresponding fitted Wide-Angle diffraction patterns of 10% SSS solution.

	Peak 1 (Å)		Peak 4 (Å)		Peak 6 (Å)	
	Capillary A	Capillary B	Capillary A	Capillary B	Capillary A	Capillary B
35 °C	4.58459	4.55435	3.85991	3.84433	3.69434	3.67683
	± 0.00014	± 0.00035	± 0.00031	± 0.00018	± 0.00102	± 0.00019
28 °C	4.51833	4.40980	3.84495	3.83977	3.66531	3.67143
	± 0.00040	± 0.00114	± 0.00022	± 0.00006	± 0.00022	± 0.00117
20 °C	4.56262	4.53201	3.84824	3.85410	3.68389	3.67098
	± 0.00010	± 0.00035	± 0.00007	± 0.00017	± 0.00043	± 0.00014
12 °C	4.52028	4.54970	3.84099	3.83876	3.65460	3.66718
	± 0.00009	± 0.00027	± 0.00024	± 0.00045	± 0.00035	± 0.00078
5 °C	4.55171	4.59570	3.84223	3.84034	3.65324	3.67110
	± 0.00035	± 0.00011	± 0.00027	± 0.00002	± 0.00025	± 0.00024
0 °C	4.49763	4.47030	3.83319	3.8399	3.66115	3.64403
	± 0.00190	± 0.00030	± 0.00041	± 0.00015	± 0.00050	± 0.00029
-5 °C	4.50987	4.49248	3.83261	3.83776	3.64902	3.63373
	± 0.00037	± 0.00019	± 0.00029	± 0.00006	± 0.00191	± 0.00045

Table 4.2 The averaged d-spacing values of peak 1, peak 4, and peak 6 under the designed temperatures (35, 28, 20, 12, 5, 0 and -5 °C). In this experiment, two capillaries (A and B) were used at each temperature.

4.4.2 Effect of temperature on the d-spacings of the β form of SSS, crystallized from its pure melt

A previous research in the effect of temperature on d-spacings of pure TAGs and binary mixtures was done by Xiyan Deng, a former graduate student. She studied the WAXD peak patterns of TAGs in different polymorphism. For pure SSS, she compared six main peaks based on their general location (*i.e.*, larger d-spacing, medium spacing, and small d-spacing). The data was plotted by taking the d-spacings at -20 °C as a reference, which allows a better comparison within groups (Figure 4.20).
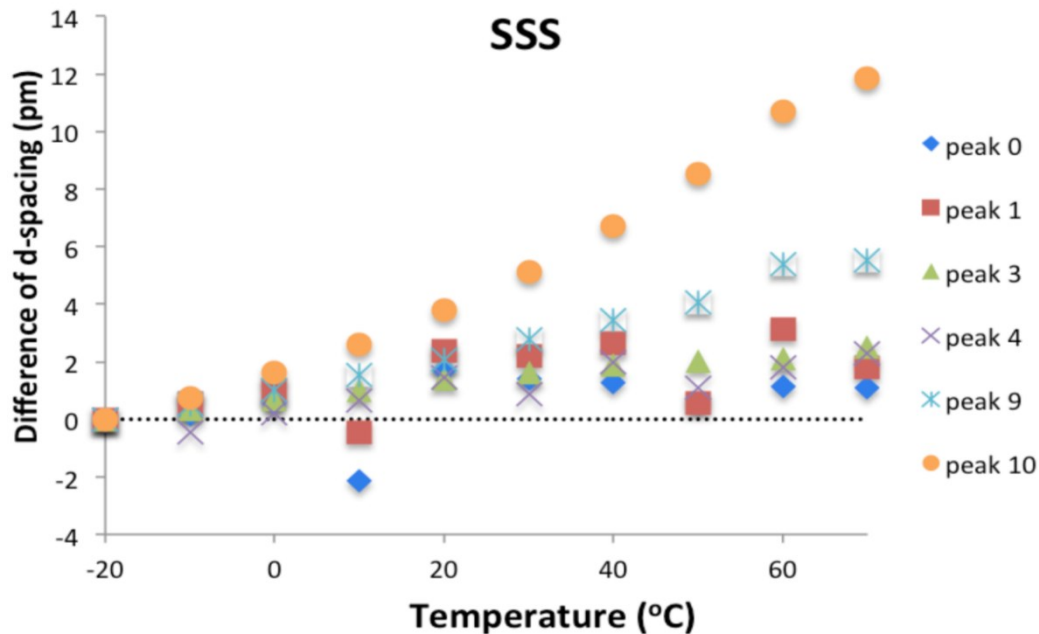
Figure 4.20 Differences of d-spacings of pure tristearin at the selected crystallization temperature. Adapted from (Deng, 2014).

The increase of temperature had no siginificant effects on the d-spacings for peaks with larger d-spacings (*e.g.,* peak 0 and peak 1). For peaks with medium d-spacing, the increase of temperature had a fairly limited role on the d-spacings. d-spacing increased 1 picometer when the temperature climbed from -20 °C to 10 °C. After 10 °C, the increase of temperature had no sigificant influence on d-spacings. The d-spacing of the peaks with smaller d-spacing, however, kept increasing when temperature increased.

The energy redistributes between the atoms of the molecules in nanocrystalline triacylglycerols as temperature increases. When thermal energy is added to the crystals, the d-spacings increase. This increase in d is observed by a decrease in the q value of the peak position. It was observed that peaks with larger d spacings, were not strongly affected by the increase in temperature. Thus, it seems that the larger d-spacing require a greater amount of energy to increase their distance. This happens because the amplitude of the thermal vibration of the atoms increases as temperature increases.

This unit cell expansion, where the characteristic periodicity "d" is changed, is observed by a decrease in the 2θ positions of the diffraction lines. If the positions of one or more lines are measured as a function of temperature, the thermal expansion of one specimen

116

can be obtained via X-ray diffraction (Cullity and Stock, 2001).

Therefore, Deng (2014) studied the positions of peaks with small-d-spacing as a function of temperature for pure TAGs and TAG mixtures. She measured the increase of d-spacings of Peak 9 and Peak 10 as the temperature increases for pure SSS (Deng, 2014). Hence, the mathematical relationships between the d-spacing and the crystal temperature were found. For the convenience of calculating temperature, these mathematical relationships are plotted with the d-spacing as x-axis and the temperature as y-axis (Figure 4.21). Thus, the temperature of the SSS crystal can be estimated from the known d-spacing values, measured via this XRD technique.

This method provides a new way to monitor and control the system temperature, especially at high shear rate. In the actual experiments, it was difficult to measure the sample temperature accurately due to many factors (*e.g.,* interference of the ambient temperature and viscous heating in shear flow). The deviation between the set temperature and the actual sample temperature can greatly influence the accuracy of the data. In Deng's research, the mathematic relationships between temperature and d-spacings can be used as a thermometer to estimate the actual sample temperature when the information of small d-spacings are known. It should be kept in mind that the temperatures obtained from the equation are still estimated values, but they are much closer to the actual temperatures in the samples. (Deng, 2014).

Temperature vd d-spacings

$y = -1.738x^2 + 1355.4x - 264175$

$y = -0.4681x^2 + 352.24x - 66201$

Peak9-Xiyan

Peak10-xiyan

Temperature: °C
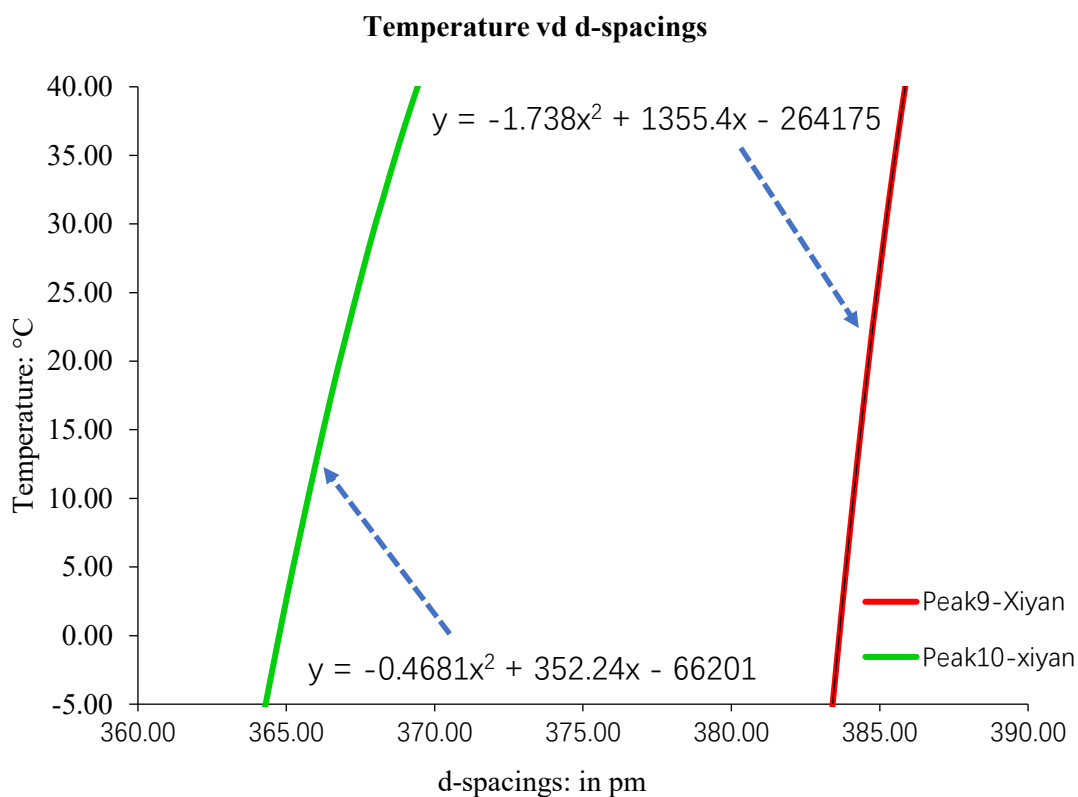
d-spacings: in pm

Figure 4.21 Temperature versus small d-spacings for peak 9 and peak 10 for pure tristearin. Modified from (Deng, 2014).

4.4.3 Effect of temperature on the d-spacings of the β form of SSS, crystallized from a 10% solution in dodecane

When the solution is cooled the SSS forms nanocrystals that remain in suspension in the liquid dodecane. The dodecane remains, however, saturated with SSS. At these temperatures the concentration of SSS in solution is negligible (See section 2.1).

An example of the fitted WAXD patterns of the pure tristearin and 10% SSS suspension is shown in Figure 4.22. It is found that the peaks of the lower plot are consistent with the peaks of the upper plot. This indicates that the crystals formed from the solution are indeed SSS crystals in the *β* form. Peak 9 and peak 10 in the upper plot (pure SSS) correspond to peak 4 and peak 6 in the lower plot (10% SSS suspension). Although peak 4 (upper plot) and peak 2 (lower plot) are also identified in the lower plot, the change in peak position (in

the reciprocal lattice spacing q) with respect to temperature for these two peaks is very small. This means that the influence of temperature on their corresponding d-spacings is not significant.
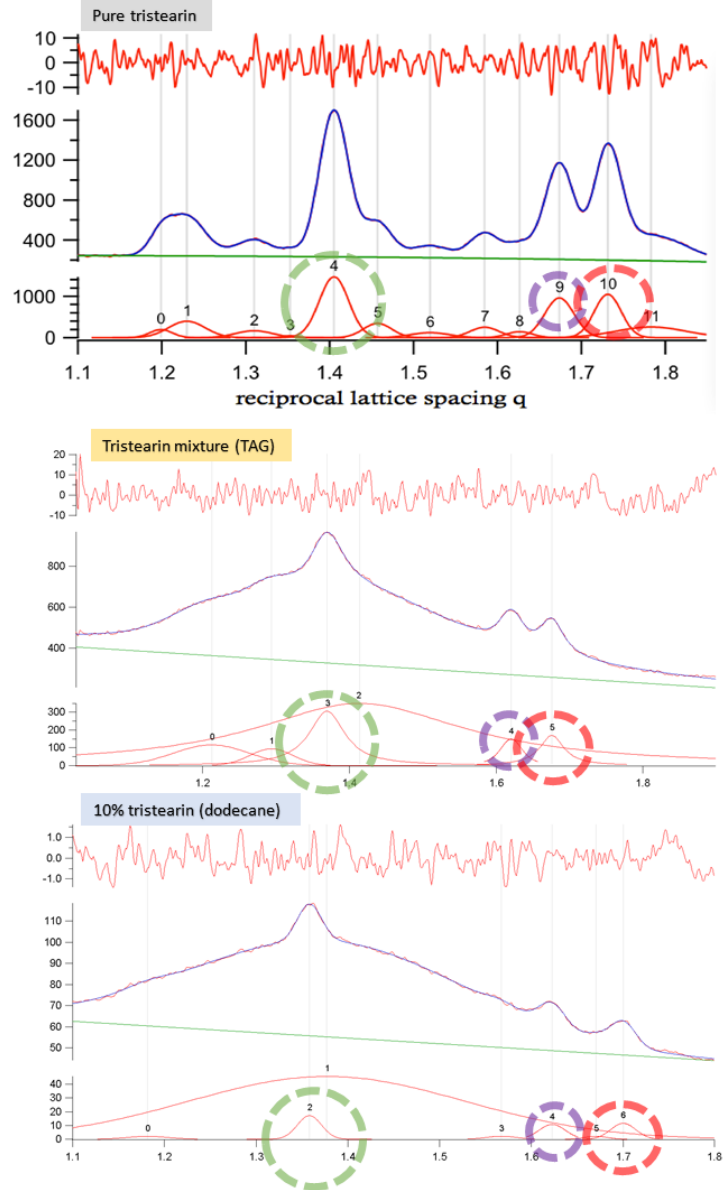
Figure 4.22 An example of a comparison between the pure SSS, SSS in TAG mixture and 10% SSS suspension (at 20 °C) (fitted by Igor pro) (peak number is assigned automatically by software).

The d-spacings that change significantly with temperature were plotted together in Figure 4.23. In Figure 4.23 (a), the d-spacings plotted correspond to peak 4. Along with these, the

equation that describes the d-spacing from Peak 10 (pure SSS) from Xiyan's model, was plotted. The confidence interval curves (CI at 95%) for Peak 10's function, were also plotted. Triangle and circle symbols were used to differentiate data from the two capillaries used.

In Figure 4.23 (b), the d-spacings plotted correspond to peak 6. Along with these, the equation that describes the d-spacing from Peak 9 (pure SSS) from Xiyan's model, was plotted. The confidence interval curves (CI at 95%) for Peak 9's function, were also plotted. Triangle and circle symbols were used to differentiate data from the two capillaries used.

Most of data are in CI region, which may suggests Deng's model still work in the dilluted 10% SSS solution. A statistical analysis, Pearson's chi-squared test (χ^2 test), was done to evaluate the goodness of fit between the experimental data from Peak 6 and Peak 4, and Deng's model. The chi-square goodness of fit tests shows that there is no certainty that our observed values are statistically similar (nor different) to the values expected under Xiyan's model (*i.e.,* for peak 6, $P_{(\chi2\ test)}=0.00325 < P_\alpha=0.05$; for peak 4, $P_{(\chi2\ test)}=0.00 < P_\alpha=0.05$). A definite conclusion cannot be made without more XRD data and powerful X-ray sources.

a.

Temperature vs small d-spacings (Peak 10 vs Peak 6)
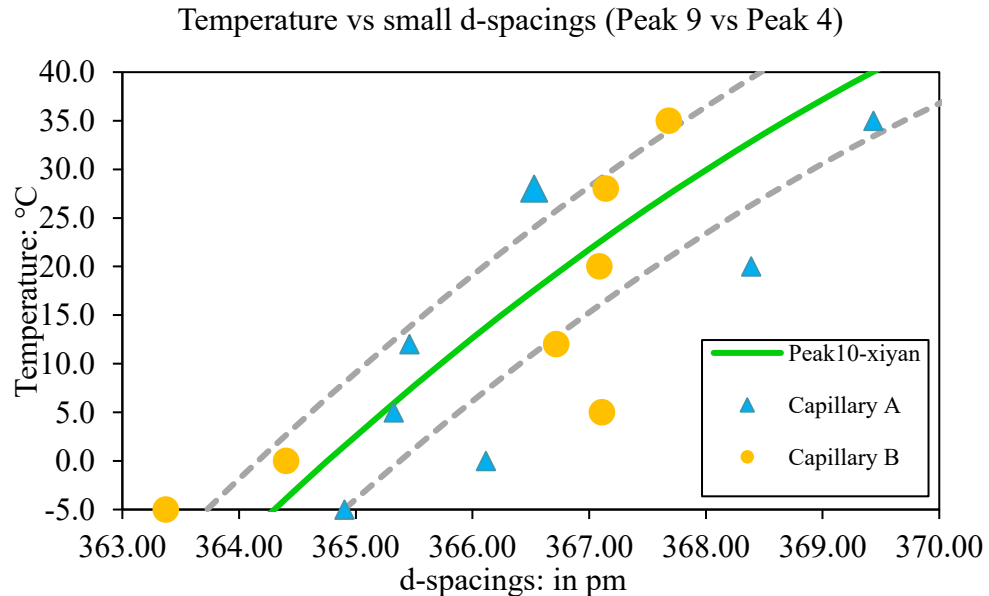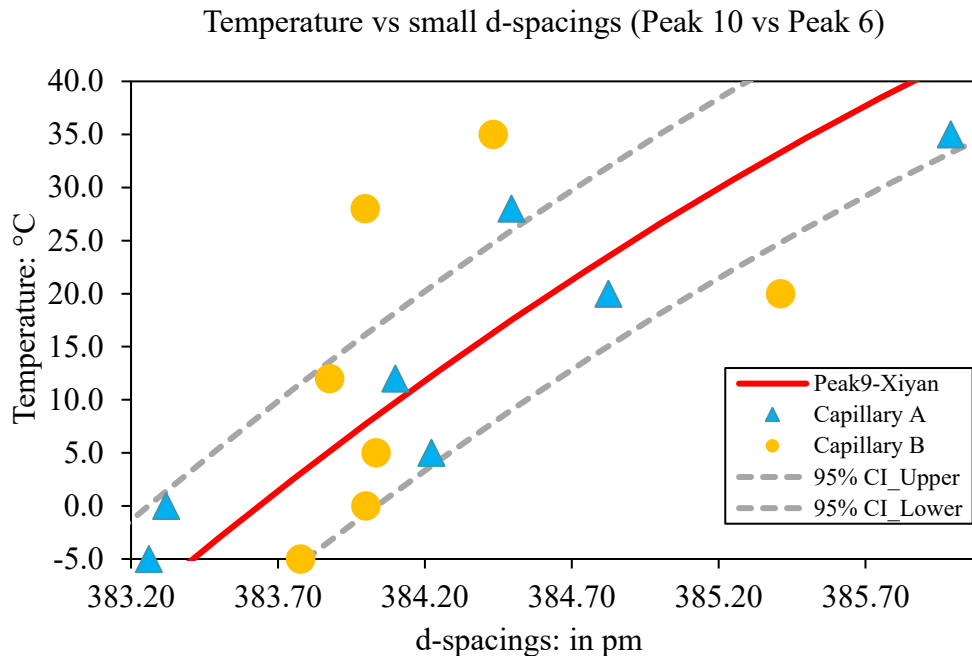
b.

Figure 4.23 (**a**) Temperature as a function of small d-spacings for Peak 10 (Xiyan's model) and Peak 6 (10% SSS). Xiyan's model for Peak 10 (reference value: 363.03 pm, at -20 °C) is shown as a green line. The WAXD results of Peak 6 from 10% SSS are shown in ▲●. (b) Temperature as a function of small d-spacings for Peak 9 (Xiyan's model) and Peak 4 (10% SSS). Xiyan's model for Peak 9 (reference value: 382.78 pm, at -20 °C) is shown as a red line. The WAXD results of Peak 4 from 10% SSS are shown in ▲●.

In these experiments, the x-ray diffracted intensity was expected to be about ten times weaker than in the experiments done by Deng with pure SSS. This is simply a consequence of the smaller mass of SSS per unit volume of x-ray beam in the capillary. Therefore, a longer acquisition time (600 mins) was chosen compared to Xiyan's experiment (100 mins).

The difference between the observed values and the expected values of d-spacings could be explained by several reseaons. The material, 10% SSS, is a suspension of Brownian SSS nanocrystals in a diluted solution. SSS nanocrystals tend to form clusters rather in a randomly distributed powder-like array in cappilary. Thus, the movement and distribution of clusters of these SSS crystals may influence the XRD data.

For example, the sedimentation of SSS clusters on the bottom or the surface of the capillary

was observed in experiments. The capillaries were removed from the temperature control cell, after their last crystallization at -5 °C. It was observed, in over half the cases, that a large proportion of crystalline clusters appeared to have decanted to the lower part of the capillary (Figure 4.24 (a)). A "bamboo" structure was once observed (Figure 4.24 (b)) in a capillary that had been at -5 °C. This heterogeneous distribution of SSS nanocrystals in capillary may increase or decrease the x-ray diffracted intensity than the expected value. In the case that they lowered it, the fitting error associated with the peak position would increase, since the background scattering of the liquid dodecane was very large. This scattering is seen as a large broad peak (Peak 2) in Figure4.22.
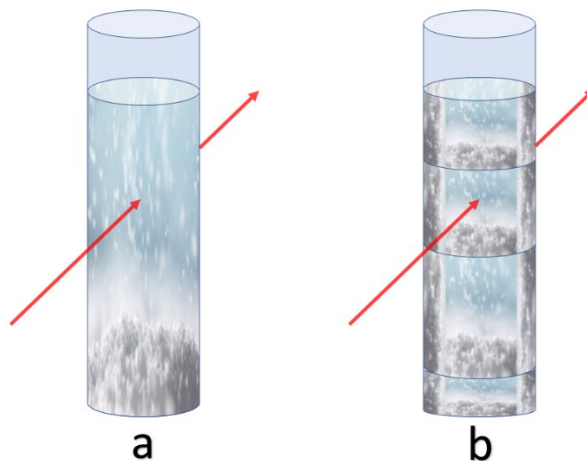
Figure 4.24 The schematic representation of possible distribution of SSS in the sample capillary.

4.5 MISCELLANEOUS

4.5.1 Dynamic Experiments

The application of shear flow in food industry has a long history, but the study of crystallization of fats under shear flow via X-ray diffraction is very recent (Guthrie et al., 2004; MacMillan et al., 2002; Mazzanti G., Li, Marangoni, & Idziak, 2011; Mazzanti, 2005; Mazzanti, Marangoni, & Idziak, 2005; Mazzanti, Marangoni, & Idziak, 2009). In Mazzanti's research team, the XRD patterns of fats under shear flow have been studied in a series of Couette cells as shown in Figure 4.25 (a).
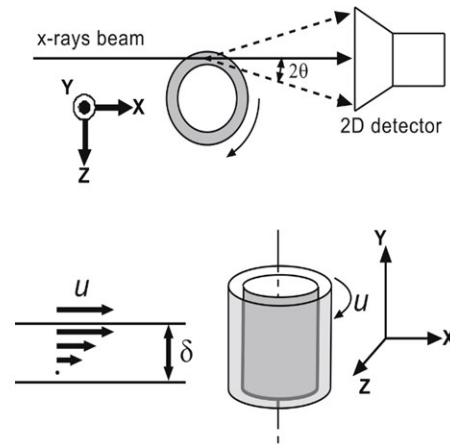
a.
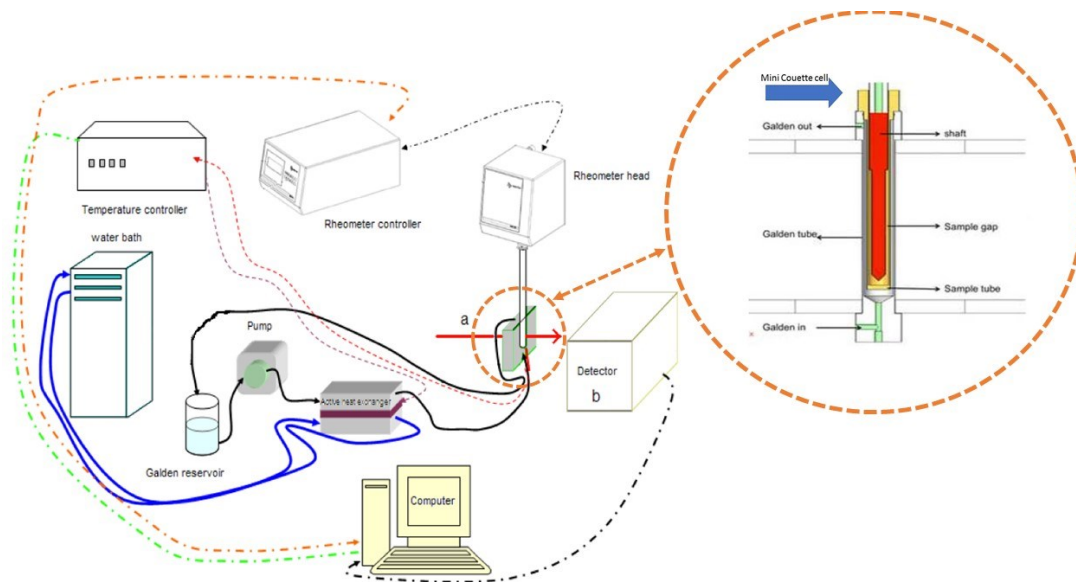
b.

Figure 4.25 (a) A Couette cell for synchrotron radiation experiments from (Mazzanti et al., 2005). (b) A Couette cell for in-house wide X-Ray diffraction experiments. Adapted from (Li, 2011).

As shown in Figure 4.25 (b), the second generrration of Mini-Couette cell was successfully used in Deng (2014) and Li (2011) research. Li studied the phase transitions during crystallization via time-resolved synchrotron X-ray diffraction. The Mini-Couette cell had been combined a rheometer head with a nuclear magnetic resonance (NMR) device. Time-resolved synchrotron X-ray diffraction experiments were done under similar conditions. Li (2011) found that shear induced a strong reduction in phase onset, transition time, and crystal size. As discussed in the previous section, Deng (2014) studied the relationship between temperature and the peak position of wide angle x-ray diffraction patterns of nanocrystalline triacylglycerols. She used both pure triacylglycerols and triacylglycerol mixtures crystallized in the desired polymorph in capillaries. She found that the d-spacing for the peaks with small d-spacing increased when the temperature increased. This relationship can be used to estimate the real sample temperature, especially under higher shear rate for pure triacylglycerols and triacylglycerol mixtures (Deng, 2014).

However, this Mini-Couette cell was broken due to deterioration. A new Mini-Couette cell

124

was then designed, which can combine multiple instruments (TA AR-2000, Rheometer measure head (Anton Paar Co), and NMR) with XRD experiments. The dimensions and material of Couette cell must be carefully determined to fit different instruments. Based on these requirements, a highly customized Mini-Couette cell was designed in Solidworks software. Additional details of this design are provided in a separate document.

5   CONCLUSION

As stated in the introduction, the aim of this research was to observe the behavior of triacylglycerol molecules that crystallize out of a non-polar solvent. The behaviour was observed for the crystallization of tristearin from a diluted 10% solution in dodecane. The tests included different crystallization temperatures (-5, 0, 5, 12, 20, 28, and 35 °C) and shear rates (0.9, 9, 90, and 900 s^{-1}). The behaviour was studied via differential scanning calorimetry (DSC), rheology, polarized light microscopy (PLM), and x-ray diffraction (XRD), as summarized in Figure 5.1.

As expected, the **DSC** tests provided preliminary information to select the temperature profiles for polarized light microscopy, rheology, and XRD experiments. A common purification method is to crystallize the triacylglycerols from a semipolar solvent, e.g. acetone, diethyl-ether or chloroform. In that case a single crystallization event to the stable form is observed (Walker, 1972). However, when crystallizing it from dodecane, instead of one crystallization event of a stable form, two events were observed.

As was anticipated, the onset temperatures of Peak 1 and Peak 2 decreased as cooling rates increased, in all pans and replicates. (see Fig. 4.2 and 4.3). Peak 1 onset decreased about 2 C° between 1 and 15 C°/min. The difference between the onset of Peak 2 and the onset of peak 1 did increase about 10 C° for the same range.

Comparison of the onset of peak 1 with the expected value of a diluted solution was done using the Hildebrand equation. It was found that the high onset temperatures of peak 1 could not be explained if the molecules were completely diluted and dispersed in the dodecane solvent. Even the inclusion of an activity coefficient correction (Margules, 1895) did not account for this high temperature. It was concluded that the tristearin molecules are probably clustered due to their polar cores, and thus behave as liquid melt nano-domains, that can crystallize in the α form at a temperature close to that of the bulk phase.

The relationship between cooling rate and onset temperature can be used to estimate the maximum onset temperature of peak 1 and peak 2 at any given cooling rate, from 1 to 15 C°/min. This provided a reference to set the maximum practical crystallization temperature that would ensure that complete crystallization had happened. For example, static XRD

126

experiments were done at a cooling rate of 3 C°/min. In that case, 35 °C is the maximum crystallization temperature possible. The static experiments did not seem to follow a traditional Avrami-like crystallization path.

The melting part of the thermograms provided also important information. The onset value of Peak 4 was around 69 °C. To melt/dissolve all crystals, a slightly higher temperature, 70 °C, was set as the conditioning temperature for static experiments. For experiments under shear flow, 60 °C was set as the conditioning temperature, due to the enhancement of mass and heat transfer.

For **rheology** measurements, the behaviour of the 10% SSS solution was studied in an AR2000 rheometer. Combinations of different crystallization temperatures (35, 28, 20, 12, 5, 0, and -5 °C) and shear rates (0.9, 9, 90, and 900 s^{-1}) were tested. The average cooling rate during the crystallization was between 4.5 and 1.7 C°/min, decreasing as temperature went lower.

Prior to the application of shear flow, the suspensions were formed by static crystallization during cooling to the chosen temperature ("step b"), and for 200 seconds at that temperature ("step c"). During this time, small deformation oscillatory rheology was applied to observe the changes in mechanical characteristics of the material, as it went from a solution to a suspension of tristearin crystals in dodecane. The final complex viscosity η* increased from 1.8 Pa·s to 2.6 Pa·s, with a temperature increase from -5 °C to 20 °C, and then decreased. The increase was somewhat unexpected. The viscosity of the dodecane solvent is exponentially reduced in that temperature increase range, from 2.46 mPa·s to 1.49 mPa·s. At all temperatures from -5 °C to 20 °C, the crystallized solid fraction was very close to 10%, as indicated by the DSC experiments. Thus, the increase in the complex viscosity must be due to changes in the shape or dimensions of the crystals and/or their clusters, rather than their volume fraction. During the formation of the crystals, the complex viscosity decreased as time progressed, e.g. from 2.5 to 2.0 Pa·s.

After the formation of the suspension, shear was applied for 1200 s. A general trend observed was that the apparent viscosity at the end of that period, η, decreases as shear rate increases, under the same crystallization temperature. Thus, from -5 to 35 °C, the 10%

tristearin suspensions exhibited "shear thinning". The shear thinning was well described by a power law function, except at 35 °C. The behaviour exponent "n" was between 0.4 and 0.6. The apparent viscosity ranged logarithmically from 10^{-3} to 10^{-1} Pa·s. Other common models (Einstein, Krieger-Dougherty) did not describe well the apparent viscosity of the suspensions.

After the shear step, the oscillatory procedure was applied again, in "step e". As time went on, η^* decreased for the material treated at low shear rates, and increased for the material treated at high shear rates. The final value of η^* ranged between 0.5 and 2.0 Pa·s for most materials. This final value was weakly affected by temperature (below 28 °C). The highest values were for the material treated at 90 s^{-1}, whereas the lower values were for the material treated at 9 s^{-1}. It is not straightforward to explain this behaviour. Furthermore, the behaviour at 35 and 28 °C followed different patterns. Further investigations exploring other volume fractions and temperature/time/shear combinations are needed.

A very clear conclusion of this section is that PLM, XRD and NMR experiments under shear flow are necessary to decipher this complex behaviour. What looks like a simple suspension of a pure solid in a pure solvent turned out to be material with a very rich gamut of behaviours.

PLM was used to visualize the suspensions obtained from the 10% SSS/dodecane solution under various crystallization temperatures (35, 28, 20, 12, 5, 0, and -5 °C) and shear rates (0.9, 9, 90, and 900 s^{-1}). As explained in the results section, it was not possible to obtain quantitative data on nucleation onset times. However, it was possible to observe qualitatively that the time (τ_c) that is required for crystals to reach the critical size and be visible under microscopy shifts to an earlier time with the applied shear. It was also observed qualitatively that the size and shape of the clusters of SSS crystals decreased under shear flow. Particularly important was the observation of segregation into smaller clusters with the application of shear. This is qualitatively consistent with a shear thinning behaviour. However, a broader range of experiments needs

To conduct **XRD** experiments under shear flow, it was first necessary to ascertain if the suspensions would generate a diffraction pattern that could be used to follow the

polymorphism, and perhaps the temperature. These experiments were conducted in capillaries, crystallizing the 10% SSS/dodecane solution. The results were then compared to Deng's research (2014) on undiluted triacylglycerol samples. It was concluded that it would be possible to identify and quantify the characteristic diffraction peaks necessary to identify the β polymorph, though less precision was obtained due to the dilution. Nonetheless, from -5 to 35 °C, it was clearly observed that the precise value of the small d-spacings at 0.364 nm and at 0.383 nm (nm at -5 °C) increased with temperature. This increase in d-spacing was modeled by Deng using a simple quadratic equation. Within this range of temperatures, the change expected was of the order of 6 pm (picometers) for the peak at 0.364 nm, and about 2.5 pm for the peak at 0.383 nm. The measurements of the d-sapcings from the suspensions are very close to the measurements for the undiluted SSS predicted by Deng. These results are very promising, despite their lax precision, not surprising under our in-house experimental constraints. This justifies conducting further experiments at a synchrotron light source.

To further explore the possibility of Deng's model under shear flow, a new shear cell was designed, which combines XRD and AR 2000. For future work, a heat exchanger was designed and printed by the 3D printer, which allows us to combine NMR, rheometer, and XRD at the same time. The possibility of using Deng's model as an intrinsic thermometer can be further developed if combined using this nova design of the combination of NMR-Rheometer-XRD technique.

The behaviour of SSS when crystallizing from its diluted solution in dodecane (non-polar solvent), showed a complexity and a variety that widely surpassed the initial expectations of this thesis. This opened many new questions that need to be further explored. Here are a few:

Are the SSS molecules really clustering? What is the size of these clusters and their temperature dependence? How is this affected by the concentration of SSS? Does the same happen with other saturated TAGs? And with unsaturated or mixed TAGs? What is the real 'equilibrium' structure of those 'solutions'?

Is there an orientation of the crystals when shear flow is applied? Is this correlated to the

shear thinning behaviour? What is the real temperature of the suspensions when subjected to high shear rates? Does it change the total amount of suspended solids by causing a partial dissolution?

Is it possible to design microscopy shear experiment that avoid the "coagulation" issues?

The thesis, thus, has expanded our knowledge of the crystallization of triacylglycerols and their interaction with non-polar solvents. Since the largest volume fraction of any triacylglycerol melt is the non-polar "sea" or alkyl chains, these findings should provide a good starting point to continue the study of the more general behaviour of fats.
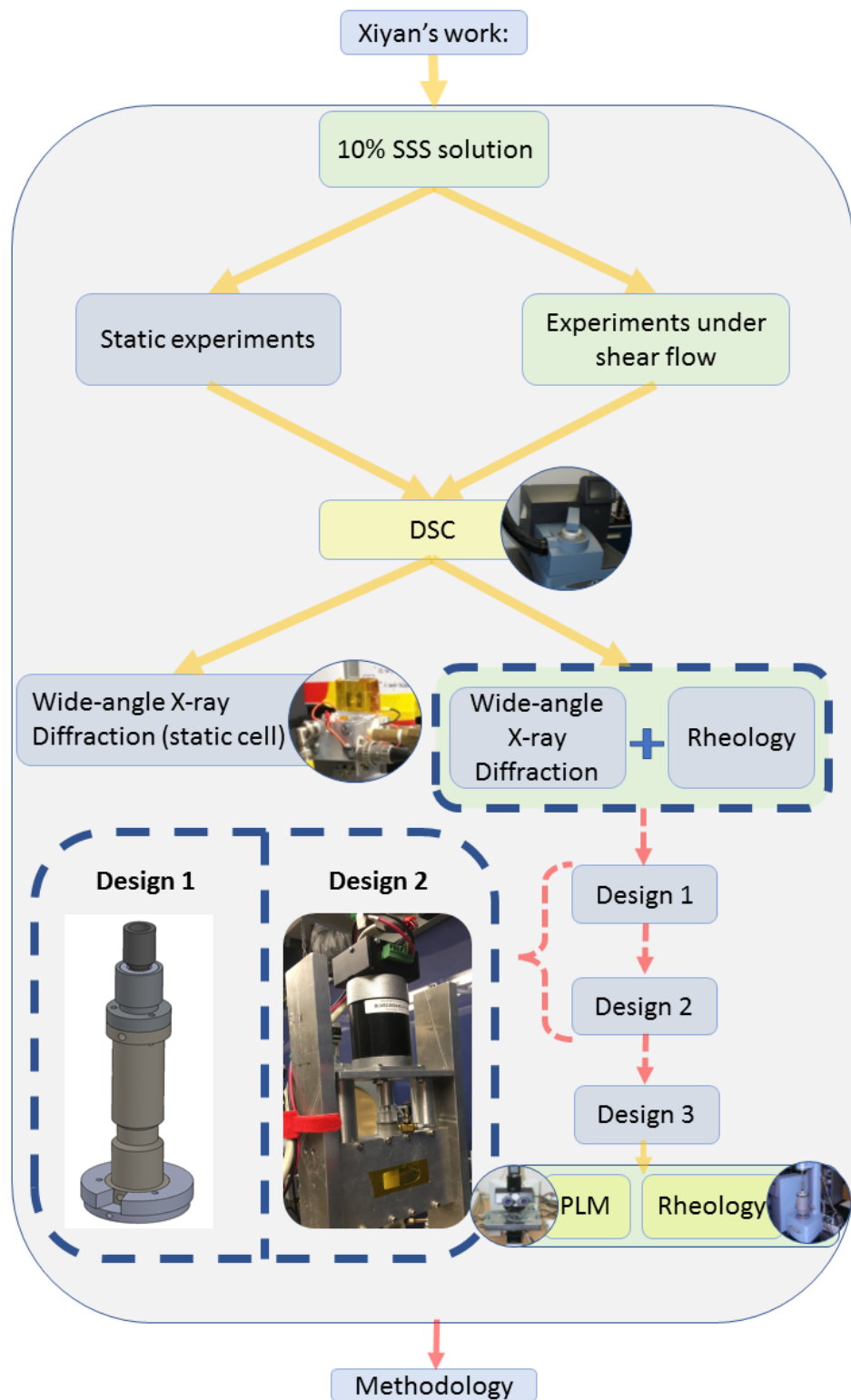
Figure 5.1 A workflow for the research.

BIBLIOGRAPHY

Acevedo, N. C., & Marangoni, A. G. (2010). Characterization of the Nanoscale in Triacylglycerol Crystal Networks. *Crystal Growth & Design, 10*(8), 3327-3333. doi:10.1021/cg100468e

Acevedo, N. C., & Marangoni, A. G. (2014). Functionalization of Non- interesterified Mixtures of Fully Hydrogenated Fats Using Shear Processing. *Food and Bioprocess Technology; An International Journal, 7*(2), 575-587. doi:10.1007/s11947-013-1110-z

Acevedo, N. C., & Marangoni, A. G. (2015). Nanostructured Fat Crystal Systems. *Annual Review of Food Science and Technology; Annu.Rev.Food Sci.Technol., 6*, 71-96. doi:10.1146/annurev-food-030713-092400

Al-Qatami, O. A. M. (2011). *Thermal study of a triglyceride mixture.* Thesis, Halifax, NS.

Ambrose, D., & Tsonopoulos, C. (1995). Vapor-Liquid Critical Properties of Elements and Compounds. 2. Normal Alkanes. *Journal of Chemical & Engineering Data, 40*(3), 531-546. doi:10.1021/je00019a001

Andrade, E. N. d. C. (1951). *Viscosity and plasticity*. New York: Chemical Pub. Co.

Arora, P. (2015). Image analysis of triacylglycerols crystallizing under shear flow. In E. Department of Process, S. Applied, S. Master of, G. Dr. Tom, G. Dr. Mark, P. Dr. Allan, M. Dr. Gianfranco (Eds.).

Avrami, M. (1939). Kinetics of Phase Change. I General Theory. *The Journal of chemical physics, 7*(12), 1103-1112. doi:10.1063/1.1750380

Avrami, M. (1940). Kinetics of Phase Change. II Transformation- Time Relations for Random Distribution of Nuclei. *The Journal of chemical physics, 8*(2), 212-224. doi:10.1063/1.1750631

Avrami, M. (1941). Granulation, Phase Change, and Microstructure Kinetics of Phase Change. III. *The Journal of chemical physics, 9*(2), 177-184. doi:10.1063/1.1750872
Bailey, A. E. (1979). *Bailey's Industrial oil and fat products* (4th ed.). New York: New York : Wiley.

Barnes, H. A. (1989). *An introduction to rheology*. Amsterdam ; New York: Amsterdam ; New York : Elsevier ; Distributors for the U.S. and Canada, Elsevier Science Pub. Co.

Benesi, H. A., & Hildebrand, J. H. (1949). A Spectrophotometric Investigation of the Interaction of Iodine with Aromatic Hydrocarbons. *Journal of the American Chemical Society, 71*(8), 2703-2707. doi:10.1021/ja01176a030

Berk, Z. (2009). Chapter 14:Crystallization and Dissolution. In ScienceDirect (Ed.), *Food process engineering and technology* (1st ed.. ed., pp. 318-331). Amsterdam ; Boston ; London; Amsterdam ; Boston: Amsterdam ; Boston ; London : Academic.

Blaak, R., Auer, S., Frenkel, D., & Löwen, H. (2004). Crystal nucleation of colloidal suspensions under shear. *Physical Review Letters, 93*(6), 068303-068303.

Boistelle, R. (1988). Crystallization and polymorphism of fats and fatty acids In N. Garti & K. Sato (Eds.), *Fundamentals of nucleation and crystal growth* (pp. 189-276). NewYor: Marcel Dekker.

Bondi, A. (1964). van der Waals Volumes and Radii. *The Journal of Physical Chemistry, 68*(3), 441-451. doi:10.1021/j100785a001

Bragg, W. H., Bragg, W. L., James, R. W., Lipson, H., Cochran, W., & Claringbull, G. F. (1933). *The crystalline state*. London: London : G. Bell.

Bunjes, H., & Unruh, T. (2007). Characterization of lipid nanoparticles by differential scanning calorimetry, X-ray and neutron scattering. *Advanced Drug Delivery Reviews, 59*(6), 379-402. doi:https://doi.org/10.1016/j.addr.2007.04.013

Campos, R., & Marangoni, A. G. (2014). Crystallization Dynamics of Shear Worked Cocoa Butter. *Crystal Growth & Design, 14*(3), 1199-1210. doi:10.1021/cg4017273

Campos, R., Narine, S. S., & Marangoni, A. G. (2002). Effect of cooling rate on the structure and mechanical properties of milk fat and lard. *Food Research International, 35*(10), 971-981. doi:10.1016/S0963-9969(02)00159-X

Caudwell, D. R., Trusler, J. P. M., Vesovic, V., & Wakeham, W. A. (2004). The Viscosity and Density of n-Dodecane and n-Octadecane at Pressures up to 200 MPa and Temperatures up to 473 K. *International Journal of Thermophysics, 25*(5), 1339-1352. doi:10.1007/s10765-004-5742-0

Cevc, G. (1987). *Phospholipid bilayers : physical principles and models*. New York: New York : Wiley (Vol. 1031, pp. 311-382).

Chang, R. (2000). *Physical Chemistry for the Chemical and the Biological Sciences* (third ed.). Sausalito, CA: University Science Books.

Chapman, D. (1962). The Polymorphism of Glycerides. *Chemical reviews, 62*(5), 433-456. doi:10.1021/cr60219a003

Coupland, J., & McClements, D. (1997). Physical properties of liquid edible oils. *Journal of the American Oil Chemists' Society, 74*(12), 1559-1564. doi:10.1007/s11746-997-00771

Damodaran, S., Parkin, K. L., Fennema, O. R., & Parkin, K. (2008). *Fennema's food chemistry* (Fourth edition.. ed.). Boca Raton: Boca Raton : CRC Press/Taylor & Francis.

David A, P. (2013). Chapter 3:Intermolecular Forces in Triacylglycerol Particles and Oils. In L. H. Wesdorp & A. G. Marangoni (Eds.), *Structure and properties of fat crystal networks* (2nd ed.. ed., pp. 101-119). Boca Raton, Fla.; Boca Raton: Boca Raton, Fla. : CRC Press.

De Graef, V., Van Puyvelde, P., Goderis, B., & Dewettinck, K. (2009). Influence of shear flow on polymorphic behavior and microstructural development during palm oil crystallization. *European Journal of Lipid Science and Technology, 111*(3), 290-302. doi:10.1002/ejlt.200800181

de Kruif, C. G., van Iersel, E. M. F., Vrij, A., & Russel, W. B. (1985). Hard sphere colloidal dispersions: Viscosity as a function of shear rate and volume fraction. *The Journal of chemical physics, 83*(9), 4717-4725. doi:10.1063/1.448997

deMan, J. M. (1992). X-ray diffraction spectroscopy in the study of fat polymorphism (Vol. 25, pp. 471-476).

Deng, X. (2014). Effect of Temperature on the Wide Angle X-Ray Diffraction of Nanocrystalline Triacylglycerols. In E. Department of Process, S. Applied, S. Master of, N. Dr. Benedict, M. Gibson, H. Dr. Jan, M. Dr. Gianfranco (Eds.).

Derdour, L., Pack, S. K., Skliar, D., Lai, C. J., & Kiang, S. (2011). Crystallization from solutions containing multiple conformers: A new modeling approach for solubility and supersaturation. *Chemical Engineering Science, 66*(1), 88-102. doi:10.1016/j.ces.2010.10.023

Dhonsi, D., & Stapley, A. G. F. (2006). The effect of shear rate, temperature, sugar and emulsifier on the tempering of cocoa butter. *Journal of Food Engineering, 77*(4), 936-942. doi:https://doi.org/10.1016/j.jfoodeng.2005.08.022

Dibildox-Alvarado, E., & Toro-Vazquez, J. (1997). Isothermal crystallization of tripalmitin in sesame oil. *Journal of the American Oil Chemists' Society, 74*(2), 69-76. doi:10.1007/s11746-997-0147-4

Einstein, A. (1906). Eine neue Bestimmung der Molek€ uldimensionen. *Annals of Physics, 324*, 289-306.

Einstein, A. (1911). Berichtigung zu meiner Arbeit: eine neue Bestimmung der Molekuldimensionen. *Annals of Physics, 339*, 591-592.

Erkey, C., Rodden, J. B., & Akgerman, A. (1990). A correlation for predicting diffusion coefficients in alkanes. *The Canadian Journal of Chemical Engineering, 68*(4), 661-665. doi:10.1002/cjce.5450680418

F. Lavigne, Bourgaux, C., & Ollivon, M. (1993). Phase transitions of saturated triglycerides. *Journal de Physique IV Colloque, 03*(8), 137-140.

Falkovich, G., & Falkovich, G. (2011). *Fluid mechanics a short course for physicists*. Cambridge ; New York: Cambridge ; New York : Cambridge University Press.

Fan, C. W., Michel, B. J., & Gianfranco, M. (2009). Viscous heating in a mini-Couette cell used in Rheo-XRD and Rheo-NMR research. *In the process of submission.*

Ferguson, R. H., & Lutton, E. S. (1941). The Polymorphic Forms or Phases of Triglyceride Fats. *Chemical reviews, 29*(2), 355-384. doi:10.1021/cr60093a010

Fick, A. (1855). Ueber Diffusion. *Annalen der Physik, 170*(1), 59-86. doi:10.1002/andp.18551700105

Formo, M. W. (1979). Physical properties of fats and fatty acids, chapter 3 Vol. 1, 5th edn. In D. Swern (Ed.), *Bailey's Industrial Oil and Fat Products* (Vol. 1, 5th ed.). New York, NY: John Wiley & Sons.

Foubert, I., Dewettinck, K., & Vanrolleghem, P. A. (2003). Modelling of the crystallization kinetics of fats. *Trends in Food Science & Technology, 14*(3), 79-92. doi:10.1016/S0924-2244(02)00256-X

Foubert, I., Vanrolleghem, P., & Dewettinck, K. (2005). *Insight in model parameters by studying temperature influence on isothermal cocoa butter crystallization* (Vol. 107).

Foubert, I., Vanrolleghem, P. A., Vanhoutte, B., & Dewettinck, K. (2002). Dynamic mathematical model of the crystallization kinetics of fats. *Food Research International, 35*(10), 945-956. doi:10.1016/S0963-9969(02)00157-6

Garti, N., & Sato, K. (2001). *Crystallization processes in fats and lipid systems*. New York: New York : Marcel Dekker. (pp. 140-152).

Ghosh, S., Tran, T., & Rousseau, D. (2011). Comparison of Pickering and network stabilization in water-in-oil emulsions. *Langmuir : the ACS journal of surfaces and colloids, 27*(11), 6589. doi:10.1021/la200065y

Gokcen, N. A. (1996). Gibbs-duhem-margules laws. *Journal of Phase Equilibria, 17*(1), 50-51. doi:10.1007/BF02648369

Guth, E., & Simha, R. (1936). Untersuchungenube die Viskositat von Suspensionen und Losungen 3. Uber die Viskositat von Kugelsuspensionen. *Kolloid-Z* (74), 266-275.

Hagemann, J., & Rothfus, J. (1983). Polymorphism and transformation energetics of saturated monoacid triglycerides from differential scanning calorimetry and theoretical modeling. *Journal of the American Oil Chemists' Society, 60*(6), 1123-1131. doi:10.1007/BF02671340

Hamaker, H. C. (1937). The London—van der Waals attraction between spherical particles (Vol. 4, pp. 1058-1072).

Hartel, R. W. (2001a). *Crystallization in foods*. Gaithersburg, Md.: Gaithersburg, Md. : Aspen Publishers.

Hartel, R. W. (2001b). *Crystallization in foods*. Gaithersburg, Md.: Aspen Publishers.

Herrera, M. L., de León Gatti, M., & Hartel, R. W. (1999). A kinetic analysis of crystallization of a milk fat model system. *Food Research International, 32*(4), 289-298. doi:10.1016/S0963-9969(99)00083-6

Herrera, M. L., Falabella, C., Melgarejo, M., & Añón, M. (1998). Isothermal crystallization of hydrogenated sunflower oil: I—Nucleation. *Journal of the American Oil Chemists' Society, 75*(10), 1273-1280. doi:10.1007/s11746-998-0172-y

Himawan, C., Starov, V. M., & Stapley, A. G. F. (2006). Thermodynamic and kinetic aspects of fat crystallization. *Advances in Colloid and Interface Science, 122*(1), 3-33. doi:10.1016/j.cis.2006.06.016

Hjorth, J. L., Miller, R. L., Woodley, J. M., & Kiil, S. (2015). Kinetic modeling of multi-component crystallization of industrial- grade oils and fats. *European Journal of Lipid Science and Technology, 117*(7), 1066-1078. doi:10.1002/ejlt.201400263

I, E. D. (1961). General theory of van der waals' forces (Vol. 4, pp. 153-176).

Israelachvili, J. N. (2011). *Intermolecular and surface forces* (3rd ed.. ed.). Burlington, MA: Burlington, MA : Academic Press.

Jackson, K. A. (2004a). Constitutional supercooling surface roughening. *Proceedings of the Symposium - Progress in Crystal Growth, 264*(4), 519-529. doi:http://dx.doi.org/10.1016/j.jcrysgro.2003.12.074

Jackson, K. A. (2004b). Diffusion in Fluid. In K. A. Jackson (Ed.), *Kinetic Processes: Crystal Growth, Diffusion, and Phase Transitions in Materials* (pp. 165-172). Weinheim: WILEY-VCH Verlag GmbH & Co. KGaA.

Jensen, L. H., & Mabis, A. J. (1963). Crystal Structure of β-Tricaprin. *Nature, 197*(4868), 681. doi:10.1038/197681d0

Jensen, L. H., & Mabis, A. J. (1966). Refinement of the structure of β- tricaprin. *Acta Crystallographica, 21*(5), 770-781. doi:10.1107/S0365110X66003839

Kaufmann, N., Graef, V., Dewettinck, K., & Wiking, L. (2012). Shear- induced Crystal Structure Formation in Milk Fat and Blends with Rapeseed Oil. *Food Biophysics, 7*(4), 308-316. doi:10.1007/s11483-012-9269-9

Kaufmann, N., Kirkensgaard, J., Andersen, U., & Wiking, L. (2013). Shear and Rapeseed Oil Addition Affect the Crystal Polymorphic Behavior of Milk Fat. *Journal of the American Oil Chemists' Society, 90*(6), 871-880. doi:10.1007/s11746-013-2226-z

Kawamura, K. (1979). The DSC thermal analysis of crystallization behavior in palm oil. *Journal of the American Oil Chemists' Society, 56*(8), 753-758. doi:10.1007/BF02663056

Kessler, H., Zimmermann, G., Förster, H., Engel, J., Oepen, G., & Sheldrick, W. S. (1981). *Does a Molecule have the Same Conformation in the Crystalline State and in Solution? Comparison of NMR Results for the Solid State and Solution with those of the X-ray Structural Determination.* Angewandte Chemie International Edition in English*, 20*(12), 1053-1055. doi:10.1002/anie.198110531

Kiselev, M., & Lombardo, D. (2016). *Structural Characterization in Mixed Lipid Membrane Systems by Neutron and X-ray scattering* (Vol. 1861).

Kloek, W. (1998). *Mechanical properties of fats in relation to their crystallization, PHD thesis.* (Dissertation/Thesis, Unpublished), University of Wageningen, The Netherlands.

Kloek, W., Van Vliet, T., & Walstra, P. (2005). Mechanical properties of fat dispersions prepared in a mechanical crystallizer. *Journal of Texture Studies, 36*(5), 544-568. doi:10.1111/j.1745-4603.2005.00031.x

Kloek, W., Walstra, P., & van Vliet, T. (2000). Nucleation kinetics of emulsified triglyceride mixtures. *Journal of the American Oil Chemists' Society, 77*(6), 643-652. doi:10.1007/s11746-000-0104-7

Kloek, W., Walstra, P., & Vliet, T. (2000). Nucleation kinetics of emulsified triglyceride mixtures. *Journal of the American Oil Chemists' Society, 77*(6), 643-652. doi:10.1007/s11746-000-0104-7

Kubota, N. (2001). Effect of Impurities on the Growth Kinetics of Crystals. *Crystal Research and Technology, Vol.36*(8-10), 749-769. doi:10.1002/1521-4079(200110)36:8

Landau, L., & Lifshitz, E. (1968). *Electrodynamics*. Moscow, Russia:: Nauka.

Larson, R. G. (1999). *The structure and rheology of complex fluids*. New York: New York : Oxford University Press.
Larsson, K. (1966). Classification of glyceride crystal forms. *Acta chemica Scandinavica, 20*(8), 2255.

Larsson, K. (1994). *Lipids-molecular organization, physical functions and technical applications*. Sweden: The Oily Press LTD.

Leckband, D., & Israelachvili, J. (2001). Intermolecular forces in biology. *Quarterly reviews of biophysics; Quart.Rev.Biophys., 34*(2), 105-267. doi:doi:10.1017/S0033583501003687

Li, M. (2011). *Rheo-nmr and synchrotron x-ray diffraction racterization of nanostructures of triglycerides crystallizing from solutions: Chapter 2*: Department of Process Engineering and, Applied Science. Master of, Dr. Zwanziger and Dr. Budge. M. Dr. Gianfranco (Eds.).

Lifshitz, E. M. (1956). The theory of molecular attractive forces between solids. *Sov. Phys.JETP, 2*, 73-83.

Lutton, E. S. (1948). Triple chain-length structures of saturated triglycerides. *Journal of the American Chemical Society, 70*(1), 248.

Maleky, F., Acevedo, N. C., & Marangoni, A. G. (2012). Cooling rate and dilution affect the nanostructure and microstructure differently in model fats. *European Journal of Lipid Science and Technology, 114*(7), 748-759. doi:10.1002/ejlt.201100314

Maleky, F., & Marangoni, A. G. (2008). Process development for continuous crystallization of fat under laminar shear. *Journal of Food Engineering, 89*(4), 399-407. doi:10.1016/j.jfoodeng.2008.05.019

Maleky, F., Smith, A. K., & Marangoni, A. (2011). Laminar Shear Effects on Crystalline Alignments and Nanostructure of a Triacylglycerol Crystal Network. *Crystal Growth & Design, 11*(6), 2335-2345. doi:10.1021/cg200014w

Marangoni, A. G. (1998). On the use and misuse of the avrami equation in characterization of the kinetics of fat crystallization. *Journal of the American Oil Chemists' Society, 75*(10), 1465-1467. doi:10.1007/s11746-998-0203-8

Marangoni, A. G. (2013). Chapter 2 Nucleation.and.Crystalline.Growth.Kinetics. In L. H. Wesdorp (Ed.), *Structure and properties of fat crystal networks* (2nd ed.. ed., pp. 27). Boca Raton, Fla.; Boca Raton: Boca Raton, Fla. : CRC Press.

Marangoni, A. G., Acevedo, N., Maleky, F., Co, E., Peyronel, F., Mazzanti, G., . . . Pink, D. (2011). Structure and Functionality of Edible Fats. *Soft Matter, 8*(5).

Marangoni, A. G., & Narine, S. S. (2002a). Identifying key structural indicators of mechanical strength in networks of fat crystals. *Food Research International, 35*(10), 957-969. doi:10.1016/S0963-9969(02)00158-8

Marangoni, A. G., & Narine, S. S. (2002b). *Physical Properties of Lipids. Marcel Dekker, Inc., New York, NY*. New York, NY: Marcel Dekker, Inc.

Marangoni, A. G., & Wesdorp, L. H. (2013). Structure and properties of fat crystal networks. In A. G. Marangoni & L. H. Wesdorp (Eds.), (2nd ed., pp. 1 online resource (500 p.)). Boca Raton, Fla.: CRC Press,.

Margules, M. (1895). Über die Zusammensetzung der gesättigten Dämpfe von Misschungen. *Sitzungsberichte der Kaiserliche Akadamie der Wissenschaften Wien Mathematisch-Naturwissenschaftliche Klasse II, 104*, 1243-1278.

Matovic, M., Miltenburg, J. C. v., Los, J. H., Gandolfo, F. G., & Floter, E. (2005). Thermal properties of tristearin by adiabatic and differential scanning calorimetry. *Journal of Chemical and Engineering Data, 50*, 1624-1630.

Matovic, M., van Miltenburg, J. C., Los, J., Gandolfo, F. G., & Floter, E. (2005). Thermal Properties of Tristearin by Adiabatic and Differential Scanning Calorimetry. *Journal of Chemical and Engineering Data, 50*, 1624-9568.

Mazzanti, G. (2005). Chapter 11: Crystallization of bulk fats under shear. In J. R. Dutcher & A. G. Marangoni (Eds.), *Soft materials : structure and dynamics* (pp. 279-297). New York: CRC Press 2004.

Mazzanti, G., Guthrie, S. E., Marangoni, A. G., & Idziak, S. H. J. (2007). A Conceptual Model for Shear-Induced Phase Behavior in Crystallizing Cocoa Butter. *Crystal Growth & Design, 7*(7), 1230-1241. doi:10.1021/cg050467r

Mazzanti, G., Guthrie, S. E., Sirota, E. B., Marangoni, A. G., & Idziak, S. H. J. (2003). Orientation and phase transitions of fat crystals under shear *Crystal Growth and Design, 3*.

Mazzanti, G., Li, M., Marangoni, A., & Idziak, S. (2011). Effects of Shear Rate Variation on the Nanostructure of Crystallizing Triglycerides. *Crystal Growth and Design, 11*(10). doi:10.1021/cg200786k

Mazzanti, G., Marangoni, A. G., & Idziak, S. H. J. (2005). Modeling Phase Transitions During the Crystallization of a Multicomponent Fat Under Shear. *Phys.Rev.E, 71*. doi:10.1103/PhysRevE.71.041607

Mazzanti, G., Marangoni, A. G., & Idziak, S. H. J. (2008). Modeling of a two- regime crystallization in a multicomponent lipid system under shear flow. *The European Physical Journal E; Soft Matter, 27*(2), 135-144. doi:10.1140/epje/i2007-10359-0

McClements, D. J., & Decker, E. A. (2008). Part I Major Food Components: Chapter 4 Lipids. In S. Damodaran, K. L. Parkin, O. R. Fennema, & K. Parkin (Eds.), *Fennema's food chemistry* (Fourth edition ed., pp. 155). Boca Raton: Boca Raton : CRC Press/Taylor & Francis.

McLaughlin, S. (1989). The electrostatic properties of membranes. *Annual review of biophysics and biophysical chemistry JID - 8505748*(18), 7812-7824.

Metin, S., & Hartel, R. (1998). Thermal analysis of isothermal crystallization kinetics in blends of cocoa butter with milk fat or milk fat fractions. *Journal of the American Oil Chemists' Society, 75*(11), 1617-1624. doi:10.1007/s11746-998-0102-z

Metin, S., & Hartel, R. W. (2005). Crystallization of Fats and Oils *Bailey's Industrial Oil and Fat Products*: John Wiley & Sons, Inc.

Mooney, M. (1951). The viscosity of a concentrated suspension of spherical particles (Vol. 6, pp. 162-170).

Moore, D. W., Burkardt, L. A., & McEwan, W. S. (1956). Viscosity and Density of the Liquid System TNT-Picric Acid and Four Related Pure Materials. *The Journal of chemical physics, 25*(6), 1235-1241. doi:10.1063/1.1743185

Morad, N. A., Idrees, M., & Hasan, A. A. (1995). Specific heat capacities of pure triglycerides by heat-flux differential scanning calorimetry. *Journal of thermal analysis, 45*(6), 1449-1461. doi:10.1007/bf02547438

Moran, D. P. J. (1994). Fats in Spreadable Products. In D. P. J. Moran & K. K. Rajah (Eds.), *Fats in Food Products* (pp. 155-211). Boston, MA: Springer US.

Mudge, E. M., & Mazzanti, G. (2009). Rheo-NMR Measurements of Cocoa Butter Crystallized Under Shear Flow. *Crystal Growth & Design, 9*(7), 3111-3118. doi:10.1021/cg800999y

Munson, B. R. (2013). *Fundamentals of fluid mechanics* (7th ed.). Hoboken, NJ: Hoboken, NJ : John Wiley & Sons, Inc.

Mutaftschiev, B. (1993). Nucleation Theory. In D. T. J. Hurle (Ed.), *Handbook of crystal growth*. Amsterdam: Amsterdam : North-Holland/Elsevier.

Narine, S. S., & Humphrey, K. L. (2004). A comparison of lipid shortening functionality as a function of molecular ensemble and shear: microstructure, polymorphism, solid fat content and texture. *Food Research International, 37*(1), 28-38. doi:10.1016/j.foodres.2003.09.013

Narine, S. S., & Marangoni, A. G. (1999). Relating structure of fat crystal networks to mechanical properties: a review. *Food Research International, 32*(4), 227-248. doi:10.1016/S0963-9969(99)00078-2

Nawar, W. (1996). Lipids. In R. F. Owen (Ed.), *Food chemistry* (3 rd ed ed., pp. 225-319). NewYor: Marcel Dekker.

Nielsen, S. S. (2010). *Food analysis* (4th ed.. ed., pp.164-180). New York

Noyes, A. A., & Whitney, W. R. (1897). The rate of solution of solid substances in their own solutions. *J. Am. Chem. Soc, 19*(12), 930-934. doi:10.1021/ja02086a003

Ortega-Rivas, E. (2012). Chapter 7:Separation Techniques for Solids and Suspensions: . In C. Ebooks (Ed.), *Non-thermal food engineering operations* (pp. P147-P148). New York: New York : Springer.

Papir, Y. S., & Krieger, I. M. (1970). Rheological studies on dispersions of uniform colloidal spheres (Vol. 34, pp. 126-130).

Pérez-Martínez, D., Alvarez-Salas, C., Charó-Alonso, M., Dibildox-Alvarado, E., & Toro-Vazquez, J. (2007). The cooling rate effect on the microstructure and rheological properties of blends of cocoa butter with vegetable oils. *Food Research International, 40*(1), 47-62. doi:10.1016/j.foodres.2006.07.016

Peschar, R., Pop, M. M., de Ridder, D. J. A., van Mechelen, J. B., Driessen, R. A. J., & Schenk, H. (2004). Crystal structures of 1,3- distearoyl- 2- oleoylglycerol and cocoa butter in the ß(V) phase reveal the driving force behind the occurence of fat bloom on chocolate. *The journal of Physical Chemistry.B, 108*(40), 15450-15453.

R.F.Strickland-Constable. (1968). Kinetics and Mechanisms of Crystallization. In R. F. Strickland-Constable (Ed.), *Kinetics and Mechanisms of Crystallization* (pp. 74-129). London, U.K.: Academic Press.

Roos, Y. o. H., & Roos, Y. H. (1995). Chapter 5: Food components and polymers (pp. 152-172). San Diego: San Diego : Academic Press.

Rosenthal, D. J., & Teja, A. S. (1989). The critical properties of n-alkanes using a low-residence time flow apparatus. *AIChE Journal, 35*(11), 1829-1834. doi:10.1002/aic.690351109

Rousset, P. (2002). Modeling Crystallization Kinetics of Triglycerides. In A. G. Marangoni & S. S. Narine (Eds.), *Physical properties of lipids*. New York: Marcel Dekker In.

Rutter, J. W., & Chalmers, B. (1953). A prismatic substructure formed during solidification of metals. *Canadian Journal of Physics, 31*(1), 15-39. doi:10.1139/p53-003; 0510.1139/p53-003

S.E.Friberg, & K.Larsson. (1997). *Food Emulsions* (3rd edition ed.). New York: Marcel Dekker.

Sato, K. (2001). Crystallization behaviour of fats and lipids — a review. *Chemical Engineering Science, 56*(7), 2255-2265. doi:10.1016/S0009-2509(00)00458-9

Sato, K., & Ueno, S. (2005). Chapter 3: Polymorphism in Fats and Oils. In F. Shahidi (Ed.), *Bailey's industrial oil and fat products, 6th ed.; v.1: Edible oil and fat products: chemistry, properties, and health effects* (6th Edition ed., Vol. 29, pp. n/a). Portland: Ringgold Inc.

Sekerka, R. F. (1965). A Stability Function for Explicit Evaluation of the Mullins-Sekerka Interface Stability Criterion. *Journal of Applied Physics, 36*(1), 264-268. doi:10.1063/1.1713887

Sherman, P. (1968). *Emulsion science*. London, New York: London, New York, Academic Press.

Small, D. M. (1966). *Handbook of Lipid Research*. New York: Plenum Press.

Smits, A. J. (2006). *Turbulent shear layers in supersonic flow* (2nd ed.. ed.). New York: New York : Springer.

Sonwai, S., & Mackley, M. (2006). The effect of shear on the crystallization of cocoa butter. *Journal of the American Oil Chemists' Society, 83*(7), 583-596. doi:10.1007/s11746-006-1243-6

Sonwai, S., & Mackley, M. R. (2006). The effect of shear on the crystallization of cocoa butter. *Journal of the American Oil Chemists' Society, 83*(7), 583-596. doi:10.1007/s11746-006-1243-6

Stapley, A., Tewkesbury, H., & Fryer, P. (1999). The effects of shear and temperature history on the crystallization of chocolate. *Journal of the American Oil Chemists' Society, 76*(6), 677-685. doi:10.1007/s11746-999-0159-3

Takeuchi, M., Ueno, S., & Sato, K. (2003). Synchrotron Radiation SAXS/WAXS Study of Polymorph-Dependent Phase Behavior of Binary Mixtures of Saturated Monoacid Triacylglycerols. *Crystal Growth & Design, 3*(3), 369-374. doi:10.1021/cg025594r

Tarabukina, E., Jego, F., Haudin, J. M., Navard, P., & Peuvrel-Disdier, E. (2009). Effect of Shear on the Rheology and Crystallization of Palm Oil. *Journal of Food Science, 74*(8), E405-E416. doi:10.1111/j.1750-3841.2009.01304.x

Teja, A. S., Lee, R. J., Rosenthal, D., & Anselme, M. (1990). Correlation of the critical properties of alkanes and alkanols. *Fluid Phase Equilibria, 56*(Supplement C), 153-169. doi:https://doi.org/10.1016/0378-3812(90)85100-O

Timms, R. E. (1995). Developments in Oils and Fats. In R. J. Hamilton (Ed.), (pp. 204-223). U.K.: Chapman & Hall, Glasgow.

Toro-Vazquez, J., Briceño-Montelongo, M., Dibildox-Alvarado, E., Charó-Alonso, M., & Reyes-Hernández, J. (2000). Crystallization kinetics of palm stearin in blends with sesame seed oil. *Journal of the American Oil Chemists' Society, 77*(3), 297-310. doi:10.1007/s11746-000-0049-x

Toro-Vazquez, J., Herrera-Coronado, V., Dibildox-Alvarado, E., Charo-Alonso, M., & Gomez-Aldapa, C. (2002). Induction Time of Crystallization in Vegetable Oils, Comparative Measurements by Differential Scanning Calorimetry and Diffusive Light Scattering. *Journal of Food Science, 67*(3), 1057-1064. doi:10.1111/j.1365-2621.2002.tb09453.x

Toro-Vazquez, J. F., Dibildox-Alvarado, E., Herrera-Coronado, V., & Charó-Alonso, M. (2002). Engineering and food for the 1st century. In J. Welti-Chanes, G. V. Barbosa-Cánovas, & J. M. Aguilera (Eds.), *Food preservation technology series* (pp. 1068 p.). Boca Raton, Fla.: CRC Press.

Toro-Vazquez, J. F., Diblidox-Alvarado, E., Herrera-Coronado, H., & Charo-Alonso, M. (2001). Triacylglyceride crystallization invegetable oils: application of models, measurements, and limi-tations. In Knovel, N. Widlak, R. W. Hartel, & S. Narine (Eds.), *Crystallization and solidification properties of lipids* (Eds ed., pp. 53-78). Champaign, Ill.: Champaign, Ill. : AOCS Press.

Tran, T., & Rousseau, D. (2016). Influence of shear on fat crystallization. *Food Research International, 81*, 157-162. doi:10.1016/j.foodres.2015.12.022

Turnbull, D., & Fisher, J. C. (1949). Rate of Nucleation in Condensed Systems. *The Journal of chemical physics, 17*(1), 71-73. doi:10.1063/1.1747055

Unruh, T., Bunjes, H., Westesen, K., & Koch, M. H. J. (1999). Observation of Size-Dependent Melting in Lipid Nanoparticles. *The Journal of Physical Chemistry B, 103*(47), 10373-10377. doi:10.1021/jp9912612

Valeri, D., & Meirelles, A. J. A. (1997). Viscosities of fatty acids, triglycerides, and their binary mixtures. *Journal of the American Oil Chemists' Society, 74*(10), 1221-1226. doi:10.1007/s11746-997-0048-6

Van Langevelde, A., Van Malssen, K., Hollander, F., Peschar, R., & Schenk, H. (1999). Structure of mono- acid even- numbered β- triacylglycerols. *Acta Crystallographica Section B, 55*(1), 114-122. doi:10.1107/S0108768198009392

Vand, V., & Bell, I. P. (1951). A direct determination of the crystal structure of the β form of trilaurin. *Acta Crystallographica, 4*(5), 465-469. doi:10.1107/S0365110X5100146X

Vanhoutte, B., Dewettinck, K., Foubert, I., Vanlerberghe, B., & Huyghebaert, A. (2002). The effect of phospholipids and water on the isothermal crystallisation of milk fat. *European Journal of Lipid Science and Technology, 104*(8), 490-495. doi:10.1002/1438-9312(200208)104

Vanhoutte, B., Foubert, I., Duplacie, F., Huyghebaert, A., & Dewettinck, K. (2002). Effect of phospholipids on isothermal crystallisation and fractionation of milk fat. *European Journal of Lipid Science and Technology, 104*(11), 738-744. doi:10.1002/1438-9312(200211)104

Walstra, P. (2003). *Physical chemistry of foods*. New York: New York : M. Dekker.
Wang, J., & Flanagan, D. R. (1999). General solution for diffusion-controlled dissolution of spherical particles. 1. Theory (Vol. 88, pp. 731-738).

Wang, Y. (2016). Boundaries of the crystal memory effect in saturated triacylglycerols. In E. Department of Process, S. Applied, S. Master of, M. Silvana, A. A. Donaldson, G. Thomas, M. Gianfranco (Eds.).

West, A. R. (1984). *Solid State Chemistry and its Applications*. England: Chichester.
Widlak, N., Hartel, R. W., & Narine, S. (2001). *Crystallization and solidification properties of lipids*. Champaign, Ill.: Champaign, Ill. : AOCS Press.

Woods, M. E., & Krieger, I. M. (1970). Rheological studies on dispersions of uniform colloidal spheres I. Aqueous dispersions in steady shear flow (Vol. 34, pp. 91-99).

Wright, A., Hartel, R., Narine, S., & Marangoni, A. G. (2000). The effect of minor components on milk fat crystallization. *Journal of the American Oil Chemists' Society, 77*(5), 463-475. doi:10.1007/s11746-000-0075-8

Wright, A. J., & Marangoni, A. G. (2002). Effect of DAG on milk fat TAG crystallization. *Journal of the American Oil Chemists' Society, 79*(4), 395-402. doi:10.1007/s11746-002-0495-5

Yu, L., Reutzel-Edens, S., & Mitchell, C. A. (2000). Crystallization and Polymorphism of Conformationally Flexible Molecules: Problems, Patterns, and Strategies. *Organic Process Research & Development, 4*(5), 396-402. doi:10.1021/op000028v

Zwietering, M. H., Jongenburger, I., Rombouts, F. M., & Vantriet, K. (1990). Modeling of the Bacterial-Growth Curve. *Applied and Environmental Microbiology, 56*(6), 1875-1881.

APPENDIX A Instrument Calibration

A.1 DSC Calibration

If the data from cyclic empty run is a deviation from the normal trace, a clean procedure must be done. A fiberglass brush must clean the cell. Then a cyclic empty cell run needs to be re-done to check the possible residues of contaminants. If the results still deviate from nominal values, a burn-up step is necessary to further cleaning. This can be done by holding at high temperature (usually 550 °C for 5 min) with dry air.

After the detection of the possible contaminants, a calibration procedure can be done by three steps (Al-Qatami, 2011):

1. Using the "calibration wizard" function with T4 heat flow option with an empty cell.

2. Determining the R and C values as a function of temperature, for the reference and sample sensors (with heating rate of 20 C°/min in first two runs)

3. Determining the cell constant and the temperature calibration: Indium was used as a standard due to the known enthalpy and melting temperature. The cell constant is a correction factor for the heat flow, which equals to the ratio of $H_{Theoretical}$ / $H_{Measurement}$.

A.2 Rheometer calibration

Geometry Inertia

The geometry is a moving component in the measuring system, which is attached to the driving motor spindle. The geometry file was chosen from previous geometry folder (Geometry>Open). The inertia of each measuring geometry differs due to unique engineered design and different masses. To calibrate the geometry inertia, we can choose Geometry Page >Settings>Inertia: Calibrate from the menu in the software. The calibration of geometry inertia is very important in measuring low viscosity fluids, especially under high-frequency oscillations.

Bearing Friction Correction

In AR 2000, an air bearing is used to set the drive shaft afloat and provide virtually friction-

free application of torque to the sample. However, there will be some residual friction, which can lead to inaccuracies in the final rheological data. To calibrate bearing Friction, an air bearing friction correction should be activated (Options>Instrument>Miscellaneous, check the 'bearing friction correction').

Rotational Mapping

The air bearing will have small variations in torque behavior around one complete revolution of the shaft. These variations are consistent over time unless changes occur in the air bearing. Thus, when in a test, a real-time correction can be made via the mapping of such rotational torque which stores variations. To create a map(Instrument>Rotational Mapping), the software rotates the drive shaft at a fixed speed, monitoring the torque required to maintain this speed through a full 360° of rotation (without operator intervention - a confidence check in bearing performance).

Zero the gap

The distance between the geometry and cup was set as 100 micron-meter. To zero the gap, the geometry moves down until touches the base of the cup in the absence of a sample, where a zero point can be obtained. It's necessary to zero the gap at the testing temperature because of thermal expansion and contraction of the geometry's material. This calibration can be accomplished automatically by pressing zero gap icon in the software.

System inertia

When the instrument has finished the system check, a series of calibration procedure was done before the experiment. The instrument inertia can be done via selecting Options>Instrument>Inertia. In this research, the system inertia value was 15.7 μNms^2 (An acceptable range is 14-16 μNms^2).

A.3 Polarized light microscopy alignment

To align the PLM, the light path selector knob needs to be switched to observation tube. Place a sample slide on the microscope stage, and the PLM need to be brought into focus with the 10× objective. Close the iris diaphragm completely with the field iris diaphragm ring. When a blurred polygon can be observed directly, the condenser height needs to be

adjusted to focus the image of the field diaphragm. Open the field iris diaphragm to increase the diameter of the field progressively until the digraph is centered and covers all the field of view. It is suggested to adjust the aperture iris diaphragm to 70% or 90% of the numerical aperture of the objective. The polarized light can be adjusted by the polarizer ring until the desired extinction is obtained.

A stage micrometer is a microscope slide that is engraved a fine and accurate scale (Figure 0.1). For 10X objective lens, the physical size of an image is aprroximately 1.2 x 0.9 mm (calibration scale: 0.7 µm/pixel).

a.   b.
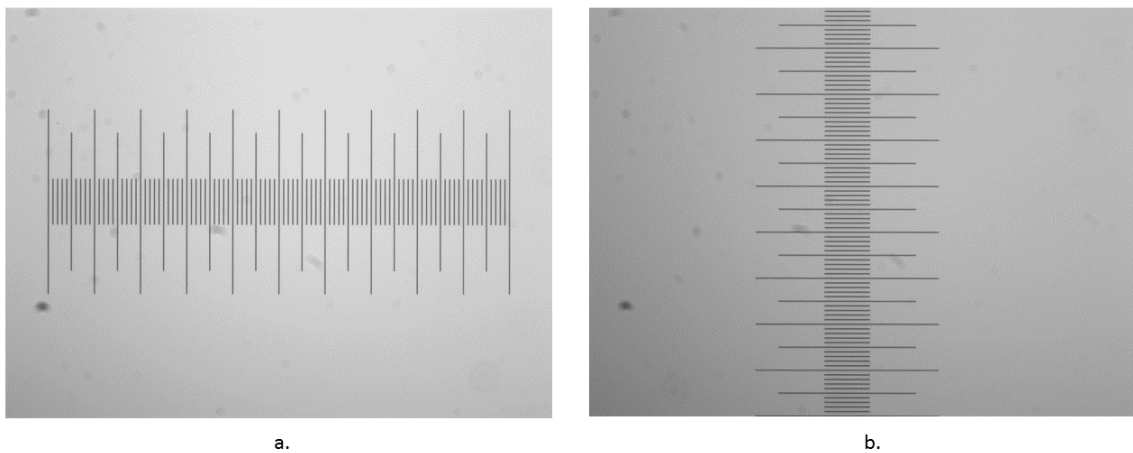
Figure 0.1 (a) Objective micrometer horizontal (10 x) where 100 micrometers are visible (b) Objective Micrometer Vertical (10 X) where 70 Micrometers are covered. (provided by Dr. Gianfranco Mazzanti).

A.4 In-House Wide-Angle X-Ray Diffraction system fittings and alignment
Alignment of the rails

For both small and wide-angle X-ray diffraction experiments, the XRI-UNO/Si 2D X-ray detector needs to be centered and aligned with the X-ray beam. The first step to center the detector is to align the rails of the detector stage (Figure 0.2). In this procedure, the X-ray beam was captured by the detector at the approximate center position with a short X-ray exposure time (10 s), to avoid-radiation damage of the detector.
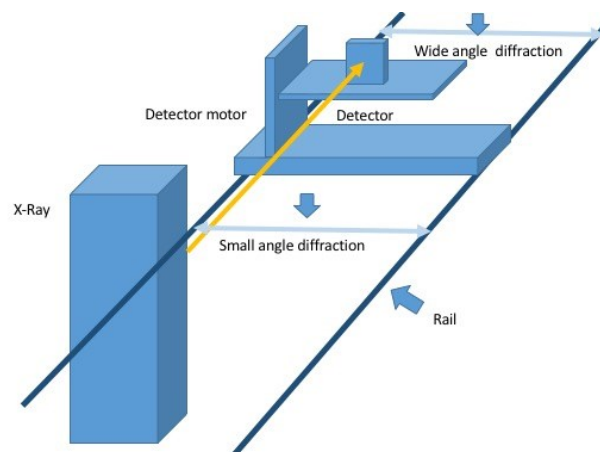
Figure 0.2 Schematic representation of the detector and its rail system.

This alignment of rails can be done in three steps:

a. ***Finding the centering position of the XRI-UNO detector at wide angle position:***

Images obtained via a short X-ray exposure were then opened in ImageJ to estimate the position of the X-ray beam stop at the detector. The XRI-UNO detector can produce a 256×256-pixel image. Thus, X-ray beam should be at the central part of image (128, 128). Several approximate positions for XRI-UNO detector were tested to match the theoretical beam center position (Figure 0.3 (a)). After finding the beam center, the detector position was reset as (0,0) in the SPEC program. Moreover, a mark (start point, corresponding to the beam stop at the detector) was made on the table, keeping the same horizontal position (shown in Figure 0.3 (b)). The final results of beam stop position (calculated via ImageJ) on the detector are shown in Figure 0.4.
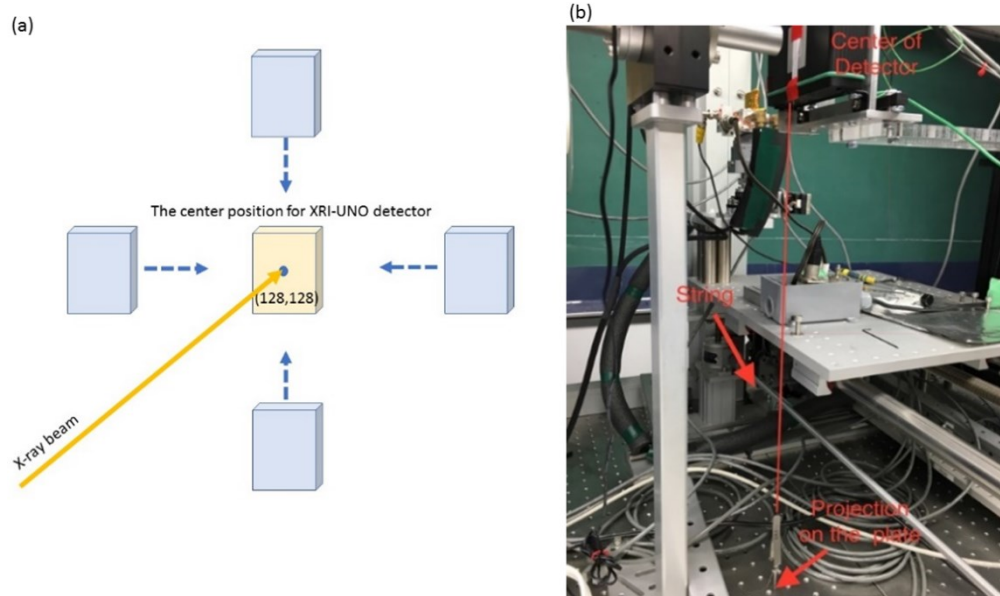
Figure 0.3 (a) Schematic representation of finding the center position for XRI-UNO detector. (b) Schematic representation of marking of the center position on the table.
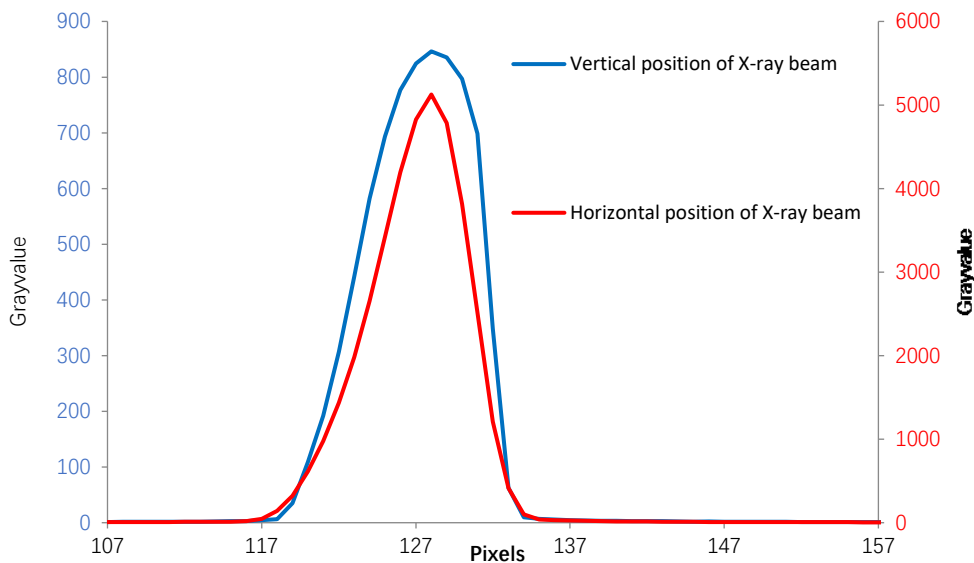

Figure 0.4 The ImageJ analysis results of the center position for XRI-UNO position.

a. *Finding the centering position at small angle position:*

The detector was kept at (0,0) position when moved backward to the small-angle position (at the end of rails). A similar procedure was applied to find the center position of the XRI-UNO detector. After finding the beam center, a mark (end point,

149

corresponding to the beam stop at the detector) was made on the table, keeping the same horizontal position

b. Align the rails with X-ray beam:

After the start and end point were fixed, the X-ray beam pathway then can be projected on the table where the rails locate (as shown in Figure 0.5 (a)). Then the rails were aligned with this drawn X-ray beam fly path. A measuring tape was also fixed on the table, which can help to align the rails (Figure 0.5 (b)).
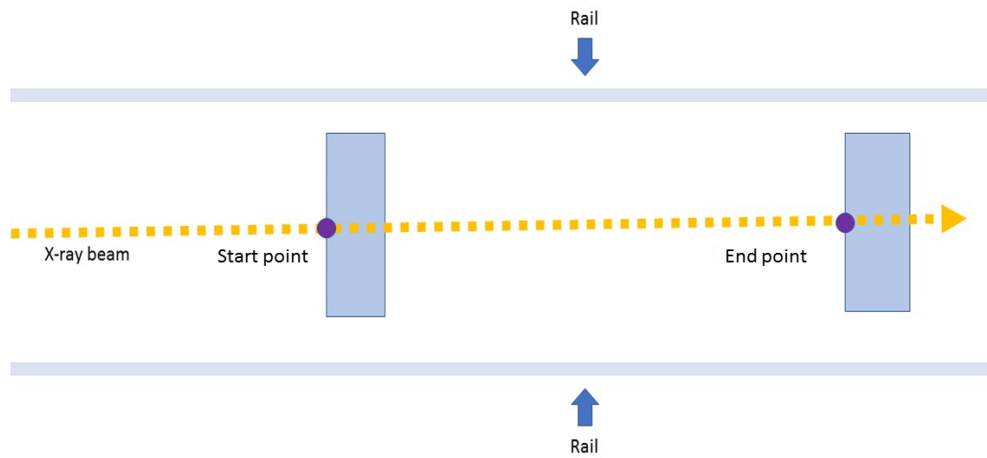
a.
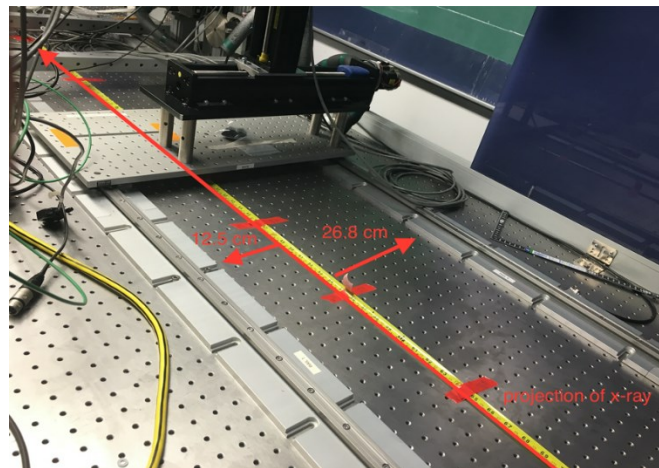
b.

Figure 0.5 (a) Schematic representation of aligning rails with X-ray beam. (b) A measuring tape was fixed on the table to facilitate the alignment.

After alignment, a recheck procedure was done by taking one image (exposure time: 15 s) at the start and end point. The ImageJ analysis results are shown in Figure 0.6. The two overlapping peaks show that XRI-UNO detector obtains the highest intensity of the X-ray beam at WAXD position and SAXD position. Therefore, the rails were well aligned with X-ray beam.
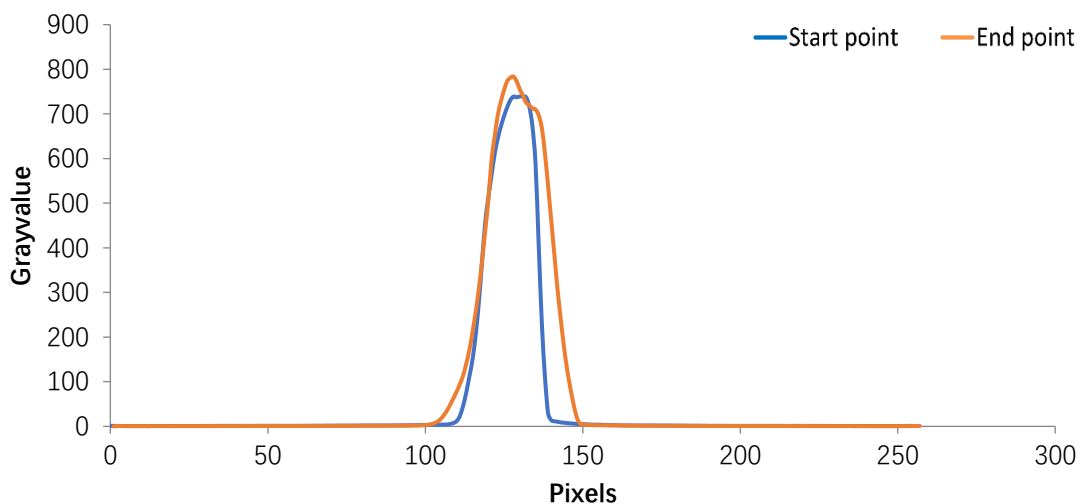

Figure 0.6 The comparison of gray values between the start point (for wide angle diffraction) and end point (for small angle diffraction).

Detector Distance Calibration

Al$_2$O$_3$ was used to calibrate the distance from the capillary cell to the XRI-UNO detector. For Al$_2$O$_3$, the angular location difference between each diffraction pattern is constant regardless of what the detector distance is. Therefore, this difference can be used to calibrate the detector distance. The typical d-spacing values of Al$_2$O$_3$ are shown in Table 0.1

Al$_2$O$_3$	d (Å)	q (Å^{-1})
d-spacing01	3.480	1.806
d-spacing02	2.551	2.463
d-spacing03	2.379	2.641
d-spacing04	2.085	3.014

Table 0.1 The typical d-spacing values of Al$_2$O$_3$.

As shown in Figure 0.7, d-spacing02 and d-spacing03 were chosen to calibrate the detector distance.
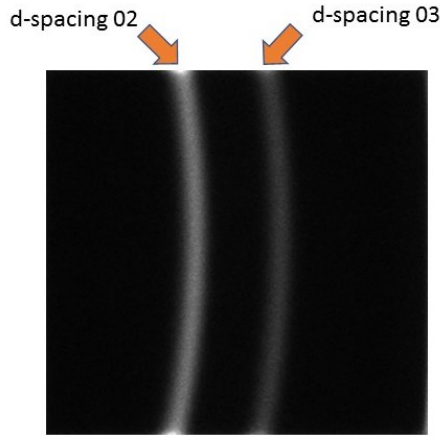

Figure 0.7 A radial plot of Al_2O_3 wide-angle diffraction patterns (d-spacing02 and d-spacing03).

According to Bragg's law and geometry:

$$\lambda = 2d \sin \theta \tag{73}$$

$$\theta = \sin^{-1}\left(\frac{\lambda}{2d}\right) \tag{74}$$

Since λ was constant (0.7093 Å), θ can be calculated by the known d-spacing values from table 0.1. Therefore, as shown in Figure 0.8, the detector distance ($dc_{\_XRD}$) can be determined by:

$$\tan(2\theta) = \tan(2 * \sin^{-1}(\frac{\lambda}{2 * d_{spacing}})) \tag{75}$$

$$dc_{\_diff} = dc_{d\_spacing03} - dc_{d\_spacing02} \tag{76}$$

$$dc_{\_XRD} = \frac{dc_{\_diff}}{\tan(2\theta_{03}) - \tan(2\theta_{02})} \tag{77}$$
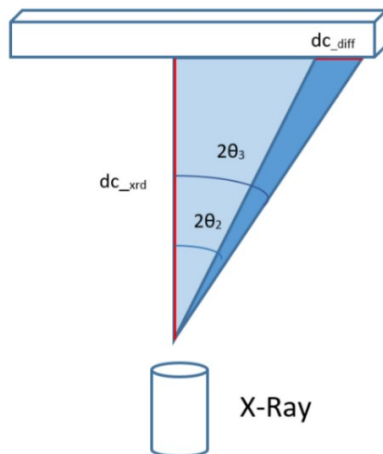
$$CX = \frac{(dc + 7.04)}{p_s} \tag{78}$$

Figure 0.8 A graphic representation of the calibration of detector distance.

According to the radial plot:

	d (Å)	tan(2θ)
d-spacing02	2.551	0.286
d-spacing03	2.379	0.309

Then the $dc_{\_diff}$ and $dc_{\_XRD}$ can be calculated:

$$dc_{\_diff=} = 3.113 \ mm$$

$$dc_{\_XRD} = 140.78 \ m$$

In this experiment, the distance from the capillary cell to the XRI_UNO detector is 140.78 mm. Other parameters for X2RD program are shown in Table 0.2.

Parameter	Value	Unite
λ	0.7093	Å
ps	0.055	mm/pixel
dc_XRD	140.78	mm
CX	633.25	pixel
CY	128	pixel

Table 0.2 Parameters for X2RD program.

APPENDIX B Methodology for Data Analysis of the XRD Measurement

B.1 Normalizing images

Images (8-bit raw) taken under the same temperature were opened as a stack (a series of images that shares a single window) with size 256 X 256 pixels in ImageJ software. A single image was then made from this stack via Z project function. At last, this single image was saved in a 16-bit format (Figure 0.9), which allows to create a radial plot via ImageJ plug-in program.
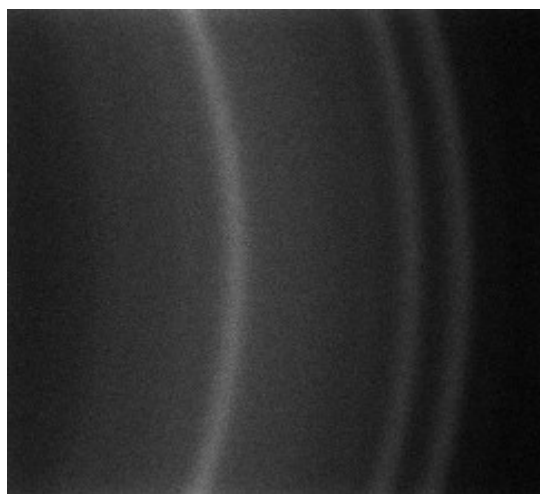

Figure 0.9 An example of 16-bit image created for radial plot.

B.2 Creating radial plots

Stefan Idziak, Gianfranco Mazzanti, Maochen Hannah Wang, and Kisun Park developed an XR2D plug-in program for ImageJ (Figure 0.10). This plug-in program allows user to create a radial plot for further analysis. In XR2D program, XRD 2D image can be reduced to 1D plot of intensity as a function of scattering vector q. This 1D plot is made by taking a radial average of intensity at increasing value of q or pixel values. Thus, a radial plot can keep the XRD information such as peak position, X-ray scattering intensity and full width at half maximum (FWHM).

To create a radial plot, images were first opened as a stack of 16 bits unsigned image (256 X 256 pixels). Then several parameters need to be input into the program to extract radial plot from the stack image (Figure 0.9). These parameters were determined as mentioned above (*i.e.,* λ = 0.7093 Å, distance = 140.78 mm, CentreX = -290.18 and CentreY = 128

pixels).

On the other hand, the silicon chip produces noise that interferes with the data analysis. To exclude this noise, the ROI (region of interest) boundaries were carefully selected and applied to all image stacks (*i.e.,* x Left = 6.0, x Right = 249. 0, y Up = 6.0 and y Down = 249.0). A starting radius (q = 1.1 Å^{-1}) and ending radius (q = 1.85 Å^{-1}) were set within this specified boundary. A radial plot was then established within this region including all necessary information. This radial plot was then exported in "text image format" (standard tab-delimited ASCII text file) for Igor analysis.
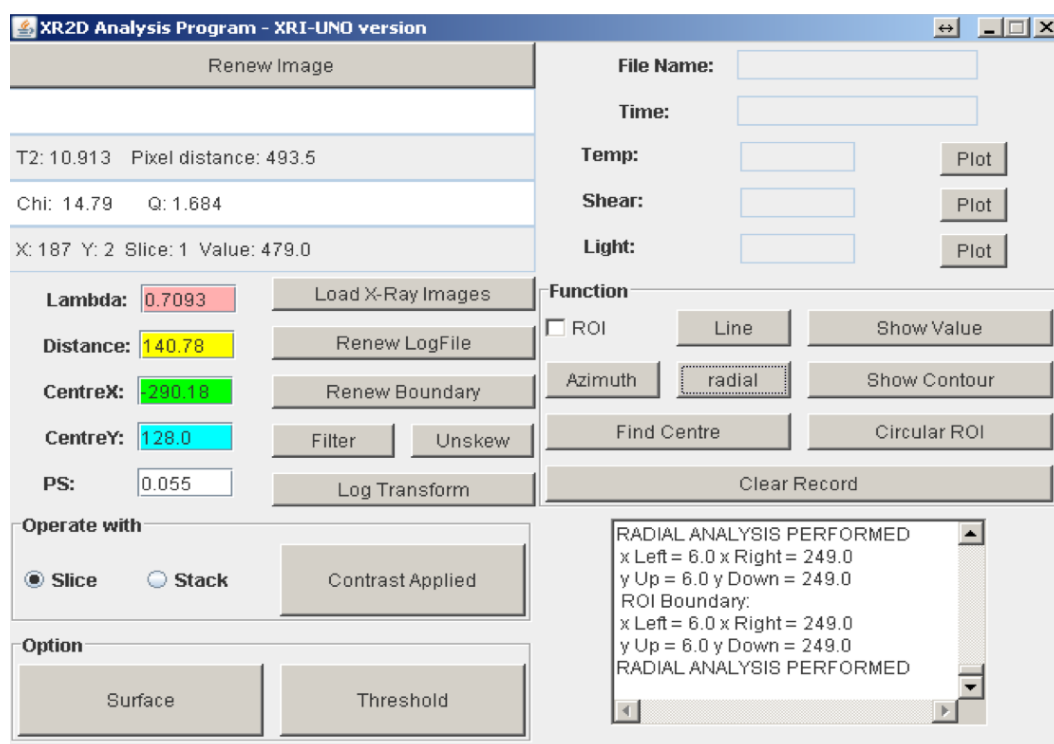

Figure 0.10 An example of GUI of XR2D plug-in program for ImageJ.

B.3 Peak Fitting by Igor Pro

Igor Pro 6.0 (Wavemetrics Inc.) is a scientific data analysis software for curve fitting and peak fitting. All the peak fittings were performed in Igor pro as follows:

a. **Baseline calibration:** In Igor Pro 6.0, baseline can be set up as, constant, linear, Cubic, logCubic and logPoly5. In this research, linear or cubic background functions were chosen to fit data.

b. **Peak fitting:** A package, Multi-peak Fit 2, from Igor Pro, was used to fit peaks.

155

This package fits peaks by minimizing the error with a fixed baseline and defined peak types (default as Gauss type and maybe changed to another kind if necessary). The "auto locate peaks" function was used to locate any positive positioned peak in one curve file automatically. Optimization can be accomplished by adjusting these two parameters (baseline or peak type) to find the best fit. As shown in Figure 0.11, results (*e.g.*, peak location, amplitude, area, and FWHM) were reported automatically after peak fitting.
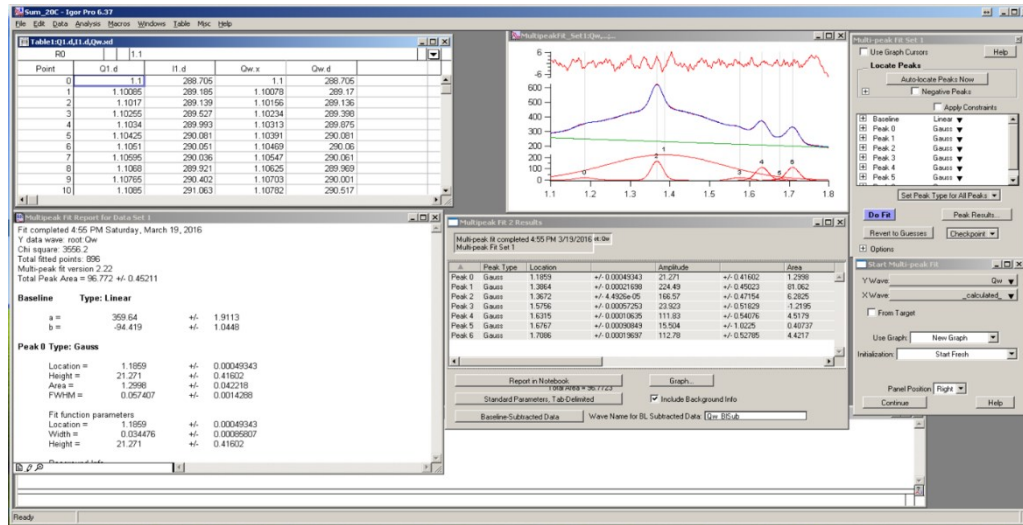

Figure 0.11 User interface for Igor Pro Multi-peak fit function.

Types of function

In this experiment, Gauss, Lorentzian, and Voigt function were applied in fitting the WAXD peaks.

a. **The Gauss distribution:** a characteristic bell shape is defined by two parameters, the frequency from line center (x) and variance (σ^2) (Deng, 2014):

$$G(x;\ \sigma)\ =\ \frac{1}{\sigma\sqrt{2\pi}}\exp\left[-\frac{1}{2}\left(\frac{q-q_0}{\sigma}\right)^2\right] \tag{79}$$

- Where: q is the reciprocal lattice spacing; σ is the standard deviation of the distribution function.

b. **The Lorentzian distribution:** a continuous symmetric probability distribution with a width characterized by its full width at half maximum (γ) (Deng, 2014):

$$L(q - q0; \gamma) = \frac{\gamma}{\pi((q - qo)^2 + \gamma^2)} \tag{80}$$

- Where: γ is the full width at half maximum; q is the reciprocal lattice spacing; q0 is the reference reciprocal lattice spacing.

c. **Voigt distribution**: a convolution of a Lorentzian and a Gauss profile (Deng, 2014):

$$V(x; \sigma, \gamma) = \int_{-\infty}^{\infty} G(x'; \sigma) L(x - x'; \gamma) dx \tag{81}$$

- Where: σ is the standard deviation of the distribution function; γ is the full width at half maximum.

Uncertainty of the experimental data

There are four kinds of uncertainty associated with peak fitting in Igor 6.0. The first kind of uncertainty of experimental data is the sigma of the location obtained from the peak fitting by Igor Pro. This sigma of the location reflects the error range and distribution (randomly or orderly) of the peak locations because of uncertainties of the fit. The second uncertainty was observed with a different sample from the same material. The third kind of uncertainty is associated with various samples and different peaks. The third kind of uncertainty should be largest in the group (Deng, 2014).

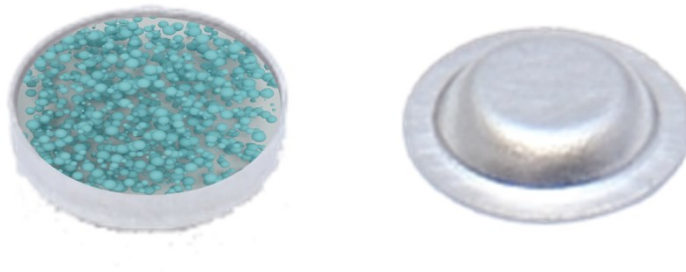**APPENDIX C** Simulation of molecular movement in a DSC pan.

Figure 0.12 Hermetic aluminum sample pan/lid set. Modified from TA
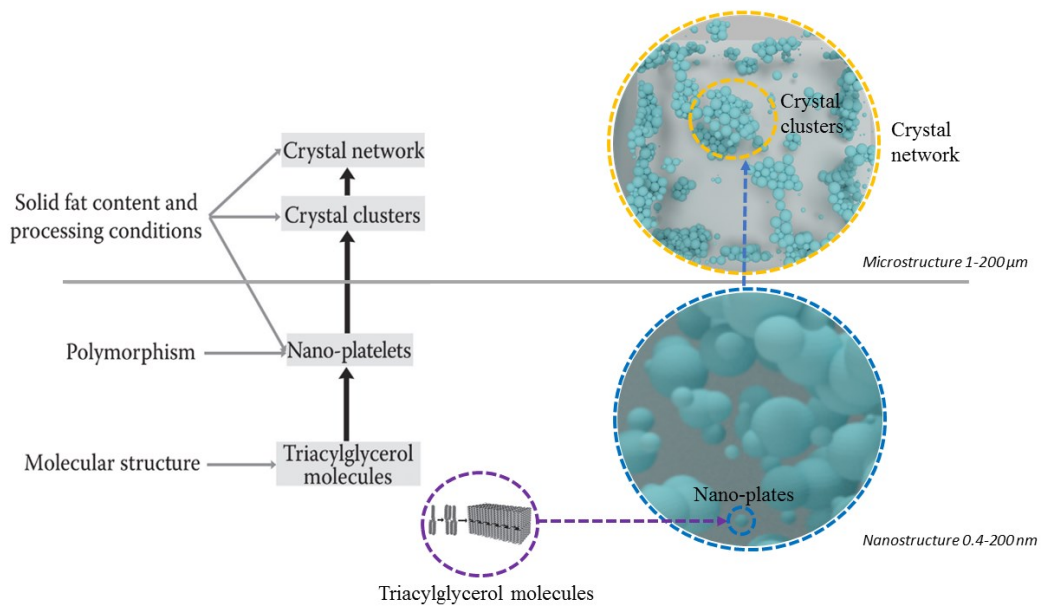(http://www.dscconsumables.com/product/DSC84006.html)

Figure 0.13 Structural hierarchy in a fat crystal network from molecules to material. Modified from (Marangoni & Wesdorp, 2013).
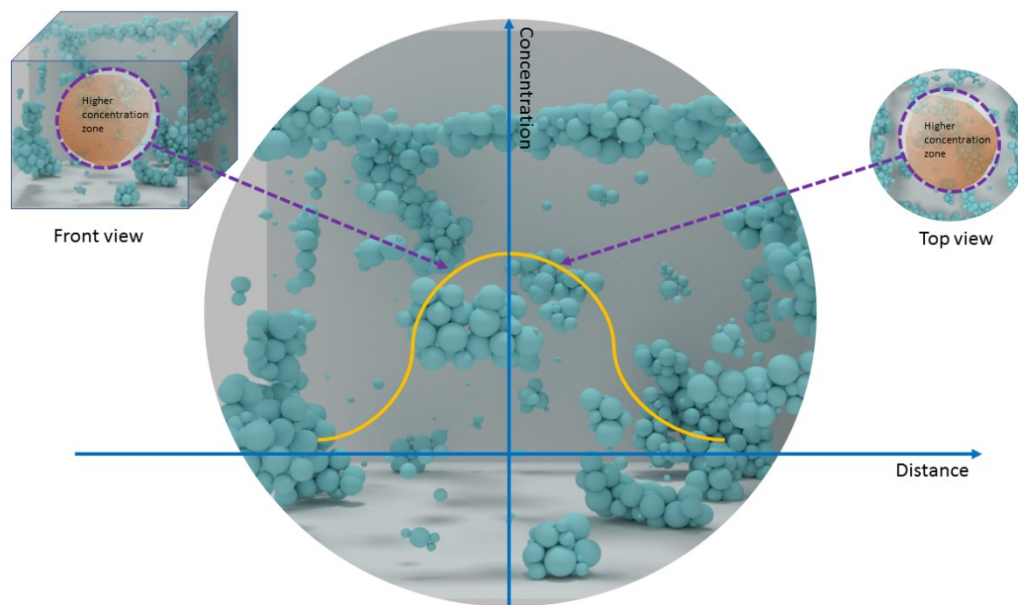
Figure 0.3 An illustration of simulation of SSS crystals distribution in the DSC pan at the end of experiment.